International Scientific-Technical and Production Journal

The Paton WELDING JOURNAL

June 2004 # 6

English translation of the monthly «Avtomaticheskaya Svarka» (Automatic Welding) journal published in Russian since 1948

Founders: *E.O. Paton Electric Welding Institute of the NAS of Ukraine*
International Association «Welding»

Publisher: *International Association «Welding»*

Address:
E.O. Paton Electric Welding Institute,
International Association «Welding»,
11, Bozhenko str., 03680, Kyiv, Ukraine
Tel.: (38044) 227 67 57
Fax: (38044) 268 04 86
E-mail: journal@paton.kiev.ua
http://www.nas.gov.ua/pwj

State Registration Certificate
KV 4790 of 09.01.2001

Subscriptions:
$460, 12 issues per year,
postage and packaging included.
Back issues available.

CONTENTS

EFFECT OF A SHIELDING GAS ON CONTRACTION OF THE TUNGSTEN-CATHODE WELDING ARC

P.V. PORITSKY[1], V.P. PRILUTSKY[2] and V.N. ZAMKOV[2]
[1]Research Centre «Institute for Nuclear Research», NASU, Kiev, Ukraine
[2]E.O. Paton Electric Welding Institute, NASU, Kiev, Ukraine

Considered is the effect of characteristics of a gas atmosphere on the process of contraction of the welding arc in inert gases. Calculations have been made, showing that the degree of contraction of the arc discharge depends upon the thermal-physical characteristics of the gas atmosphere and electron-atom collision processes. Impact of the Ramsauer effect on the arc discharge contraction characteristics has been established.

Keywords: *contraction, inert gas, welding arc, Ramsauer effect*

The welding arc is an electric discharge occurring in an electrically conductive gas channel (plasma column). Conductivity of the arc plasma is a result of thermal ionisation of gas at relatively high temperatures, compared with temperature of electrodes. This is the case of balance between the heat released in the plasma under the effect of the electric current flow and heat removed to the electrodes and ambient atmosphere. Space characteristics of the positive arc column and distribution of the current density in it determine parameters needed for realisation of thermal equilibrium. In turn, analysis of distribution of the current density in the positive arc column makes it possible to establish relationship between the discharge parameters for different welding conditions.

Increase in the current density (energy concentration) in the welding arc, other conditions being equal, leads to increase in the metal penetration depth during welding. This makes study of the mechanism of contraction of the welding arc especially topical, which is associated with an increased attention of specialists to widening of technological capabilities of TIG welding through changing composition of a shielding gas and adding fluxes to the arc zone.

Contraction of the discharge takes place providing that the following conditions are met [1–6]: volume neutralisation of the charged particles dominates over their diffusion drift to the «discharge chamber walls»[1], and frequency of formation of the charged particles dramatically decreases in a direction from the discharge axis to the arc periphery. The degree of contraction of the discharge is determined by non-uniformity of the distribution of temperature across its section. Thermal contraction is caused by decrease in temperature on the periphery of the discharge and increase in the gas density (under a constant pressure). Therefore, electrons on the periphery of the discharge give up the major part of their energy to the neutral particles. Their temperature falls. In turn, this enhances the recombination processes and, hence, decreases the concentration of electrons. The energy transferred from electrons to heavy particles depends upon their type (atoms, ions, molecules, etc.). Therefore, the degree of contraction of the arc caused by heat contraction depends upon the type of a shielding gas.

As a rule, when evaluating parameters of the arc discharge plasma, the frequency or section of electron-atom collisions is assumed to be independent of the electron energy. This makes it possible to substantially simplify the required calculations [3–6]. However, this assumption is not always justifiable, as the section of electron-atom collisions may have a non-monotonous dependence upon the electron energy. In particular, a deep minimum is seen for some inert gases and alkali metals (Ramsauer effect), and this has a decisive effect on the discharge plasma parameters.

The purpose of this study was to investigate the effect of physical characteristics of shielding gases on contraction of the positive arc column. For this, a detailed analysis of the processes causing heat contraction was conducted, subject to a difference between the electron and gas temperatures in the arc column plasma.

Local thermodynamic and ionisation equilibrium. It is conventional to describe the state of the normal- or high-pressure arc discharge plasma, which is also the case of the welding arc, as a local thermodynamic and ionisation equilibrium [3–7]. Because of high concentrations of atoms and electrons, the collision processes in this plasma play a much more important role than the transfer processes. Therefore, the transfer of particles under the effect of space non-uniformity is insignificant, and the state close to equilibrium persists at each point of the discharge. This state is characterised by certain gas, T, and electron, T_e, temperatures, while the velocity distributions of atoms and electrons correspond here to the Maxwellian function.

The above temperatures set as a result of an interaction of electrons with external fields, collision of

[1]In the case of a free-burning welding arc, the term «discharge chamber wall» means a zone on the discharge periphery, where the temperature is close to that of the ambient atmosphere.

electrons and atoms, and transfer of heat across the discharge section. At the same time, the relationship between T and T_e is determined only by the collision processes and interaction of electrons with the external electric field. In the case of DC welding, where the gas discharge plasma is in a constant electric field with intensity E, the equation describing the T and T_e relationship has the following form [1, 8]:

$$T_e - T = \frac{m_a}{3k}\left(\frac{eE}{m_e}\right)^2 \frac{\langle u^2/\nu_{ea}\rangle}{\langle u^2\nu_{ea}\rangle}, \quad (1)$$

where m_a is the mass of an atom; k is the Boltzmann constant; e is the charge of an electron; m_e is the mass of an electron; u is the velocity of an electron; angle brackets mean an averaged velocity distribution of electrons using the Maxwellian function; and ν_{ea} is the frequency of electron-atom collisions.

In particular, if ν_{ea} does not depend upon the electron velocity, formula (1) will have the following form:

$$T_e - T = \frac{m_a w_e^2}{3k}, \quad (2)$$

where w_e is the drift velocity of electrons equal to

$$w_e = \frac{eE}{m_e}\langle u^2/\nu_{ea}\rangle. \quad (3)$$

The gas-discharge plasma is in the state of a local thermodynamic equilibrium, providing that the characteristic time of energy exchange between electrons (due to collisions) is short, compared with the characteristic time of energy exchange in their collisions with atoms and characteristic time of energy transfer of electrons to other regions of the discharge.

Consider gas at low ionisation, where

$$kT_e << E_I, \quad (4)$$

where E_I is the effective energy of ionisation of the gas atmosphere.

For the welding arc, where the local thermodynamic equilibrium, including the ionisation equilibrium, persists, the density of electrons, n_e, at a given point of the discharge is related to the density of positive electrons, n_i, and neutral atoms, n_a, by the Saha equation [7, 9, 10]:

$$\frac{n_e n_i}{n_a} = \frac{2g_i}{g_a}\left(\frac{2\pi m_e kT_e}{h^2}\right)^{3/2}\exp\left(\frac{E_I}{kT_e}\right), \quad (5)$$

where h is the Planck constant; g_i and g_a are the statistical weights for the basic states of ion and atom, respectively.

Owing to condition $kT_e << E_I$, the density of excited atoms is low, compared with that of atoms in the basic state. Criterion of the local ionisation equilibrium has the following form [3, 11]:

$$\tau_{rec} << \tau_{dif}, \quad (6)$$

where $\tau_{rec} \sim (K_{rec}n_e^2)^{-1}$ is the characteristic time of recombination of an individual electron; $\tau_{dif} = r_{PS}^2/a_g D_{amb}$ is the characteristic time of diffusion of the electron from the region occupied by plasma; K_{rec} is the velocity constant of a three-part recombination of electrons and ions determined by formula $K_{rec} = 6.4\cdot10^{-22}(1000/T_e)^{9/2}$ cm^6/s [3–5]; r_{PS} is the radius of the region occupied by plasma; a_g is the parameter that depends upon the discharge geometry ($a_g = 5.78$ for a cylindrical geometry); and D_{amb} is the coefficient of ambipolar diffusion expressed in terms of the coefficient of diffusion of ions, D_{ion}:

$$D_{amb} = D_{ion}\left(1 + \frac{T_e}{T}\right). \quad (7)$$

The coefficient of diffusion of ions is determined primarily by the process of resonance re-charging and calculated from the following formula [5, 10]:

$$D_{ion}N = d_{i0}\sqrt{T/T_{i0}}, \quad (8)$$

where N is the quantity of heavy particles (atoms and ions) in unit volume; and d_{i0} and T_{i0} are some constants for a given gas.

Therefore, the local ionisation equilibrium takes place providing that

$$\eta = \frac{\tau_{dif}}{\tau_{rec}} = \frac{K_{rec}n_e^2 r_{PS}^2}{a_g D_{amb}} >> 1. \quad (9)$$

It should be noted that this criterion is stronger than the criterion of the possibility of describing the gas-discharge plasma by a two-temperature model, having the following form [8, 10]:

$$n_e\sigma_{ee} >> \frac{m_e}{m_a}n_a\sigma_{ea}, \quad (10)$$

where σ_{ee} and σ_{ea} are the characteristic sections of electron-electron and electron-atom collisions.

Criterion (10) for the argon plasma has the form of $n_e/n_a >> 2\cdot10^{-7}$ at $T_e = 10^3$ K and $n_e/n_a >> 5\cdot10^{-6}$ [8] at $T_e = 10^4$ K.

Contraction of the positive arc column. Consider plasma of the positive welding arc column, given that it has a cylindrical shape, local thermodynamic and ionisation equilibrium, as well as a constant pressure across the discharge section. Assuming that the intensity of heat release is proportional to the local current density, write down the heat transfer equation (Elenbaas–Heller equation [3–6]) in the following form:

$$\frac{1}{r}\frac{d}{dr}\left\{r\left[\kappa(T)\frac{dT}{dr} + \kappa_e(T)\frac{dT_e}{dr}\right]\right\} + q(r) = 0, \quad (11)$$

where r is the distance from the discharge axis; $\kappa(T)$ and $\kappa_e(T_e)$ are the coefficients of gas and electron thermal conductivity; $q(r) = j(r)E$ is the intensity of heat release in unit volume; $j(r) = \sigma E$ is the electric current density; and σ is the electrical conductivity of plasma.

Equation (11) describes heat transfer across the section of the discharge allowing for gas and electron thermal conductivity. Solution of this equation also determines the temperature field in the arc plasma. Boundary conditions are selected as follows: arc temperature is $T(0) = T_0$, and temperature at the discharge chamber wall T_R (with no restriction to the consideration generality) is assumed to be constant (e.g. 300 K).

Because of the presence of local ionisation equilibrium in a region of plasma determining its energy balance, the electron and gas temperatures change but slightly. This allows an approximate analytical solution of equation (11) to be derived by the method described in detail in studies [3–6]. According to this method, dependencies of the current density and energy release, as well as the related values, upon the temperature across the section of the discharge are assumed to be assigned. Coefficients are also assumed to be constant and equal to their values at the discharge axis. These simplifications make it possible to transform equation (11) into a conventional differential equation having an analytical solution. This solution is approximate. At the same time, it allows the effect of different physical processes on the distribution of temperature and other values across the section of the discharge to be analysed.

Adding variable

$$\theta = \frac{[T_e(0) - T_e(r)]E_I}{2kT_e^2(0)}, \qquad (12)$$

yields $n_e(r) = n_e(0)\exp(-\theta)$. Accordingly, the current density and energy release density vary across the section of the discharge as $j(r) = j_0\exp(-\theta)$ and $q(r) = q_0\exp(-\theta)$, where $j_0 = j(0)$ and $q_0 = q(0)$, and as $\kappa_e \sim n_e \sim \exp(-\theta)$.

Adding dimensionless variable

$$x = \left(\frac{r}{R}\right)^2, \qquad (13)$$

where R is the radius of the discharge chamber, yields the following form of thermal balance equation (11):

$$\frac{d}{dx}\left(x\,[\exp(-\theta) + \xi]\,\frac{d\theta}{dx}\right) - A\exp(-\theta) = 0, \qquad (14)$$

where ξ, A and ξ_T are the parameters that determine the distribution of temperature across the section:

$$\xi = \zeta_T\frac{\kappa(T)}{\kappa_e(T_e)}, \quad A = \frac{q_0R^2E_I}{8kT_e^2\kappa_e(T_e)}, \quad \zeta_T = \frac{dT(r)}{dT_e(r)}.$$

In this approximation, as noted above, all values of the coefficients are assigned for the discharge axis, and constancy of the intensity of the electric field and pressure p across the discharge section is used as an additional condition. The augend in equation (14) describes the removal of heat due to gas and electron thermal conductivity, and the addend characterises heat release due to the electric current flowing through the plasma.

Consider in series the modes of the discharge, where the removal of heat is determined in one case by the gas thermal conductivity, and in the other case — by the electron thermal conductivity. In the first extreme case ($\xi >> 1$) the equation has the following solution:

$$\theta = 2\ln[1+(Ax/2\xi)], \qquad (15)$$

which corresponds to the following distribution of the density of electrons across the section:

$$n_e(r) = n_e(0)\exp(-\theta) = n_e(0)F(r), \qquad (16)$$

where $F(r) = \dfrac{1}{(1 + (r/r_g)^2)^2}$ and $r_g = \dfrac{16\zeta_T kT_e^2\kappa(T)}{q_0E_I}$.

Distributions of the current density and energy release intensity are characterised by similar dependencies:

$$j(r) = j_0\exp(-\theta) = j_0F(r), \qquad (17)$$

$$q(r) = q_0\exp(-\theta) = q_0F(r). \qquad (18)$$

Relationship between the power of a unit length of the arc discharge, Q (current I) and its temperature at the discharge centre can be estimated through integrating expression (18) across the discharge section (all values of the quantities in the right part are taken at the discharge centre):

$$Q = IE = \int_0^R q(r)2\pi r dr \approx \frac{16\pi\zeta_T kT_e\kappa(T)}{E_I}. \qquad (19)$$

For the other extreme case ($\xi << 1$), consider two regions θ (depending upon what term of the equation coefficient is ignored). At $\theta > \ln(1/\xi)$, expression (15) is the solution of the said equation.

In a region of $\theta < \ln(1/\xi)$, adding new variable $\psi = \exp(-\theta)$ yields the following form of equation (14):

$$\frac{d}{dx}\left(x\,\frac{d\psi}{dx}\right) + A\psi = 0. \qquad (20)$$

In a general case, solution of the equation is expressed in terms of the Bessel functions. The selected boundary conditions have the form of $\psi(0) = 1$ and $\psi(x_J) = 0$, where $x_J = (r_J/R)^2$ and r_J is the plasma radius ($r_J \le R$). Plasma region $0 \le r \le r_J$ makes the main contribution to the net current of the discharge. Therefore, for region $0 \le r \le r_J$ ($\psi = 0$ at $r > r_J$), it is reasonable to consider only that solution which is expressed in terms of the first-kind Bessel function:

$$\psi = J_0(2\sqrt{Ax}). \qquad (21)$$

Accordingly, the following distribution across the discharge section holds for the electron density:

$$n_e(r) - n_e(0)\exp(-\theta) - n_e(0)J_0\left(2\sqrt{A}\,\frac{r}{R}\right),$$
$$0 \le r \le r_J, \quad n_e(r) = 0, \quad r > r_J. \tag{22}$$

The energy release and current densities are described by similar dependencies:

$$q(r) = q_0 J_0\left(2\sqrt{A}\,\frac{r}{R}\right), \quad 0 \le r \le r_J,$$
$$q(r) = 0, \quad r > r_J; \tag{23}$$

$$j(r) = j_0 J_0\left(2\sqrt{A}\,\frac{r}{R}\right), \quad 0 \le r \le r_J,$$
$$j(r) = 0, \quad r > r_J. \tag{24}$$

The following expression holds for the Q value:

$$Q \approx 1.36 q_0 r_J^2. \tag{25}$$

For the radius of plasma, r_J, which corresponds to vanishing of the Bessel function, we have that

$$r_J^2 \approx \frac{5.78R^2}{4A} \approx \frac{11.57kT_e^2\kappa_e(T_e)}{q_0 E_I}. \tag{26}$$

Therefrom, power of a unit length of the arc discharge is as follows:

$$Q = IE \approx \frac{15.7kT_e^2\kappa_e(T_e)}{E_I}. \tag{27}$$

Combining relationships (16) to (18) and (27) yields a general expression for the intensity of heat release per unit length of the discharge:

$$Q = IE \approx (16\zeta_T\kappa(T) + 5\kappa_e(T_e))\frac{\pi kT_e^2}{E_I}. \tag{28}$$

The effective radius of the plasma is determined from the following relationship:

$$\int_0^R n_e(r)2\pi r dr = 1.36 n_e(0) r_0^2, \tag{29}$$

yielding $r_0^2 = 2.31 r_g^2$ and $r_0 = r_J$, respectively, for the above particular cases. Thus, the general expression for the effective radius of the plasma is a combination of expressions for radii from (16) to (18) and (26):

$$r_0^2 = (37.1\zeta_T\kappa(T) + 11.6\kappa_e(T_e))\frac{kT_e^2}{q_0 E_I}. \tag{30}$$

Contraction of the discharge takes place if parameter r_0 characterising sizes of the discharge region is small compared with the discharge chamber radius R. It follows from equation (30) that the region occupied by the discharge decreases with increase in the energy release. At the same time, characteristic contraction radius r_0 depends also upon the value of T_e. Hence, it follows that the range of the plasma increases with increase in difference between the electron temperature and the gas one. As the lower limit for the electron temperature is the gas one, the most intensive contraction takes place when these temperatures are equal to each other.

Difference of the electron temperature. To study the character of difference of the electron temperature in different inert gases, it is convenient to write down expression (1) in the following form [8]:

$$T_e - T = \left(\frac{E}{n_a}\right)^2 g(T_e), \tag{31}$$

where

$$g(T_e) - \frac{m_a}{3k}\left(\frac{e}{m_e}\right)^2 \frac{\langle u^2/k_{ea}\rangle}{\langle u^2 k_{ea}\rangle}. \tag{32}$$

Here $k_{ea} = \nu/n_a = u\sigma_{ea}^*(u)$ is the constant of the velocity of electron-atom collisions, and σ_{ea}^* is the transport (diffusion) section of the electron-atom collisions.

Function $g(T_e)$ does not depend upon the intensity of the electric field, E, and atom density n_a. Therefore, it is a universal characteristic of difference between the electron temperature and the gas one[2]. This difference between the electron and gas temperatures can be expressed in terms of the product of square of the E/n_a ratio (reduced intensity of the electric field) by $g(T_e)$.

The form of function $g(T_e)$ for different gases is shown in Figure 1. Because of the Ramsauer effect, $g(T_e)$ has a maximum for argon, krypton and xenon. As a result, instabilities may take place in plasma at low values of E/n_a and gas temperatures. In particular, for xenon the value of the critical reduced intensity of the electric field, below which the instabilities may develop in plasma, is 0.03 Td [5, 6]. As the range of the instabilities in plasma corresponds to low electron temperatures (< 3500 K), this fact is insignificant for actual conditions of the welding arc. Electron thermal conductivity in plasma depends upon the temperature of electrons. In an assumption of constancy of the diffusion section of scattering of electrons at atoms, the electron thermal conductivity coefficient can be determined using the following formula [3–6]:

$$\kappa_e = \kappa_{e0}\left(\frac{n_e}{n_a}\right)\left(\frac{T_e}{T_{e0}}\right)^{1/2}, \tag{33}$$

where T_{e0} and k_{e0} are the certain constants.

It might be expected that, as the electron temperature increases (according to formula (30)), size of the discharge domain will increase more intensively than in the case of a linear dependence upon T_e.

As the characteristic radius of contraction, according to formula (30), depends also upon the gas thermal conductivity, their relationship should be taken into account.

[2]The E/n_a ratio is usually expressed in townsends (Td). 1 Td = $= 10^{-17}$ V·cm^2.

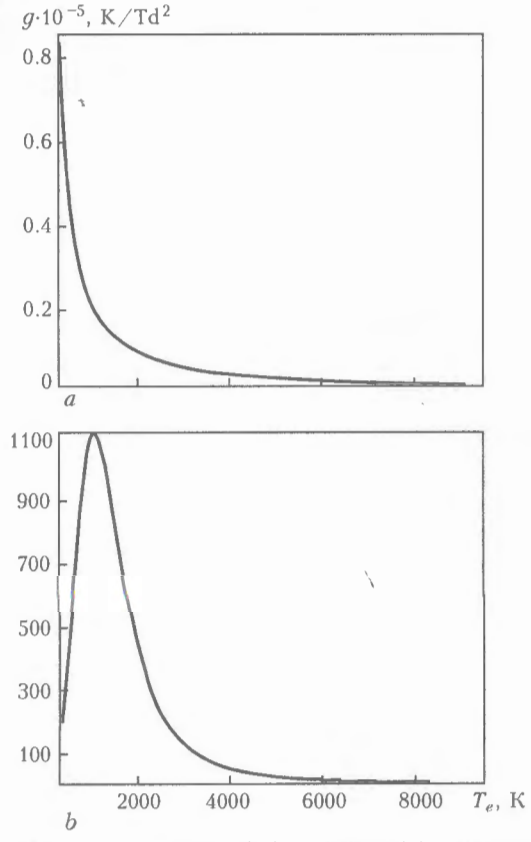

Figure 1. Forms of function $g(T_e)$ for helium (*a*) and argon (*b*)

Arc discharge model. Factors that cause contraction of the arc discharge are substantially different in an extent of the effect they exert. To compare, consider the welding arcs in different inert gases at the same values of current I. Equation (11) can be simplified by adding a heat function:

$$S = \int_0^{T_e} \kappa_e(T_e')dT_e' + \int_0^{T} \kappa(T')dT'. \qquad (34)$$

If we assume that $\kappa(T) \sim T\gamma$, and that the values of the gas and electron temperatures are equal to their values at the discharge axis, providing that condition (4) is met, this yields

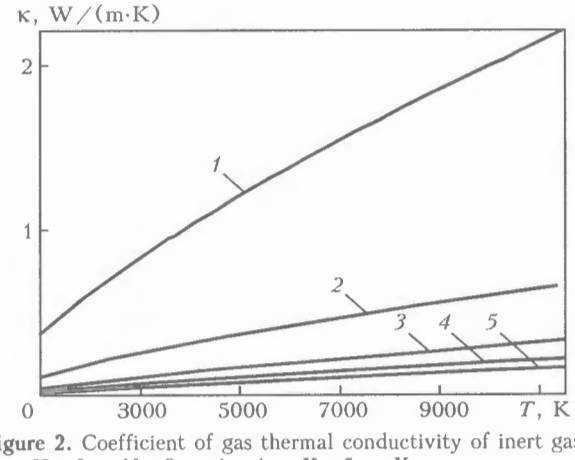

Figure 2. Coefficient of gas thermal conductivity of inert gases: *1* — He; *2* — Ne; *3* — Ar; *4* — Kr; *5* — Xe

Table 1. Parameters of thermal conductivity formula [12] for inert gases

Gas	$\lambda_{273} \cdot 10^3$, *W/(m·K)*	γ
He	143.70	0.73
Ne	46.76	0.71
Ar	16.45	0.80
Kr	8.92	0.86
Xe	5.15	0.93

$$S = \kappa_e(T_e)\frac{2kT_e^2}{E_I} + \kappa(T)\frac{T}{1+\gamma}. \qquad (35)$$

At the same time, double integration of equation (11) yields

$$S = 0.215 q_0 r_0^2 \ln\left(\frac{R}{r_0}\right). \qquad (36)$$

Calculate characteristics of the arc discharge (providing that E and p = const) using expressions (34) to (36) by adding to them the equation of state $p = NkT \approx n_a kT$, Ohm's law and condition of quasi-neutrality of plasma. This results in a system of equations to calculate parameters of the arc discharge:

$$T_e - T = \left(\frac{E}{n_a}\right)^2 g(T_e), \qquad (37)$$

$$IE = \frac{2kT_e^2}{E_I}[16\kappa\zeta_T + 11.57\kappa_e] = q_0\pi r_q^2 = 0.431\pi q_0 r_0^2, \qquad (38)$$

$$S = 0.215 q_0 r_0^2 \ln\left(\frac{R}{r_0}\right) = \frac{2\kappa_e kT_e^2}{E_I} + \frac{T\kappa}{\gamma+1}, \qquad (39)$$

$$p = NkT \approx n_a kT, \qquad (40)$$

$$\frac{n_e^2}{n_a} = \frac{2g_i}{g_a}\left(\frac{2\pi m_e kT_e}{h^2}\right)^{3/2} \exp\left(-\frac{E_I}{kT_e}\right), \qquad (41)$$

$$I = \sigma E \pi r_0^2. \qquad (42)$$

Here

$$r_0^2 = \frac{k_B T_e}{q_0 E_I}[37.1\kappa\zeta_T + 11.57\kappa_e], \quad q_0 = \sigma E^2,$$

$$\zeta_T = \frac{dT}{dT_e} = \left(1 - (T_e - T)\frac{d\ln g(T_e)}{dT_e}\right)\left(\frac{2T_e}{T} - 1\right)^{-1}.$$

The coefficient of gas thermal conductivity of inert gases can be approximately described by the following formula [12]:

$$\lambda = \lambda_{273}\left(T/T_{273}\right)^{\gamma}, \qquad (43)$$

where $T_{273} = 273.16$ K, and $\lambda_{273} = \lambda(T_{273})$.

Table 1 gives values of parameters λ_{273} and γ for different gases. Figure 2 shows values of the coefficients of thermal conductivity of inert gases in a range of 1000–11600 K calculated using formula (43). Helium has the maximum thermal conductivity within

the said temperature range, and xenon has the minimum thermal conductivity. Thermal conductivity of helium is more than by an order of magnitude higher than that of xenon. Thermal conductivity of neon is 4–5 times as high as that of xenon, and 2.5 times as low as that of helium. Thermal conductivity of argon and krypton is higher than that of xenon by a factor of 2 and 1.4, respectively.

Values of electrical conductivity and electron thermal conductivity of plasma were determined from the following formulae [9, 13]:

$$\sigma = \frac{n_e e^2 \langle u^2 \rangle}{m_e \langle u^2 \nu_{ea} \rangle}, \qquad (44)$$

$$\kappa_e = \frac{5}{2} \frac{n_e k^2 T_e \langle u^2 \rangle}{m_e \langle u^2 \nu_{ea} \rangle}. \qquad (45)$$

As the diffusion section of electron-atom collisions for argon, krypton and xenon has a minimum caused by the Ramsauer effect, the transport coefficients of these gases in plasma will have a maximum, which must affect the contraction characteristics. This fact was ignored in studies [3–6], the authors of which used dependence (33). The system of equations (37) to (45) allows determination of the E, T_e, T, n_e, n_a, N and r_0 values at the assigned values of arc current I and pressure p, and vice versa — determination of I and p at the assigned values of E, T_e, T, n_e, n_a, N and r_0.

As the arc gas ionisation degree $\alpha = n_e/N$ is increased to 10^{-4}–10^{-3}, collisions of electrons with ions and effect of the ionisation-recombination processes on heat transfer become more substantial [11]. To allow for these phenomena, it is necessary to take into account the frequency of collisions of electrons with all heavy particles, $\nu_e = \nu_{ea} + \nu_{ei}$, where ν_{ei} is the frequency of electron-ion collisions. Also, it is necessary to take into account the sum of the thermal conductivity coefficients $(k_e + k_p)$, where k_p is the thermal conductivity coefficient depending upon the ionisation-recombination processes.

The frequency of electron-ion collisions is expressed in terms of the diffusion section of Coulomb collisions $\sigma^*_{ei}(u)$ [13]:

$$\nu_{ei}(u) = n_i u \sigma^*_{ei}(u) = \frac{1}{4\pi} n_i \left(\frac{e^2}{m_e \varepsilon_0}\right)^2 \frac{L_{ei}}{u^3}, \qquad (46)$$

where ε_0 is the electric constant; $L_{ei} = \ln\left(\frac{12\pi\varepsilon_0 k T_e r_D}{e^2}\right)$ is the Coulomb logarithm; and $r_D = \sqrt{\frac{\varepsilon_0 k T_e T}{n_e e^2 (T_e + T)}}$ is the Debye radius.

The thermal conductivity coefficient caused by the ionisation-recombination processes for a case of low ionisation has the following form [1, 7]:

$$\kappa_p = \frac{D_{amb} n_e}{2} \left(\frac{E_I}{k T_e}\right)^2. \qquad (47)$$

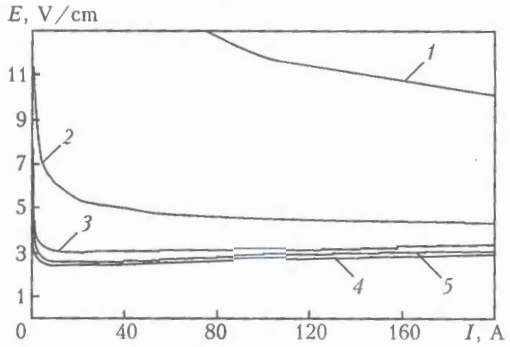

Figure 3. Calculated volt-ampere characteristics (E–I) for arc discharges under atmospheric pressure (R = 0.75 cm): *1* — discharge in He; *2* — Ne; *3* — Ar; *4* — Kr; *5* — Xe

It should be taken into account that thermal conductivity caused by the ionisation-recombination processes may make a marked contribution to total thermal conductivity because of a high value of $(E_I/kT_e)^2$. Values of the sections in calculations were taken from the data of [14], and coefficients of diffusion of ions were taken from [5, 15].

Calculation results and discussion. The above system of equations is a model of the arc discharge, providing that the heat released in the plasma channel is transferred as a result of thermal conductivity to the discharge chamber walls, where a certain temperature is maintained. Such conditions directly correspond to the arc stabilised by the walls. At high currents, they are characterised by a growing volt-ampere characteristic, in contrast to the open arcs having a drooping volt-ampere characteristic [16]. Owing to contraction of the discharge, plasma is concentrated in a limited region near the arc axis. It means that with the wall radius exceeding much the plasma radius, the calculated parameters of the discharge will slightly depend upon the further increase in size of the discharge chamber. Therefore, the case of $R >> r_0$ can be considered corresponding also to the open arc. Naturally, the tungsten-cathode welding arc has no stabilising wall. The role of the wall is played by external factors, such as shielding gas flows caused by external blow, convection [6, 11, 17] and evaporation of the anode surface [11, 18]. Normally, it is recommended that the discharge glow radius be regarded as the wall radius for the open arc [19].

The model considered describes the «long arc», where the heat flow is removed to the walls [11, 17].

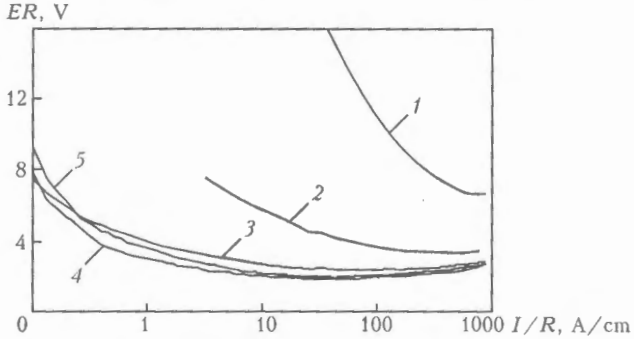

Figure 4. Calculated volt-ampere characteristics (ER – I/R) for arc discharges under atmospheric pressure: *1* — discharge in He; *2* — Ne; *3* — Ar; *4* — Kr; *5* — Xe

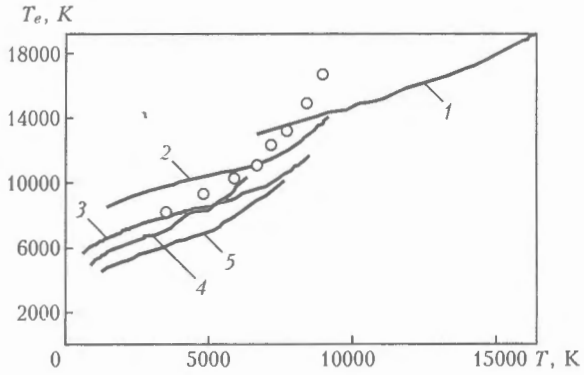

Figure 5. Relationship between gas and electron temperatures in the arc under atmospheric pressure for R = 0.75 cm: *1* — He; *2* — Ne; *3* — Ar; *4* — Kr; *5* — Xe (*circles* — experiments performed in argon [19])

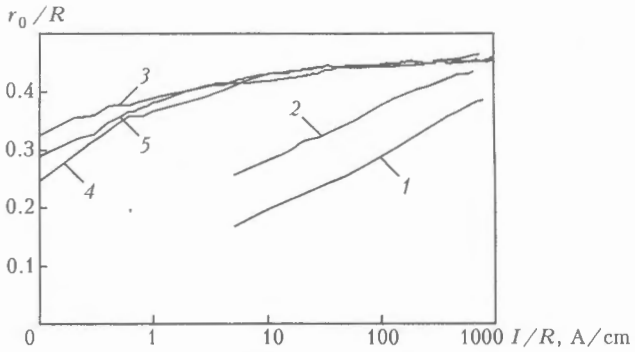

Figure 6. Dependence of relative contraction radius r_0/R upon I/R for the arc under atmospheric pressure: *1* — He; *2* — Ne; *3* — Ar; *4* — Kr; *5* — Xe

Its opposite is the «short arc» (such arcs are usually called also the electrode-stabilised arcs), in which the heat flow is removed mostly to the electrodes. In this case the near-electrode processes dominate. However, according to the data of [20], the welding arc burning at a tungsten cathode in inert gas is impurity-free. Hence, the near-electrode processes in it are thought to have no direct effect on the positive column. Therefore, it seems more appropriate to use the model of the «long arc» to describe the tungsten-cathode welding arc.

Figure 3 shows calculated volt-ampere characteristics (E–I) of the arc discharge, and Figure 4 shows calculated volt-ampere characteristics in terms of variables $ER - I/R$ (the arc with no radiation is described by single curves through variables r/R, ER and I/R [16]). Figure 5 shows calculation of gas and electron temperature in the arc. For argon, krypton and xenon, at R = 0.75 cm, we have a growing E–I characteristic (see Figure 3), whereas for helium and neon the volt-ampere characteristic is drooping. The calculation results are close to the experimentally measured values of the electric field intensity [14] and arc temperature [19]. Thus, under the discharge conditions corresponding to current densities $j_0 < 8.5 \cdot 10^2$ A/cm^2, the difference in the calculation and experimental results [18] is not in excess of 30 % (see Figure 5). The results obtained are in agreement also with the data given in [3–6] for the xenon and argon arcs. In these studies the calculations were made using a more simplified model based on expressions (2) and (33). In a number of cases, it was assumed in them that the sections of electron-atom collisions were independent of the electron energy, which did not allow calculations in a range of temperatures cor-

Table 2. Parameters of arc discharges under atmospheric pressure

No.	Gas	I, A	R, mm	r_0, mm	E, V/cm	T, K	T_e, K	Q, W/cm	q_0, W/cm^3	α	ξ	η
1	Ar	50	1.5	0.69	16.90	5400	10240	$8.5 \cdot 10^2$	$1.3 \cdot 10^5$	$4.8 \cdot 10^{-2}$	$1.5 \cdot 10^{-2}$	$4.4 \cdot 10^3$
2	Same	200	7.5	3.37	3.33	7100	9880	$6.7 \cdot 10^2$	$4.3 \cdot 10^3$	$3.9 \cdot 10^{-2}$	$2.9 \cdot 10^{-2}$	$3.8 \cdot 10^2$
3	»	400	7.5	3.34	3.60	7700	10600	$1.5 \cdot 10^3$	$9.6 \cdot 10^3$	$7.7 \cdot 10^{-2}$	$1.4 \cdot 10^{-2}$	$8.2 \cdot 10^4$
4	»	600	10	4.45	2.76	8150	10700	$1.7 \cdot 10^3$	$6.1 \cdot 10^3$	$8.6 \cdot 10^{-2}$	$1.3 \cdot 10^{-2}$	$1.5 \cdot 10^5$
5	Xe	50	1.5	0.67	16.20	5310	9130	$8.1 \cdot 10^2$	$1.3 \cdot 10^5$	$1.5 \cdot 10^{-1}$	$4.1 \cdot 10^{-3}$	$2.9 \cdot 10^5$
6	Same	200	7.5	3.39	3.07	6600	8800	$6.1 \cdot 10^2$	$3.9 \cdot 10^3$	$1.2 \cdot 10^{-1}$	$1.0 \cdot 10^{-2}$	$3.1 \cdot 10^6$
7	»	400	7.5	3.40	3.34	7150	9400	$1.3 \cdot 10^3$	$8.5 \cdot 10^3$	$2.2 \cdot 10^{-1}$	$3.1 \cdot 10^{-3}$	$5.9 \cdot 10^6$
8	»	600	10	4.50	2.55	7760	9460	$1.5 \cdot 10^3$	$5.6 \cdot 10^3$	$2.4 \cdot 10^{-1}$	$3.3 \cdot 10^{-3}$	$9.5 \cdot 10^6$

Table 2 (cont.)

No.	Gas	I, A	R, mm	r_0, mm	E, V/cm	T, K	T_e, K	Q, W/cm	q_0, W/cm^3	α	ξ	η
9	He	200	7.5	2.53	10.10	13440	16670	$2.0 \cdot 10^3$	$2.3 \cdot 10^4$	$5.3 \cdot 10^{-2}$	0.23	99
10	Same	600	10	3.78	6.73	15630	17800	$4.0 \cdot 10^3$	$2.1 \cdot 10^4$	$1.1 \cdot 10^{-1}$	0.12	$3.9 \cdot 10^2$
11	Ne	200	7.5	3.15	4.35	8060	12370	$8.7 \cdot 10^2$	$6.5 \cdot 10^3$	$2.1 \cdot 10^{-2}$	$4.2 \cdot 10^{-2}$	$1.4 \cdot 10^3$
12	Same	600	10	4.28	3.41	10320	13100	$2.0 \cdot 10^3$	$8.2 \cdot 10^3$	$4.3 \cdot 10^{-2}$	$2.5 \cdot 10^{-2}$	$4.1 \cdot 10^3$
13	Kr	50	1.5	0.68	15.30	4540	9200	$7.6 \cdot 10^2$	$1.2 \cdot 10^5$	$4.5 \cdot 10^{-2}$	$8.0 \cdot 10^{-3}$	$1.7 \cdot 10^4$
14	Same	200	7.5	3.43	2.47	5380	8900	$5.8 \cdot 10^2$	$3.6 \cdot 10^3$	$3.5 \cdot 10^{-2}$	$1.4 \cdot 10^{-2}$	$2.0 \cdot 10^5$
15	»	400	7.5	3.38	3.21	5950	9530	$1.3 \cdot 10^3$	$8.3 \cdot 10^3$	$7.2 \cdot 10^{-2}$	$6.8 \cdot 10^{-3}$	$4.2 \cdot 10^5$
16	»	600	10	4.80	2.32	8500	9400	$1.3 \cdot 10^3$	$4.5 \cdot 10^3$	$7.1 \cdot 10^{-2}$	$1.1 \cdot 10^{-2}$	$3.1 \cdot 10^5$

responding to the Ramsauer minimum in the sections of electron-atom collisions.

The results of calculation of parameters of the arcs at assigned I and p are given in Table 2 and shown in Figure 6. These data allow a conclusion that the higher contraction of the arc discharge in inert gases occurs under conditions where the heat is transferred through gas thermal conductivity, which corresponds to the discharge conditions with relatively low electron temperatures and, therefore, low currents. At an increasing current and constant wall radius R causing increase in electron temperature, the region occupied by plasma also increases. With further increase in the welding current the discharge region hardly changes in size (see Figure 6). If we neglect this slight dependence of the contraction radius upon the reduced current I/R, then $r_0/R \approx$ const and $r_0 \sim R$ with a dominant electron thermal conductivity. According to a conclusion of study [21], the linear dependence of the contraction radius upon the wall radius is a general principle of the thermal contraction. Further increase in electron temperature and ionisation degree of the arc discharge enhances the effect of collisions of electrons with ions, this leading to a slight variation in size of the discharge region for the wall-stabilised arc. This effect was used to develop high-power arc light sources [22]. Note that with a dominant electron thermal conductivity the most contracted arc discharge is that in helium, compared with other inert gases. Also, it should be emphasised that argon, krypton and xenon are among the gases with a distinct Ramsauer effect, which is of a quantum nature and shows up in the presence of a minimum section of electron-atom collisions for electrons with an energy a bit lower than 1 eV. This phenomenon determines «transparency» of a low-ionised gas for such electrons and causes increase in difference between the electron temperature and the gas one, which decreases the arc contraction. Characteristic inflection of the T_e/T curve in Figure 5 corresponds to the region of the Ramsauer minimum.

It should be borne in mind that, because of a difference in values of the sections of electron-atom collisions, the effect of this phenomenon on contraction of the arc discharge in different gases will be greatly different. Thus, other conditions being equal and values of the welding current being low, where the gas thermal conductivity is dominant, the arc discharge in xenon is more contracted than in argon. However, in welding at high currents, where the electron thermal conductivity is dominant, the arc in argon is more contracted than in xenon (see Figure 6). Therefore, for example, xenon should not be regarded as to be an atmosphere in which the arc discharge is always more contracted than in argon.

CONCLUSIONS

1. Contraction of the welding arc burning at the tungsten cathode in an inert gas is determined by its thermal-physical properties and characteristics of electron-atom collisions.

2. Presence of the Ramsauer effect in gas in which the arc is burning leads to a substantial decrease in contraction of the arc discharge within a corresponding temperature range.

3. Contraction of the arc discharge in an inert gas is the highest when welding is performed at relatively low currents with the gas thermal conductivity dominating in the heat removal process. As the current is increased, the region occupied by plasma gradually grows.

4. In welding at high currents the most contracted arc discharge is that in helium.

5. In welding at low currents (other conditions being equal) the degree of contraction of the arc discharge increases in an order of Ar→Xe→Kr.

1. Eletsky, A.V., Palkina, L.A., Smirnov, B.M. (1975) *Phenomena of transfer in low-ionised plasma*. Moscow: Atomizdat.
2. Eletsky, A.V., Rakhimov, A.T. (1977) Instabilities in gas discharge plasma. In: *Chemistry of plasma*. Issue 4.
3. Eletskii, A.V., Smirnov, B.M. (1996) Non-uniform gas discharge plasma. *Physics-Uspekhi*, 39(**11**), 1137–1156.
4. Smirnov, B.M. (1997) Contraction of high-pressure positive arc column. *Teplofizika Vys. Temperatur*, 35(**1**), 14–18.
5. Smirnov, B.M. (2000) Cluster plasma. *Physics-Uspekhi*, 43(**5**), 453–491.
6. Smirnov, B.M., Smirnov, M.B. (1997) Positive column of xenon arc discharge. *Phys. Scripta*, 56(**3**), 302–307.
7. Granovsky, V.L. (1971) *Electric current in gas. Steady-state current*. Moscow: Nauka.
8. Smirnov, B.M. (2002) Kinetics of electrons in gases and condensed systems. *Physics-Uspekhi*, 172(**12**), 1411–1447.
9. Golant, B.E., Zhilinsky, A.P., Sakharov, I.E. (1977) *Principles of plasma physics*. Moscow: Atomizdat.
10. Smirnov, B.M. (1972) *Physics of low-ionised gas*. Moscow: Nauka.
11. Biberman, L.M., Vorobiov, V.S., Yakubov, I.T. (1982) *Kinetics of non-equilibrium low-temperature plasma*. Moscow: Nauka.
12. Fastovsky, V.G., Rovinsky, A.E., Petrovsky, Yu.V. (1972) *Inert gases*. Moscow: Atomizdat.
13. Zhdanov, V.M. (1982) *Transfer phenomena in multicomponent plasma*. Moscow: Energoatomizdat.
14. Haksli, L., Crompton, R. (1977) *Diffusion and electron drift in gases*. Moscow: Mir.
15. Radtsig, A.A. (1981) Diffusion of charged particles in gas in constant electric field. In: *Chemistry of plasma*. Issue 8.
16. Zhukov, M.F., Koroteev, A.S., Uryukov, B.A. (1975) *Applied dynamics of thermal plasma*. Novosibirsk: Nauka.
17. Zhovtyansky, V.A., Patriyuk, V.M. (2000) Peculiarities of heat removal from electric arc in copper vapours. *Ukr. Fizich. Zhurnal*, 45(**9**), 1059–1066.
18. Paton, B.E., Zamkov, V.N., Prilutsky, V.P. et al. (2000) Contraction of the welding arc caused by the flux in tungsten-electrode argon-arc welding, *The Paton Welding J.*, **1**, 5–11.
19. Batenin, V.M., Minaev, P.V. (1969) Temperature at axis of argon-shielded electric arc. *Teplofizika Vys. Temperatur*, 7(**2**), 208–212.
20. Eroshenko, L.E., Prilutsky, V.P., Zamkov, V.N. (1997) Study of glow of anode vapours in arc during TIG welding over the flux layer. *Avtomatich. Svarka*, **11**, 11–13.
21. Rakhimov, A.T., Ulinich, F.R. (1969) Contraction of cylindrical gas discharge. *Doklady AN SSSR*, 187(**1**), 72–74.
22. Vasserman, A.L. (1989) *Xenon tubes and their application*. Moscow: Energoatomizdat.

EVALUATION OF ENERGY TRANSFER TO ARC DISCHARGE ANODE IN INERT GASES

A.V. ERSHOV and O.G. BYKOVSKY
Zaporozhie National Technical University, Zaporozhie, Ukraine

System of equations and boundary conditions are considered for calculation of near-anode zone of temperature- and ionization-nonequilibrium plasma of inert gases at the absence of molecular impurities. The effect of non-equilibrium in argon plasma and distribution of energy fluxes on anode between electrons, atoms and ions is shown.

Keywords: *anode, gradient, diffusion, concentration, ionization, ionization and thermal non-equilibrium, volume charge, voltage drop, Knudsen layer*

Electrical arc discharge in inert gases is used widely in welding processes, and also in plasma-arc refining of metals. The surface being treated is, as a rule, anode. In this connection it is very actual to define the structure of energy transfer, consisting in finding heat flows transferred by separate particles (atoms, electrons and ions). Characteristics of near-anode region depend greatly on temperature boundary layer. Calculations of a channel arc in argon [1, 2] revealed a significant thermal and ionization non-equilibrium in near-wall layers of plasma. Investigations of near-anode region, accounting for thermal [3], and also ionization non-equilibrium [4, 5], showed that the anode drop is negative and this is correlated with results of probe measurements of V.A. Klyarfeld and N.A. Neretina [6]. However, the above-mentioned works have no information about the heat flow transfer by separate particles.

The allowance for ionization non-equilibrium gives the most complete definition of processes of energy transfer. However, this calculation is complicated by presetting boundary conditions at external and internal boundaries of the temperature boundary layer. It is possible to solve this problem only by using successive approximations as both the thickness of the temperature layer and also the plasma temperature at its external boundary depend on Joule heat evolution and density of discharge current. In work [4] the difference between the electron and nuclear temperatures at the external boundary of layer occurred to be higher than that in a near-wall zone due to the non-precise selection of boundary conditions, and this is not correct. It should be noted that the approximation $T_e = T = \text{const}$ [7], used for calculation of the ionization non-equilibrium, is not fulfilled in the near-anode zone.

The aim of the present work is to determine the energy fluxes which are transferred to the anode by electrons, atoms and ions and also to develop a model of the near-anode zone with allowance for thermal and ionization non-equilibrium of plasma.

Analysis of processes in near-anode region prove the need in a combined solution of equations of diffusion and heat conductivity of electron and ion components of plasma. Equations for current density of electrons [4, 5]

$$j_e = -eD_e \frac{dn_e}{dy} + \sigma_e \frac{d\varphi}{dy} \qquad (1)$$

and ions

$$j_i = -eD_i \frac{dn_i}{dy} - \sigma_i \frac{d\varphi}{dy} \qquad (2)$$

take into account the gradient and field diffusion of charged particles. Here, e is the electron charge; D_e, D_i and σ_e, σ_i are the coefficients, respectively, of diffusion and electric conductivity of electrons and ions; φ is the plasma potential; n_e and n_i is the concentration of electrons and ions, respectively. It is possible with a sufficient degree of accuracy to take the equality of concentrations $n_e = n_i$ for the quasi-neutral plasma. The equation of heat conductivity of electrons takes into account the change in enthalpy flow of electrons, heat evolution in recombination, Joule heating and energy losses in radiation and collision with heavy particles [4, 5]:

$$\frac{d}{dy}\left[-\lambda_e \frac{dT_e}{dy} - j_e\left(\frac{5}{2}\frac{kT_e}{e} + u_i - \varphi\right)\right] = -w_e - u_p, \qquad (3)$$

where λ_e is the heat conductivity; T_e is the temperature of electrons; u_i is the potential of ionization; u_p is the volume radiation of plasma; w_e is the density of energy transferred by heavy particles at elastic collisions:

$$w_e = 3k \frac{m_e}{M} n_e \nu_e (T_e - T); \qquad (4)$$

k is the Boltsmann's constant; m_e and M is the mass, respectively, of electrons and heavy particles (ions and atoms); T is the temperature of atoms; ν_e is the frequency of collisions of electrons with a heavy component of plasma.

Equation of heat conductivity for atoms and ions takes into account the heat inflow at collisions with electrons:

$$\frac{d}{dy}\left(-\lambda \frac{dT}{dy}\right) = w_e. \quad (5)$$

Equation of balance of ions flow in ionization and recombination of particles [4, 5, 7] has a form

$$\frac{dj_i}{edy} = K_i n_e n_a - K_r n_i n_e^2, \quad (6)$$

where K_i, K_r are the coefficients of ionization and recombination, respectively; n_a is the concentration of atoms. In the condition of ionization equilibrium when the rate of ionization and recombination are equal, there is a relation between the coefficients

$$K_i = K_r \frac{n_{e0}^2}{n_{a0}}, \quad (7)$$

where n_{e0} and n_{a0} are the equilibrium concentrations of electrons and atoms, respectively, calculated by Saha's formula. To determine the concentrations of particles the Dalton's equation for the sum of partial pressures is used:

$$P = k[(n_a + n_i)T + n_e T_e].$$

To solve the system of equations (1)–(3), (5), (6), the definition (7) of boundary conditions is required. At the external boundary of the diffusion layer at $y = \delta$, from which a numerical calculation was started, the zero gradient of concentration of electrons, definite difference of concentration of electrons from equilibrium value, difference of temperature of heavy particles from the temperature of electrons, as well as beginning of the potential counting were preset. At the absence of gradients the level of electron temperature was found from equations (3) and (4) depending on the density of discharge current. At the interface of a diffusion layer with the anode surface at $y = l_i$, where $l_i = 10^{-7}$ m is the length of a free path of ion [4], the gradient of concentration of ions, temperature of heavy particles equal to the temperature of electrode surface, and heat flow $q_e + j_e(-\varphi_0 + 5kT_e/2e)$, rushed away by electrons through a potential barrier φ_0 in Knudsen layer of thickness equal to the length of a free path of ion l_i, were preset (Figure 1).

Thus, the properties of boundary conditions can be written in the following form:

at $y = \delta$

$$\frac{dn_e}{dy} = 0, \quad n_e = 0.9n_{e0},$$
$$T = K_{th} T_e(j_e), \quad (8)$$
$$\varphi = 0;$$

at $y = l_i$

$$\frac{dn_i}{dy} = \frac{n_i}{l_i}, \quad (9)$$

$$T = T_w, \quad (10)$$

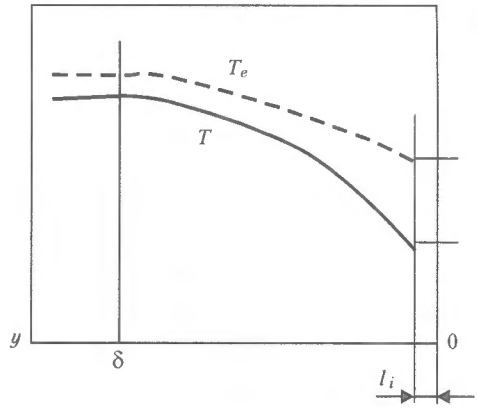

Figure 1. Scheme of boundary conditions for calculation of near-anode region of discharge

$$-\lambda_e \frac{dT_e}{dy} = j_e(\varphi_0 + 5kT_e/2e).$$

Completion of calculation of diffusion layer occurs in fulfillment of the boundary condition (9), when the gradient of concentration of ions reaches the ratio of concentration of ions to the length of a free path. Here, the degree of surface ionization of atoms is neglected.

In the boundary condition (8) the difference of temperature of heavy particles from the temperature of electrons is taken into account using the coefficient of a thermal non-uniformity $K_{th} < 1$. The value of this coefficient was selected in such a way that in integration of equation of heat conductivity for heavy particles (5) their temperature was reduced to the temperature of anode surface preset by the condition (10). It should be noted that with increase in coefficient K_{th} the thickness of temperature layer is increased. Electron temperature in the condition (8) was determined depending on the preset discharge current in accordance with equations (1), (3) and (4) at zero gradients of temperature.

Let us evaluate the validity of above-taken assumption about a low degree of surface ionization which corresponds to the boundary condition (9). The degree of surface ionization is determined by formula of Saha–Langmuir [8]:

$$\left(\frac{n_i}{n}\right)_w = \frac{g_i}{g_a} \exp[(\Phi - E_i)/kT],$$

where g_i/g_a is the ratio of statistic weights of ion and atom; Φ is the work function of an electron; E_i is the potential of ionization of atoms.

Thus, the evaluation of degree of surface ionization for argon shows that at electrode temperature T = = 3000 K, the work function Φ = 4.5 eV, potential of argon ionization E_i = 15.7 eV, we obtain n_i/n_a = = 10^{-18} that allows us to neglect the concentration of ions at the metal surface.

Parameter of the calculation is the discharge current density

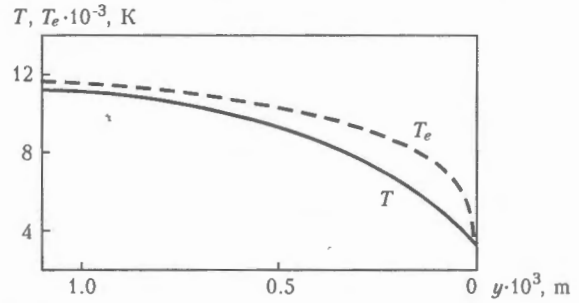

Figure 2. Nature of distribution of temperature of atoms T and electrons T_e of plasma at current density $j = 4 \cdot 10^6$ A/m^2

$$j = j_i - j_e,$$

which presets the level of temperature of plasma electrons.

Potential drop in Knudsen layer is the following [9]:

$$\varphi_0 = -\frac{kT_e}{e} \ln \frac{j_{e.ch}}{|j| + j_i + j_e},$$

where $j_{e.ch} = en_e v_e/4$ is the chaotic current of electrons at the anode; j_e is the current of emission of electrons from the anode surface. When the chaotic current of electrons prevails over the sum of discharge ion and emission currents the anode drop becomes negative. Role of negative anode drop consists in limitation of chaotic current of electrons from plasma to the level required for the balance of currents. At insufficient chaotic current of electrons the anode drop becomes positive.

Numerical solution of the considered system of equations with preset boundary conditions defines the structure of heat flow at the anode surface and distribution of parameters of plasma in the diffusion layer. Figure 2 shows the distribution of temperature of electrons and atoms at current density $j = 4 \cdot 10^6$ A/m^2 in argon plasma, while Figure 3 shows the distribution of concentration of electrons and its comparison with equilibrium concentration, defined by Saha's formula. As follows from Figure 2, the temperature of electrons exceeds significantly the temperature of heavy particles in near-wall low-temperature zone where the concentration of electrons is

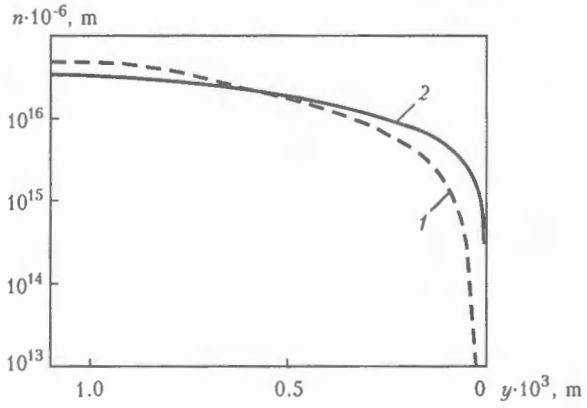

Figure 3. Change in equilibrium n_{e0} (*1*) and non-equilibrium n_e (*2*) concentrations of electrons in near-anode zone at current density $j = 4 \cdot 10^6$ A/m^2

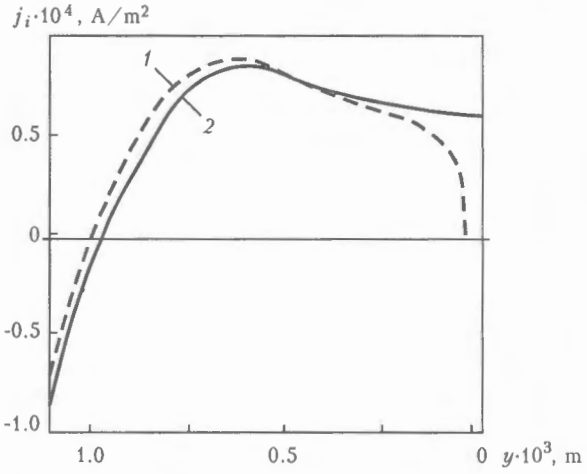

Figure 4. Change in ion current in equilibrium (*1*) and non-equilibrium (*2*) plasma of boundary layer

higher than the equilibrium value by several orders (see Figure 3). For example, the equilibrium concentration and electric conductivity of electrons in the layer of $5 \cdot 10^{-5}$ m thickness is lower than actual values by more than two orders.

Therefore, if not to take into account the non-equilibrium of plasma, then the ohmic drop of voltage, determined by the resistance of plasma in a near-wall zone, occurred to be hundred times higher and will be hundreds of volts. Concentration of ions depends on processes of ionization, occurring in external high-temperature part of the anode zone, and processes of recombination in low-temperature near-wall zone. In spite of the fact that sizes of these zones are approximately similar, the intensity of ionization and increase in ion current in the ionization zone is much higher than the decrease in ion current in the recombination zone (Figure 4). Allowance for distribution of temperature reduces the density of ion current by an order as compared with the case T_e = const. Distribution of potential is determined not only by ohmic resistance of plasma, but also by concentration diffusion of electrons. As the flow of diffusion is higher than the discharge current, the anode drop is negative both in diffusion zone and also in non-collision layer.

Heat flows transferred by atoms q_a, electrons q_e and ions q_i were determined by the following formulae:

$$q_a = \lambda w \left(\frac{dT}{dy}\right)_w,$$

$$q_e = \frac{5}{2}\frac{k}{e} j_e (T_{ew} - 293), \qquad (11)$$

$$q_i = j_{iw}(u_i + \varphi_0).$$

In formula (11) the cooling of electron gas to room temperature $T_0 = 293$ K is taken into account. Index w denotes near-wall parameters of plasma. The full heat flow is determined usually by a volt equivalent of heat flow

$$U^T = \Phi + \frac{q_a + q_e + q_i}{j}.$$

Results of calculation are given in Table for a steel anode with temperature T_w = 2800 K and work function Φ = 4.3 eV.

Heat transfer of electrons is approximately 2 times higher than that of atoms. In spite of a small share of energy of ions in a common heat flow, their effect on surface refining can occur to be significant.

Experimental measured value U^T is (5.6–6.0) V [10, 11] that is correlated satisfactory with a design value.

CONCLUSIONS

1. Calculations confirmed the presence of a local thermodynamic equilibrium of plasma only in a high-temperature zone of a boundary layer, whereas in a near-wall low-temperature zone the concentration of electrons is occurred to be much higher than the equilibrium concentration determined by electron temperature due to equalizing its level by the diffusion flow.

2. In near-wall part of the boundary layer the existence of a recombination zone was revealed, at the interface of which the ion current reaches maximum, while in the zone itself its negligible reduction takes place.

3. It is shown that the recombination of ions is occurred also at the anode surface as the negative anode drop of voltage leads to the movement of ions to its surface.

Results of calculation of parameters of energy transfer at anode

$j \cdot 10^{-4}$, A/m^2	$j_i \cdot 10^4$, A/m^2	T_{ew}, K	q_a/j, V	q_e/j, V	q_i/j, V	U^T, V
200	0.27	3900	0.48	0.78	0.022	5.67
400	0.55	3700	0.48	0.74	0.022	5.63
800	1.10	4400	0.49	0.89	0.022	5.80
1600	2.60	4900	0.50	0.99	0.024	5.97

1. Kruger, Ch.H. (1970) Non-equilibrium in confined arc plasma. *Phys. Fluids*, 13(7), 1737–1746.
2. Ulenbush, J. (1973) Study of non-equilibrium of arc plasma. *Izvestiya SO AN SSSR*. Technical Sciences Series, 3(13), 27–39.
3. Gorchakov, V.S., Nazarenko, I.P., Panevin, I.G. et al. (1977) Results of calculation of parameters of near-anode layer in arc discharge. In: *Proc. of 7th All-Union Conf. on Low-Temperature Plasma Generators*, Alma-Ata, May, 1977. Vol. 2.
4. Panevin, I.G., Nazarenko, I.P., Ershov, A.V. (1977) Study of near-anode processes in high-current discharges of high-pressure. In: *Experimental studies of plasmatrons*. Ed. by M.F. Zhukov. Novosibirsk: Nauka.
5. Panevin, I.G., Khvesyuk, V.I., Nazarenko, I.P. et al. (1992) *Theory and calculation of near-electrode processes*. Novosibirsk: Nauka.
6. Klyarfeld, V.A., Neretina, N.A. (1958, 1959, 1960) Anode region in gas discharge at low pressures. Part 1. *Zhurnal Tekhnich. Fiziki*, 28(2), 48–50; Part 2. *Ibid.*, 29(1), 36–46; Part 3. *Ibid.*, 30(3), 12–18.
7. Bejlis, I.I., Lyubimov, G.A., Rakhovsky, V.I. (1972) Diffusion model of near-cathode region of high-current arc discharge. *Doklady AN SSSR*, 203(1), 71–74.
8. Dobretsov, L.N., Gomoyunova, M.V. (1966) *Emission electronics*. Moscow: Nauka.
9. Lyubimov, G.A. (1963) Change of electric potential near the wall of channel in ionised gas movement in magnetic field. *Zhurnal Prikl. Mekhaniki i Teoret. Fiziki*, 5, 24–31.
10. Zheenbaev, Zh., Kobtsev, G.A., Konavko, R.I. et al. (1972) Optimisation of anode unit with argon shielding. In: *Abstr. of pap. of 5th All-Union Conf. on Low-Temperature Plasma Generators*, Novosibirsk, 1972. Vol. 2.
11. Anshakov, A.S., Dandaron, G.-N.B., Vastyuk, V.K. et al. (1977) Study of heat flow to anode. In: *Abstr. of pap. of 7th All-Union Conf. on Low-Temperature Plasma Generators*, Alma-Ata, May, 1977. Vol. 2.

APPLICATION OF ADAPTIVE ALGORITHM FOR WELDING QUALITY MONITORING IN CONTROL SYSTEMS OF RESISTANCE SPOT WELDING MACHINES

N.V. PODOLA, P.M. RUDENKO and **V.S. GAVRISH**
E.O. Paton Electric Welding Institute, NASU, Kiev, Ukraine

Peculiarities of application of the adaptive algorithm of neuron networks in resistance spot welding control systems based on microcontroller are considered. To simplify the required calculations at preset accuracy of control, the neuron network with input process parameters in relative units is suggested.

Keywords: *resistance spot welding, nugget diameter, weld spot, microcontroller, neuron network, adaptation, algorithm*

In control systems of resistance spot machines the single-crystal eight-digit controllers of MCS51 type, providing the sufficient accuracy of the process control, are usually used. When the neuron networks are used in these controllers for welding quality monitoring, the required accuracy of prediction of weld spot nugget diameter D_{nugg} can be attained by using an adaptive algorithm [1, 2]. In this case the variables, expressed in natural units, are supplied to the neuron network input.

Calculation of weight factors and threshold values of neuron networks is made in a personal computer using floating-point computations. In a single-crystal controller the use of this calculation for computation of weld spot nugget diameter using the neuron network takes much time and is not correlated with a high efficiency of the resistance machines. The aim of the work is to evaluate the efficiency of applying the adaptive algorithm of mains to decrease the duration of calculation of neuron network without loss in accuracy of prediction.

At one and the same structure of the neuron network the weight factors and its threshold values are determined by the parameters of the welding conditions, such as welding current, diameter of test surface of the electrodes, voltage at electrodes. To avoid the storage of large files of data about the weight factors and threshold values in memory, the algorithm of their restructuring was suggested [2, 3]: in change of conditions the weight factors, threshold values and structure of a basic model remain constant, while the input variables are recalculated by a linear law in such a way that to preserve the previuos region of model definition:

$$I_n = A_1 I + B_1; \quad U_n = A_2 U + B_2, \tag{1}$$

where I_n and U_n are, respectively, the values of welding current and voltage between the electrodes, supplied to the input of neuron network; I and U are the measured values of the same parameters.

Coefficients and free terms in relationships (1) are calculated coming from allowable deviations of parameters of basic and new conditions of welding:

$$\begin{aligned} A_1 &= (I_{b.max} - I_{b.min})/(I_{max} - I_{min}); \\ B_1 &= I_{b.max} - A_1 I_{max}; \\ A_2 &= (U_{b.max} - U_{b.min})/(U_{max} - U_{min}); \\ B_2 &= U_{b.max} - A_2 U_{max}, \end{aligned} \tag{2}$$

where $I_{b.max}$, $I_{b.min}$, $U_{b.max}$, $U_{b.min}$ are the maximum and minimum values of a range of changing welding current and voltage between electrodes of the basic condition; I_{max}, I_{min}, U_{max}, U_{min} are the same values for the new condition.

In addition, the similar linear transformation is used for an output value, i.e. diameter of the weld spot nugget:

$$D_{nugg} = A_3 D_b + B_3,$$

where D_b is the diameter of weld spot nugget at the basic condition;

$$\begin{aligned} A_3 &= (D_{max} - D_{min})/(D_{b.max} - D_{b.min}); \\ B_3 &= D_{max} - A_3 D_{b.min}, \end{aligned} \tag{3}$$

where D_{min} and D_{max} are the measured values of nugget diameter, respectively, at I_{min}, U_{min} and I_{max}, U_{max}; $D_{b.min}$ and $D_{b.max}$ are the output minimum and maximum values of neuron network at substituting of values I_{min}, U_{min} and I_{max}, U_{max}, recalculated by (1), to its input.

Application of the above-described algorithm in the control system of resistance machine could provide the error in prediction of weld spot nugget diameter of not more than 10 % in welding low-carbon steel with a packet thickness from (0.8 + 0.8) up to (2.0 + + 2.0) mm. Here, the accuracy of recalculated model depends on the proper selection of parameters D_{min}, D_{max}, I_{min}, U_{min}, I_{max}, U_{max} in (2) and (3), at which the values of weld spot nugget diameter are changed from minimum to maximum allowable value in selection of the new welding conditions. When selecting these parameters, it is necessary to take into account the error of reproducibility of experimental data. It is impossible in data accumulation to increase succes-

sively the accuracy of resetting. In the restructured model the data in the centre of the definition region are not taken into account, but it is the region where there is the highest probability of the process proceeding.

It is evident that experiments and computations are simplified greatly in case, if the input variables of the neuron network are in a single range of values. Their representation in relative units is the simplest method to reduce input parameters of the spot welding process to the close numerical values

$$X' = (X - X_{opt})/X_{opt},$$

where X is the current values, while X_{opt} are the optimum values of parameters.

It is known that, independently of the thickness of parts welded, the relative change in welding condition parameters (current, compression force of electrodes) should not exceed the preset values by ±5 % in current and by ±10 % in electrode compression force to provide the quality welded joint. In other words, when the spot welding process parameters are presented in relative units, the regions of changing the input values are superimposed one on another and coincide very often.

It is known that the normalizing of input data is used usually in computation of parameters of the neuron network that is in fact their estimate in relative units:

$$X'' = (X - X_{av})/X_{e.r},$$

where $X_{av} = 0.5(X_{max} + X_{min})$ is the average value of range of changing input data of network variables; $X_{e.r} = 0.3(X_{max} - X_{min})$ is the estimation of this range limits.

Assuming that $X_{av} = X_{opt}$ usually, it is possible to suppose that

$$X'' = X'X_{opt}/X_{e.r},$$

and the normalized value of output is the value of weld spot nugget diameter

$$D'' = D_{nugg}/(1.1D_{max}).$$

In calculation of neuron network with input variables in relative units the need in their normalization is avoided that promotes the increase in rate of the algorithm convergence [4]. At control of the process of welding, performed using the new condition, it is necessary to select new optimum values of parameters of condition $X_{opt.new}$ and weld spot nugget diameter $D_{opt.new}$. Further, relative values X' should be substituted to the network and scale factor at the basic

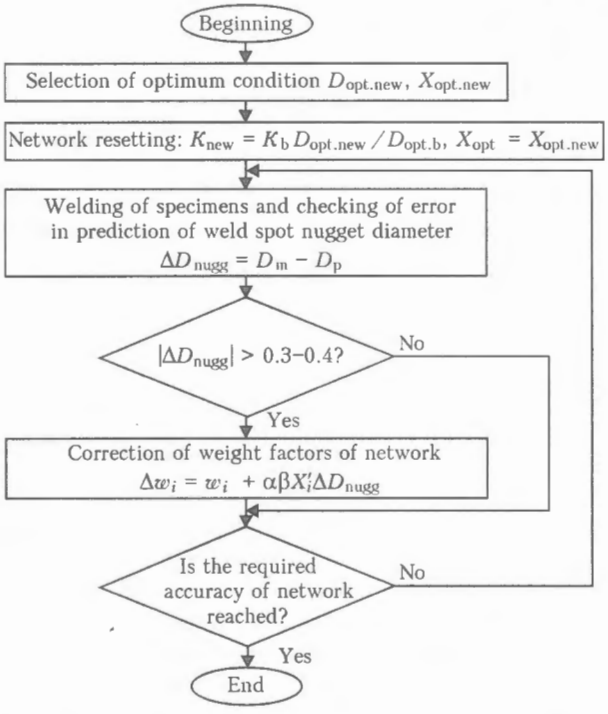

Figure 1. Algorithm of adaptation of neuron network with input parameters in relative units (see designations in the text)

neuron network K_b should be changed proportionally to the change of optimum values of nugget diameter at basic $D_{opt.b}$ and new condition $D_{opt.new}$:

$$K_n = K_b D_{opt.new}/D_{opt.b}. \quad (4)$$

Algorithm of restructuring (Figure 1) of neuron networks with input parameters in relative units was checked in welding of parts of low-carbon steel with a packet thickness (0.8 + 0.8), (1.2 + 1.2) and (2.0 + + 2.0) mm.

Optimum conditions of welding were selected taking into account the recommendations of the International Institute of Welding (Table). The scope of investigation of the process was from $0.5D_{opt.new}$ to $1.1D_{opt.new}$ (until appearance of splash). At optimum condition the welding current and voltage between the electrodes was changed within the −20 – +5 % range, the compression force of electrodes — by +50 %, diameter of test surface of electrodes — by +50 %.

The basic neuron network was constructed for welding a packet of thickness (1.2 + 1.2) mm. Input parameters of the neuron network were their relative values X'. Then, the coefficient at output of basic neuron network K_b for the new network K_{new} was changed by relationship (4) for packets of thickness (0.8 + 0.8) and (2.0 + 2.0) mm using optimum pa-

Thickness of packet, mm	*Welding current, kA*			*Welding duration, period*	*Compression force, daN*	*Nugget diameter, mm*
	Basic	*Minimum*	*Maximum*			
1.2 + 1.2 (basic network)	8.9	5.9	9.9	10	370	5.4
0.8 + 0.8	8.2	6.5	9.8	8	320	4.6
2.0 + 2.0	12.1	8.7	13.2	12	550	6.9

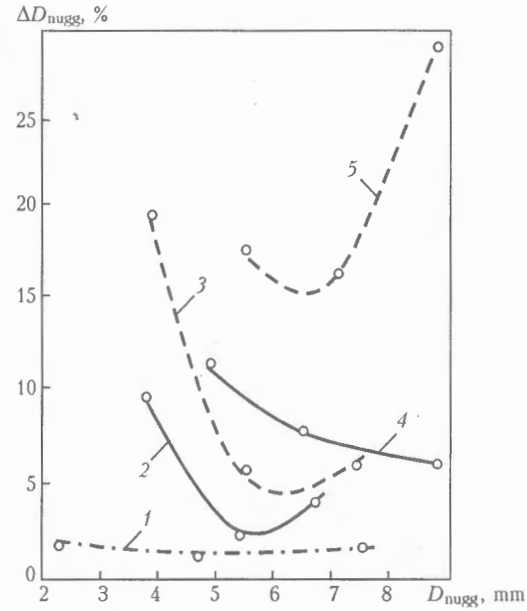

Figure 2. Error ΔD_{nugg} of prediction of diameter of weld spot nugget D_{nugg} in welding parts from low-carbon steel with a different thickness of packet: *1* — (1.2 + 1.2) mm — basic condition; *2, 3* — (0.8 + 0.8) mm; *4, 5* — (1.2 + 1.2) mm; *solid curves* — with adaptation; *dashed lines* — without it

rameters of basic condition $I_{opt.b}$, $U_{opt.b}$ and $D_{opt.b}$ and new optimum condition $I_{opt.new}$, $U_{opt.new}$ and $D_{opt.new}$.

It is evident that at optimum parameters of welding condition the error of prediction is determined by the error of reproducibility of the experiment: maximum error should be expected at the periphery of the required region of welding process definition. This error will be higher at the larger violation of the similarity of welding processes at basic and new conditions.

The increase in error of prediction of the welding process in the region of condition parameters at which the nugget diameter is larger than $D_{opt.new}$, is not hazardous, as the rejected joint for the welded joint quality monitoring in this region can be evaluated by the appearance of a splash (if the splashes are not admissible), which is determined with a high validity by voltage drop between the electrodes. In addition, if to come from the condition of selection of optimum condition, then this region is so small usually that the appearance of a significant error in it is improbable.

Another situation with an increase in error in the region of a minimum allowable nugget diameter D_{min}. Here, and removal from point $D_{opt.new}$ will be larger and the accuracy of prediction should be high for distinguishing the non-quality welded joint. To increase the accuracy of welding process definition at values of condition parameters at which the nugget diameter is approaching D_{min}, it is possible to use data in this point for resetting the neuron network. In experiments this point was obtained at a simultaneous decrease in mains voltage by −10 – −20 %, increase in compression force of electrodes by +20 – +50 %, and the diameter of test surface of electrodes — by +50 %.

Using error of weld spot nugget diameter $\Delta D_{nugg} = D_m - D_p$ (where D_m and D_p are the measured and predicted values of nugget diameter, respectively), the weight factors of mains were corrected:

$$\Delta w_i = w_i + \alpha\beta X_i' \Delta D_{nugg}, \qquad (5)$$

where $\alpha = 0.1$ is the coefficient of averaging; β is the coefficient determined by a predicted value of nugget diameter from the algorithm of neuron network teaching. In our case algorithm with an error of «back propagation» type was used for the neuron network teaching.

The described algorithm was checked at different conditions of welding parts with an indicated range of a packet thickness. Optimum parameters of the condition were selected at different time of welding. To decrease the errors less than by 10 % the correctness of weight coefficients of mains by (5) in two cases from nine cases was not necessary, in six cases welding of one spot was sufficient, and in one case two spots were sufficient to clarify the coefficients w_i (Figure 2).

The given adaptive algorithm and used structure of the neuron network are more convenient for realization in single-crystal controllers, when the digit network is limited by 8 bites as compared with a calculation using input parameters in natural units as the scaling of input variables is simplified. In calculations of neuron networks and their checking in personal computer the computations with a floating point are used with almost unlimited accuracy of representation of input values of parameters and results of intermediate computations for the set problem.

In a single-crystal controller the application of arithmetical operations with a floating point in computations by neuron networks is not rational as a lot of time is spent for calculations as a compared with a high efficiency of the resistance welding machines. It is evident that the calculations in the single-crystal computer should be realized in the condition of a fixed point. The main length of a word in these computers is 8 bits, i.e. initial data, coefficients and results of intermediate calculations are within the range of −27 – +127. By complicating the algorithms of calculations it is possible to increase the digit network, however, the volume of memory and time of calculations of program in this case are increased. Minimum volume of memory was selected as a criterion of optimality of computational algorithm for its realization at error of computations of not more than 0.1–0.2 mm as compared with the neuron network, constructed without limitations in calculation of weight factors and threshold values of the neuron network.

When programming the neuron network, it is necessary to select the capacity of representation of weight factors and threshold values, accuracy of representation of a sigmoid function and performance of intermediate computations, in particular accumulation of a subsigmoid sum. Evaluation of capacity of

representation of coefficients and threshold values of the network was realized using the calculation of neuron network using the same experimental data with a limitation of digit network from 7 to more bits.

The network, calculated without limitation of variables, was taken as a basic neuron network for evaluation of error of the process definition.

It follows from the calculations made that the acceptable accuracy of definition of the process of the resistance spot welding using the neuron network of the selected structure is attained in limitation of its parameters up to ±512. The increase in accuracy of representation up to ±1024 does not almost increase the accuracy of calculation of the weld spot nugget diameter, and reduction to ±256 decreases the accuracy of prediction. Thus, such neuron networks were considered later, whose variables were within the range of −512 – +512 (10 bits).

It was taken into account in description of a sigmoid function (Figure 3) that it is symmetrical relative to point $x = 0$, $y = 1/2$ and changed at output in the 0–1 range in changing the argument in the whole range of values from $-\infty$ to $+\infty$. Region of description by argument can be limited coming from the nature of function non-linearity. Thus, at $x = 3.0$ $y = 0.952$; $x = 4.0$ $y = 0.982$; $x = 5.0$ $y = 0.993$; $x = 6.0$ $y = 0.997$; $x = 7.0$ $y = 0.999$; $x = 8.0$ $y = 0.9997$. In case of limitation of argument up to $x_{max} = 5.0$ the error of function description at the boundary of area of its determination will not exceed 1 %. Maximum error of description of sigmoid function depending on a pitch of argument change is in the vicinity of point $x = 0$ and at $1/16$ pitch it is 0.0156, at $1/32$ — 0.0078, at $1/64$ — 0.0039, i.e. pitch $1/32$ provides the description error of not worse than 1 %. To describe the sigmoid function with an accuracy of not worse than 1 % and in the form convenient for realization in single-crystal controllers, the argument was presented in the form of 9-bit number, including one sign digit, with $1/2$ discreteness of argument changing. The error of approximation here is changed from 0.0078 (in the centre) to 0.004 (at the ends of definition area).

Maximum value of subsigmoid expression depending on maximum value of input variables (255 or 8 bits), maximum values of weight factors and threshold values (±512 or 10 bits), and also a number of summands in subsigmoid expression (4) is 8 + 10 + + 3 = 21 bits. Thus, the subsigmoid sum should be considered as a 3-bit number.

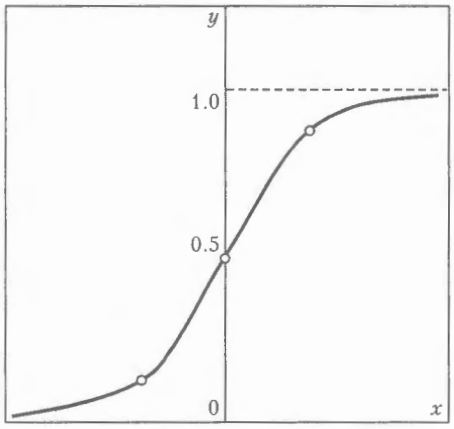

Figure 3. Sigmoid function

The described limitations in intermediate calculations are proved by the results of experiments on welding low-carbon steel, which were compared with calculations made in the floating point conditions. The error of prediction of nugget diameter here was not more than 0.1 mm.

Thus, the algorithm suggested is very simple for use in change of the condition, there is a feasibility to accumulate results of experiments and to increase the accuracy of setting the neuron network in definite points of the preset region of conditions. As a whole, the algorithm in relative units allows monitoring of the welding quality within a wide range of thickness of materials welded without conductance of a large number of experiments for the construction of the neuron network.

1. Paton, B.E., Podola, N.V., Gavrish, V.S. et al. (1999) Automatic evaluation of quality of resistance spot welding using the neuron networks. *Avtomatich. Svarka*, **12**, 3–8.
2. Podola, N.V., Rudenko, P.M., Gavrish, V.S. (2002) Adaptive algorithm of quality control of resistance spot welding using neural networks. *The Paton Welding J.*, **1**, 44–46.
3. Podola, N.V., Gavrish, V.S., Rudenko, P.M. (1999) Adaptive system of control of resistance spot welding process of low-carbon steel. *Avtomatich. Svarka*, **6**, 3–5.
4. Rajbman, N.S., Chadeev, V.M. (1975) *Construction of models for control of production process*. Moscow: Energiya.

MECHANICAL PROPERTIES AND FRACTURE TOUGHNESS OF WELDED JOINTS OF A WWER-1000 REACTOR

A.S. ZUBCHENKO, G.S. VASILCHENKO, E.G. STARCHENKO and S.I. NOSOV
FGUP «TsNIITMASh», Moscow, Russia

Effect of nickel content in weld metal of steel 15Kh2NMFAA welded joints on their brittle fracture susceptibility has been studied, in particular after radiation exposure. It is shown that mechanical properties of weld metal with nickel content of not more than 1.3 % are not lower that those given in the specification. It is recommended that the design of reactors for brittle fracture resistance should be performed on the basis of fracture toughness of welded joints, using a standard curve.

Keywords: *arc welding, low-alloyed steel, reactor body, welded joints, mechanical properties, brittleness, fracture toughness*

Automatic welding of batch-produced bodies of WWER-1000 reactors made of steels of grades 15Kh2NMFA and 15Kh2NMFAA was performed using Sv-12Kh2N2MAA wire in combination with FTs-16 and FTs-16A flux. In this case, 1.2–1.9 % Ni was provided in the weld metal. Studies to assess the influence of nickel content on weld metal susceptibility to brittle fracture, also after irradiation, were conducted to more precisely determine the role of nickel in performance of reactor body metal. Investigations were performed using commercial batches of welding wire Sv-12Kh2N2MAA with 1.25 and 1.6 % Ni (melts 178058 and 179687), and a test batch of wire was made with 2.48 % Ni (content of other elements being on the level of specification requirements for Sv-12Kh2N2MAA wire). Welded joints 190 mm thick were made in keeping with the standard requirements for welding and heat treatment of 15Kh2NMFAA steel. Composition, impact toughness and critical brittleness temperature of the metal of welded joints are given in Tables 1 and 2.

Radiation resistance of weld metal was studied by the procedure of Institute of Nuclear Power Engineering. Radiation embrittlement of weld metal with different content of nickel was studied by the shift of critical brittleness temperature ΔT_F after irradiation with the fluence of $(24–260)\cdot10^{22}$ N/m^2 at $E >$ > 0.5 MeV. Testing results showed that the observed correlation between the value of standard fluence and shift T_{c0} of weld metal is close to the linear one (Figure 1). Data was confirmed, which shows that shift ΔT_F of weld metal with nickel content of more than 1.3 % (similar to that below 1.3 %) after exposure to fluence, corresponding to the design dose over 40 years of operation of WWER-1000 reactor ($\leq 64\cdot10^{22}$ N/m^2), does not exceed values guaranteed by the certification report. Influence of nickel on radiation embrittlement becomes stronger at fluence value much greater than the design value. A decision was taken to correct the

Table 1. Composition of weld metal

No. of wire melt, flux batch	*Weight fraction of elements, %*								
	C	*Si*	*Mn*	*Cr*	*Ni*	*Mo*	*S*	*P*	*Cu*
178058, 139	0.064	0.25	1.08	1.60	1.28	0.55	0.011	0.009	0.055
179687, 69	0.065	0.32	0.86	1.83	1.60	0.60	0.006	0.007	0.060
Test melt, 139	0.078	0.27	1.10	1.68	2.45	0.65	0.007	0.006	0.030
22554, 235	0.080	0.30	0.75	2.00	1.10	0.62	0.012	0.006	0.040

Table 2. Properties of weld metal after tempering

No. of wire melt, flux batch	*Critical brittleness temperature, °C*	*Impact toughness at 20 °C, J/cm²*
178058, 139	–30 – –40	180–190
179687, 69	–30 – –40	143–193
Test melt, 139	–20 – –30	150–170

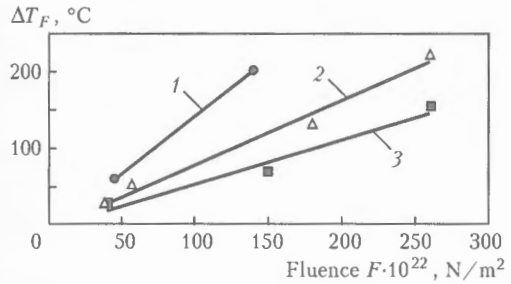

Figure 1. Radiation embrittlement of weld metal at different content of nickel at $E > 0.5$ MeV: 2.45 (*1*); 1.60 (*2*); 1.28 (*3*) % Ni

composition of welding wire Sv-12Kh2N2MAA in terms of lowering the content of nickel in it to approximately 1.3 % at a simultaneous tightening of requirements to impurity element content (≤ 0.006 % P, ≤ 0.006 % S, ≤ 0.06 % Cu).

In order to study the characteristics of brittle fracture resistance of the metal of a weld made with a commercial batch of wire Sv-12Kh2N2MAA (22554 melt) of a corrected composition, Company «Izhorskie zavody» made welded joints of steel 15Kh2NMFA 250 mm thick. They were used to prepare specimens for testing at the temperature of 20 and 350 °C, specimens with a Charpy notch for impact testing, as well as compact CT-1T and CT-4T specimens.

Welding was followed by heat treatment by a standard mode 620 °C (25 h) + 650 °C (20 h). Blanks for making the templates and specimens were cut out mechanically, in keeping with the technical requirements given in the drawings and process charts for cutting out specimens from the reference welded joints. Results of specimen testing are given in Table 3, from which it is seen that all of them satisfy the standard requirements. Deformation curves recorded at tensile testing of specimens were used for plotting Ramberg–Ostgud curves at the temperature of 20 (Figure 2, *a*) and 350 °C (Figure 2, *b*).

Impact testing specimens with a Charpy notch in the weld metal were tested in impact testing machine PSW-300 in the temperature range from +20 up to −40 °C. Figure 3 gives experimental values for all 20 specimens and temperature dependencies of average values of impact toughness and minimum values of the percentage of tough component in the fractures. Comparison of the plotted curves with the criteria values in keeping with the regulations set forth in document [1], enabled determination of the critical brittleness temperature of weld metal T_c = −20 °C,

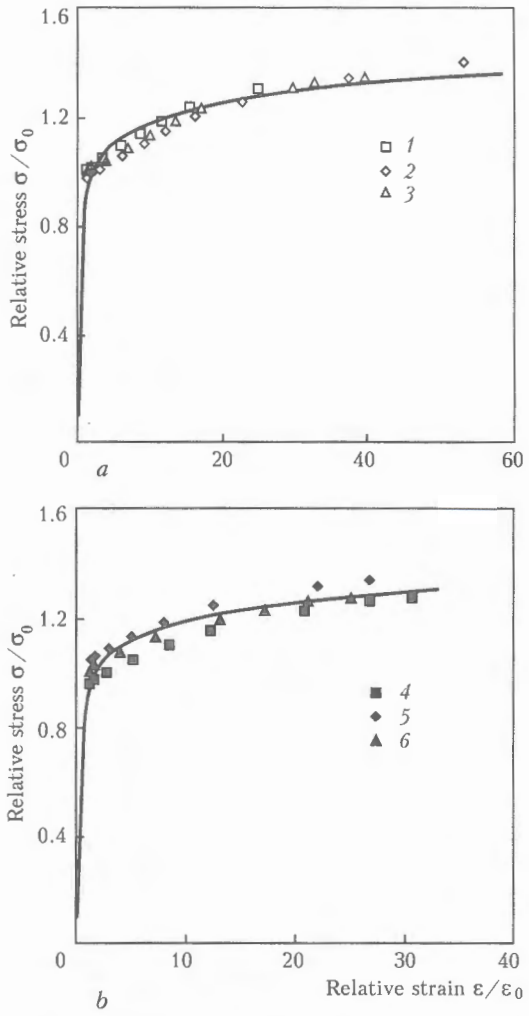

Figure 2. Diagram of weld metal deformation at 20 (*a*) and 350 (*b*) °C and its approximation by Ramberg–Ostgud method (curve is Ramberg–Ostgud approximation): *a* — $\varepsilon/\varepsilon_0 = \sigma/\sigma_0 + 1.048(\sigma/\sigma_0)^{12.7}$, σ_0 = 470.2 MPa, ε_0 = 0.224 %; *b* — $\varepsilon/\varepsilon_0 = \sigma/\sigma_0 + 0.891(\sigma/\sigma_0)^{13.67}$, σ_0 = 406.4 MPa, ε_0 = 0.214 %; *1–6* — specimen numbers

which is much lower than the standard requirement to the metal of welds of WWER-1000 reactors (T_c = = 0 °C).

Results of impact testing of Charpy specimens further allowed evaluation of the temperature for testing compact specimens CT-1T [2] (for which the average value of fracture toughness K_{JC} = 100 MPa$\sqrt{\text{m}}$)

$$T_c = T_{28}^{*}{}_J + C, \qquad (1)$$

Table 3. Mechanical properties of weld metal specimens

Specimen No.	*Test temperature, °C*	*Yield point, MPa*	*Ultimate strength, MPa*	*Elongation, %*	*Reduction in area, %*
1 2 3	20	$\frac{484–494}{3 \times 488}$ (422)	$\frac{588–591}{3 \times 589}$ (539)	$\frac{22.6–25.0}{3 \times 23.5}$ (15.0)	$\frac{73.1–75.0}{3 \times 73.7}$ (55.0)
4 5 6	350	$\frac{412–450}{3 \times 428}$ (392)	$\frac{491–518}{3 \times 499}$ (490)	$\frac{15.8–18.2}{3 \times 17.2}$ (17.0)	$\frac{67.8–69.5}{3 \times 68.5}$ (50.0)

Notes. 1. The numerator gives the scatter of values, the denominator gives the average. 2. Standard required values are given in brackets.

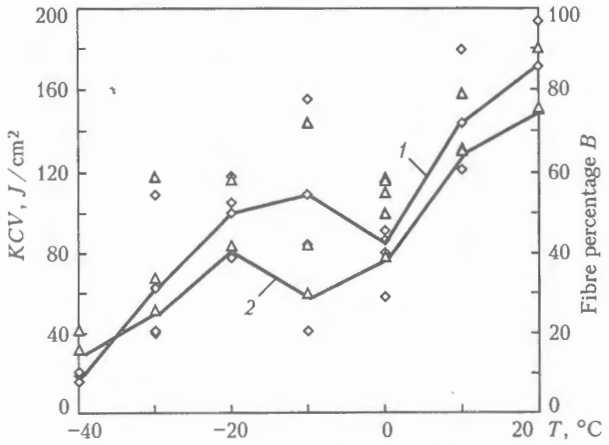

Figure 3. Dependence of average *KCV* values (*1*) and minimum values of fibre percentage (*2*) on temperature

where C is the correction for Charpy specimens equal to −18 °C.

Figure 3 allows evaluation of temperature $T_{28\,J}$ = = −32 °C, and, therefore, T_{test} = −50 °C.

After inducing cracks, starting from notches in keeping with the requirements of [3], testing of the first CT-1T specimens allowed determination of value $K_{JC} > 140$ MPa$\sqrt{m}$, which led to lowering of testing temperature for subsequent CT-1T specimens to T_c = = −70 °C. Testing of eight specimens (all turned out to be valid) at T = −70 °C determined the scatter of K_{JC} values at the average value of fracture toughness of the order of 100 MPa$\sqrt{m}$, which is necessary for construction of a «master-curve» [2]. Results of testing all 12 CT-1T specimens are given in Table 4.

Experimental data obtained on CT-1T specimens were processed by formulas given in the design part of the document [2]. Calculation results allowed determination of reference temperature T_0 = −60 °C for CT-1T specimens of the tested welded joint. The following equation was used for plotting the «master-curve»:

$$K_{JC} = 30 + 70 \exp [0.019(T_{test} - T_0)] \quad (\text{MPa}\sqrt{\text{m}}). \quad (2)$$

Tolerance ranges of 5 and 95 % were calculated by the following formula:

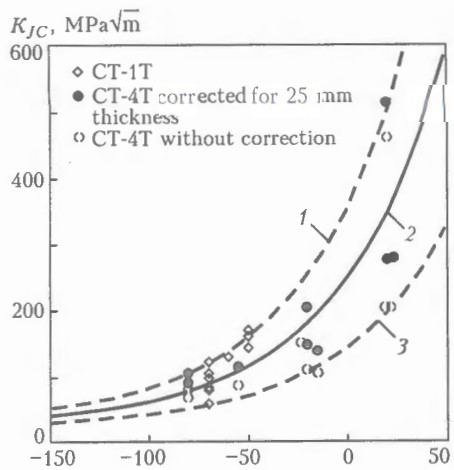

Figure 4. «Master-curve» (*2*) for weld metal with 95 (*1*) and 5 (*3*) % confidence intervals

Table 4. Results of testing CT-1T specimens

Specimen No.	*Test temperature, °C*	*Crack size, mm*	*Breaking load, N*	*Fracture toughness, MPa√m*
1	−50	24.15	6870	160.0
2	−50	24.4	6600	142.3
3	−50	24.5	6800	170.0
4	−60	24.7	6400	129.0
5	−70	27.9	6660	121.4
6	−70	24.7	3470	58.0
7	−70	24.5	5200	96.1
8	−70	24.8	5330	104.4
9	−70	26.1	5000	103.2
10	−70	24.5	5200	98.0
11	−70	24.8	4700	83.5
12	−70	25.0	4200	80.3

$$K_{JC} = D_1 + D_2 \exp [0.019(T_{test} - T_0)], \quad (3)$$

where D_1, D_2 are the reference coefficients from [2].

«Master-curve» and tolerance ranges for the studied weld metal were obtained using the results of testing CT-1T specimens (Figure 4). It is seen that practically all the experimental points fall within the selected tolerance range. Compact CT-4T specimens were made of the same welded sample, as CT-1T specimens.

Fatigue cracks were induced, using TsDM-200Pu testing machine. Initial cyclic loading up to cracks initiation on the side surfaces was conducted at maximum load P_{max} = 450 kN and minimum P_{min} = 80 kN for approximately 60,000 cycles. The last 5 mm of the crack were grown at P_{max} = 150 kN and P_{min} = = 30 kN for 50,000 cycles. After a crack has been induced, testing of CT-4T specimens was performed

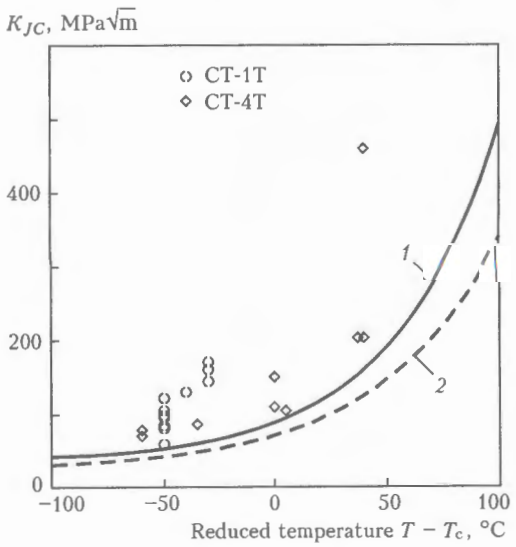

Figure 5. Comparison of the results of fracture toughness testing of CT-1T and CT-4T specimens with a standard curve for welded joints of WWER-1000 reactor bodies: *1* — standard curve $[K_I]_3$ = = 35 + 53 exp [0.0217($T - T_c$)] [1]; *2* — basic K_{JC} curve = 23 + + 48 exp [0.019($T - T_c$)] [4]

Table 5. Results of testing CT-4T specimens

Specimen No.	Test temperature, °C	Crack size, mm	Breaking load × 10^{-4}, N	Fracture toughness, MPa$\sqrt{m}$	
				Actual	Recalculated for 25 mm thickness
1	20	107.85	72.2	202.9	276.9
2	20	104.02	108.0	369.0	512.0
3	20	103.40	83.0	203.9	279.3
4	−15	104.40	46.5	103.5	138.3
5	−20	103.20	50.0	109.6	146.7
6	−20	103.90	67.6	149.8	203.1
7	−55	104.64	38.5	86.4	113.6
8	−80	104.40	37.4	80.6	105.4
9	−80	104.10	31.24	69.5	89.6

in TsDM-200Pu machine, fitted with force and displacement transducers, system of recording the specimen deformation, as well as a cryochamber for cooling specimens by liquid nitrogen vapours. Temperature of the cooled specimen was controlled continuously, using chromel-alumel thermocouples, the heads of which were welded in the zone of the end of the induced crack.

K_{JC} value of CT-4T specimens was determined allowing for the plastic component of fracture energy for only one specimen, tested at +20 °C and having by the moment of fracture a static growth of the initial fatigue crack of 2.15 mm. The other eight specimens failed without any static growth of the crack, which allowed determination of value K_{JC} just by the elastic component.

K_{JC} values obtained for CT-4T specimens were also recalculated for the thickness of CT-1T specimen by the following formula:

$$K_{1JC} = K_{min} + (K_{4JC} - K_{min})\,(B_4/B_1)^{1/4}, \qquad (4)$$

where K_{min} = 20 MPa$\sqrt{m}$; K_{1JC}, K_{4JC} and B_1, B_4 is the fracture toughness and thickness of CT-1T and CT-4T specimens, respectively.

Results of testing CT-4T specimens are given in Table 5. Measured K_{JC} values of CT-4T specimens, both the actual ones and those recalculated for the thickness of 25 mm, are given in Figure 4. Confidence intervals of 5 and 95 % of the «master-curve», obtained from the results of testing CT-1T specimens, are confirmed by the results of testing CT-4T specimens 100 mm thick, both for the actual values and those recalculated for the thickness of 25 mm (Figure 5). The Figure gives the results of testing specimens CT-1T and CT-4T, depending on temperature equal to the difference of the specimen testing temperature, and critical brittleness temperature of weld metal T_c = −20 °C. It is seen that even minimum values of fracture toughness of specimens 25 and 100 mm thick meet the requirements of the standard curve for welded joints of casing steels [1].

In conclusion it should be noted that the retrofitted standard technology, providing welds with a lower content of nickel, is recommended for fabrication of bodies of WWER-1000 and WWER-1500 reactors, and design of these reactors for brittle fracture resistance should be conducted, using the standard curve of fracture toughness of welded joints [1].

1. *PNAE G-7-002–86*. Codes for strength design of equipment and pipelines of nuclear energy plants. Moscow: Energoatomizdat.
2. *ASTM E 1921–97*. Standard method for determination of reference temperature for ferritic steels in transition range.
3. *GOST 25.506–85*. Methods of mechanical testing of materials. Determination of characteristics of crack resistance (fracture toughness) during static loading. Moscow: Gosstandart SSSR.
4. Margolin, B.Z., Shvetsova, V.A., Nikolaev, V.A. et al. (2001) *Procedure for prediction of temperature dependence of material fracture toughness in WWER-440 and WWER-1000 reactor bodies.*

EFFECT OF ANNEALING TEMPERATURE ON MECHANICAL PROPERTIES OF MOLYBDENUM ALLOY AND ITS WELDED JOINTS

B.A. ZADERY, S.S. KOTENKO, A.E. MARINCHENKO, E.P. POLISHCHUK and K.A. YUSHCHENKO
E.O. Paton Electric Welding Institute, NASU, Kiev, Ukraine

Effect of annealing temperature on mechanical properties of base and welded joint metal in molybdenum alloy TsM12 has been studied. It is shown that the character of variations in the ductility characteristics of the weld metal with increase in the preliminary annealing temperature is in good agreement with the character of variations in ductility of the initial material. It has been found that the molybdenum alloy specimens cut at different angles to the rolling direction, as well as specimens made from the weld metal and tested in a temperature range of 20–800 °C, exhibit a three-stage mode of strain hardening.

Keywords: *arc welding, molybdenum alloys, welded joints, annealing, cold shortness, strain hardening*

Development of heat-resistant structural materials intended for operation in a temperature range of 1200–1800 °C is based on using refractory metals with the bcc lattice. As follows from study [1], mechanical properties of alloys based on refractory metals, as well as their operational properties (weldability [2–4], formability [5], etc.), depend to a considerable degree upon the structural state of metal resulting from the process of thermomechanical treatment. It should be noted that relationship between structural factors, tough-brittle transition temperature and weldability of refractory bcc metals and alloys on their base play an important role. This relationship is especially important for the alloys welded, as metal of the weld and near-weld zones as a rule greatly differs from the base metal in structural and mechanical characteristics, which leads to decrease in strength and low-temperature ductility of the welded joint as a whole.

Investigations were conducted to study the effect of the structural state on mechanical properties of base metal and metal of welded joints in molybdenum alloy TsM12 of the following chemical composition, wt.%: Mo – base, Hf – 0.14, Zr – 0.12, B – 0.002, Ni – 0.04, C – 0.005, O_2 – 0.001, N_2 – 0.0016, H_2 – 0.0001. The alloy was studied in a deformed condition (as-received) and after annealing for 1 h at a temperature of 1100, 1200, 1400, 1600, 1800 and 2000 °C.

Specimens for welding were cut so that the longitudinal axis of a specimen was at an angle of 0, 45 and 90° to the rolling direction of the initial sheet. Tungsten-electrode arc welding was performed in the chamber with a controlled atmosphere of inert gas under the following conditions: I_w = 120 A, U_a = = 18 V, v_w = 2.8 mm/s.

Mechanical tests of specimens of the base and welded joint metals were conducted using a four-point loading method. The choice of this method was based on the fact that, in contrast to three-point bending, in the case of the four-point one the conditions formed between the load application points, because of a constant bending moment, provide the test results that most accurately characterise the material and do not depend upon the probable heterogeneities of metal (such as structural heterogeneities characteristic of welded joints) in a range of the maximal bending moment.

Cold shortness temperature T_c was determined as the lowest temperature at which the specimens were bent without fracture or cracking. In this case sag f was 2 mm, which corresponds to deformation of external fibres of specimens tested to three-point bending to a bending angle of 90°.

Changes in the proportionality limit depending upon the annealing temperature and test temperature are shown in Figure 1. The molybdenum alloy sheets in the deformed state (after annealing at 1100 °C to relieve treatment stresses) are characterised by a clearly defined anisotropy of the proportionality limit. At room temperature, the specimens cut in a direction coinciding with the rolling direction have a minimum value of σ_p, while the transverse specimens have a maximum value of σ_p. Increasing the test temperature to 400 °C leads to decrease of 200 MPa in the proportionality limit. The anisotropy of properties, however, remains in this case at a previous level. After recrystallisation annealing at a temperature of 1500 °C and formation of an equiaxed grain structure in a sheet with a mean grain size of 60–80 μm, the material exhibits almost complete isotropy at all the test temperatures.

Changes in elongation of the alloy specimens depending upon the annealing and test temperatures are of a totally different character (Figure 1). The uniaxial tension test at room temperature reveals the ductility dip after annealing in a temperature range of 1200–1400 °C. In this case, independently of the orientation of the longitudinal axis of a specimen rela-

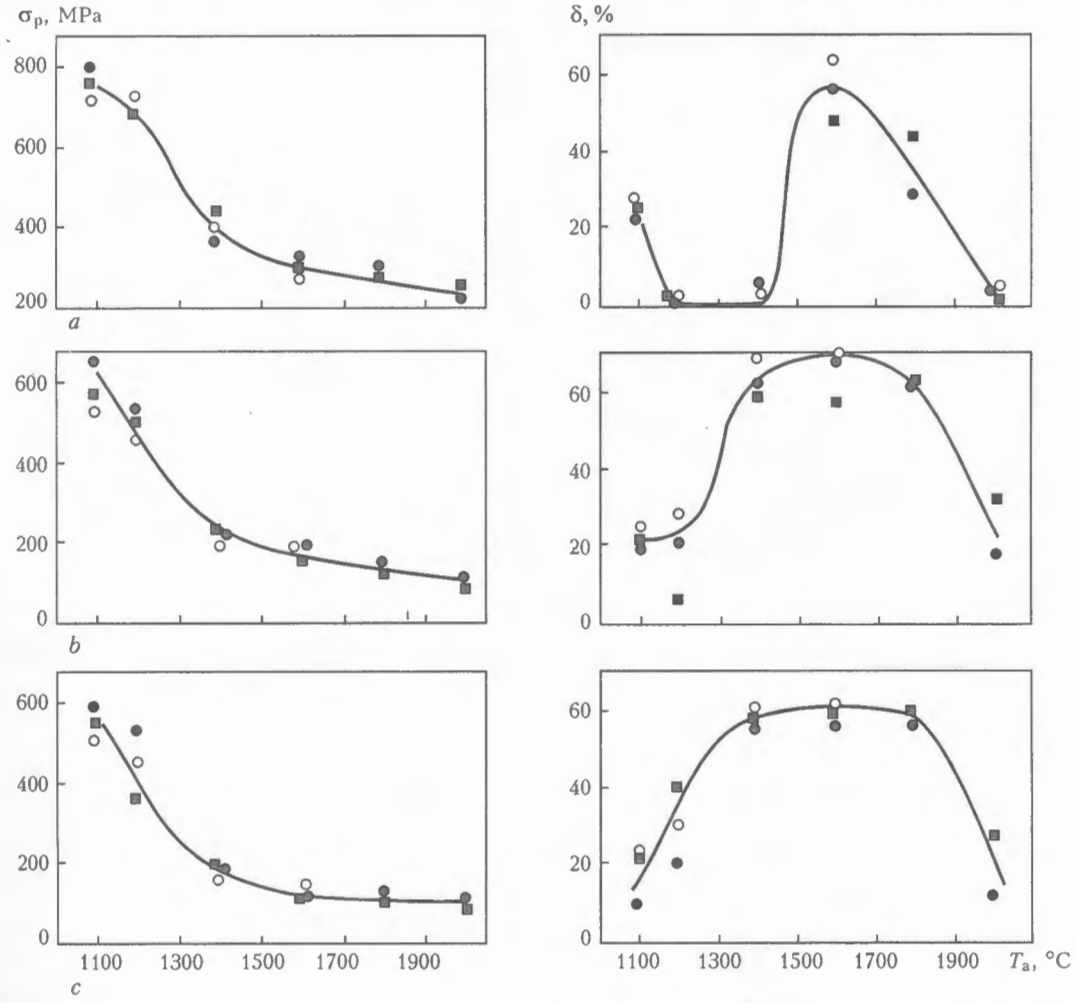

Figure 1. Effect of annealing temperature T_a on proportionality limit σ_p and elongation δ of the specimens cut along (○), across (●) and at an angle of 45° to the rolling direction (■) at different test temperatures T_{test}: *a* — 20; *b* — 200; *c* — 400 °C

tive to the rolling direction of the initial sheet, the values of elongation fall to 0–2.5 %. Increasing the annealing temperature to 1600 °C leads to a dramatic increase in ductility, resulting in anisotropy of properties: elongation of the longitudinal specimens amounts to 62 % and that of the transverse specimens — to 46 %. Increasing the test temperature to 200 and 400 °C leads to elimination of the ductility dip after annealing at temperatures of 1200–1400 °C. Increasing the test temperature is accompanied by decrease in anisotropy of elongation.

Naturally, fusion welding of the molybdenum alloy TsM12 sheets inevitably leads to formation of a region in the heat-affected zone, the structural state of which corresponds to that resulting from annealing of the material at 1200–1400 °C. In this case ductility of a welded joint is at a low level.

Analysis of dependence of variations in structure and mechanical properties upon the deformation conditions shows that formation of certain structural states both during plastic deformation and during subsequent heat treatment, or under controlled conditions of fusion welding, allows a substantial improvement of a set of mechanical characteristics. Plastic deformation of low-alloy molybdenum alloys, ending with formation of sub-boundaries of an extended cellular structure, causes a complete dissolution of precipitates present in the alloy prior to deformation, despite the fact that the latter occurs in a temperature range of decomposition of the oversaturated solid solution in molybdenum. Therefore, no precipitates of the redundant phase, which causes as a rule a substantial decrease in the level of mechanical properties of the alloy, are revealed in structure of the deformed base metal (Figure 2).

Annealing in a temperature range of existence of a relatively stable cellular structure leads to partial annihilation of dislocations inside the cells and escape of the remaining dislocations to the boundaries (Figure 2, *c*, *d*). This is accompanied by a more complete segregation of impurities at the cell boundaries and decrease in the level of residual stresses.

Strain hardening of the molybdenum alloy specimens can be described as follows:

$$\sigma = \sigma_s + \Delta\sigma,$$

where σ_s is the yield stress corresponding to a stress at the moment of beginning of plastic flow of the material. At the first stages of plastic deformation, where the dislocation density increases and the level of disorientation of the formed sub-boundaries is $Q <$

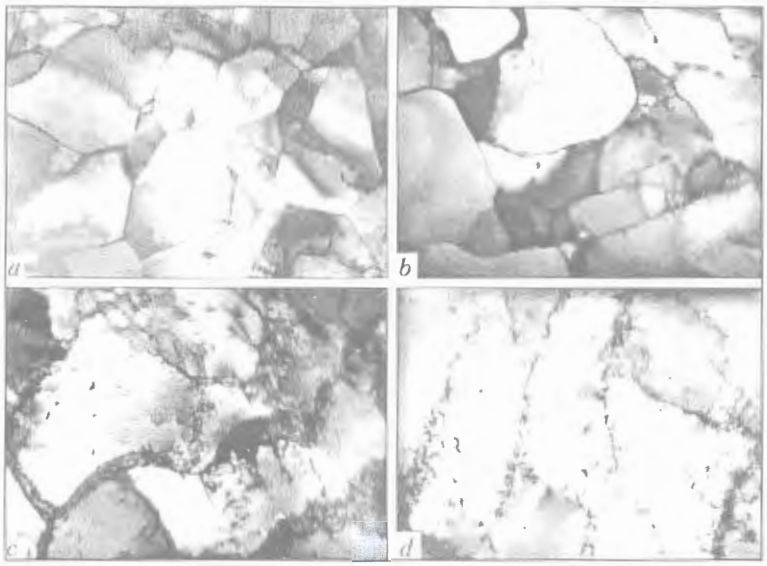

Figure 2. Dislocation structure of molybdenum alloy TsM12 after annealing for 1 h at different temperatures (*a* — 1100; *b* — 1200; *c* — 1300; *d* — 1400 °C) and in testing at 800 °C

$< Q_{cr}$, the value of extra hardening Δ_σ can be determined from the following expression:

$$\Delta\sigma = NE^n,$$

where E is the true plastic strain equal to $\ln(1 + \varepsilon)$; ε is the conditional plastic strain $\Delta l / l_0$; N is the strain hardening coefficient; and n is the strain hardening factor.

Analysis of the results of tests of the TsM12 specimens cut from a sheet at different angles to the rolling direction, after annealing in a temperature range of 1100–2000 °C and tensile test at temperatures of 20–800 °C, indicates to a multistage character of strain hardening (Figure 3). A linear stage of strain hardening is characterised, according to [6, 7], by a concentration of the major part of dislocations in flat clusters located in one or two slip systems. In deformation within this region, the dislocations persist in planes of the active sources, whereas their density grows due to involving the new dislocation sources and, to a lesser degree, systems.

As follows from studies [6, 7], because of a large number of active slip systems and easy transverse slip, this stage of strain hardening in polycrystalline bcc

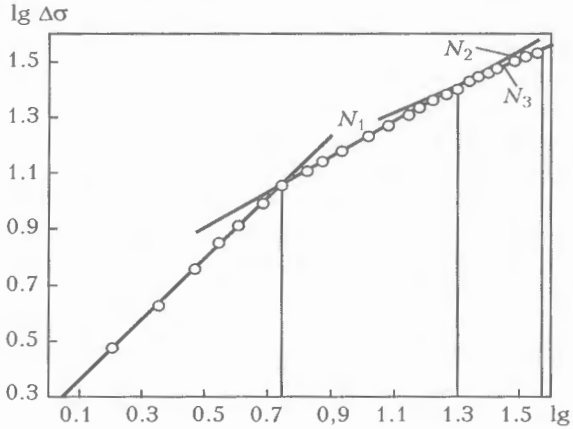

Figure 3. lg $\Delta\sigma$ against lg E (E in %) for longitudinal specimens of alloy TsM12 after annealing at 1400 °C and test temperature of 200 °C

metals shows up only in special cases (at low values of the stacking fault energy and temperature, large grain size, etc.) and is limited to low strains. The presence of an extended zone of the linear stage of strain hardening of the weld metal is attributable to the fact that, according to [2, 3], columnar crystalline grains of the weld metal have approximately identical direction of their boundaries and crystallographic orientation.

Symmetric arrangement of crystalline grains of the weld metal relative to its axis, caused by conditions of solidification of the weld pool from the surface of melted grains at the fusion line, is accompanied by formation of a certain structural and crystallographic texture in the welded joint.

As the Schmidt factor values in this case are approximately identical for the majority of crystals of the weld metal, it can be assumed that, upon reaching the certain level of deformation, the dislocation sources in the same slip systems will work when almost all the crystals have the identical orientation. Therefore, all the crystalline grains make a single-valued contribution to deformation of a specimen and act, thus, as a single whole. This situation is possible, of course, only at the stages of plastic deformation with a low dislocation density.

Occurrence of the linear stage of strain hardening in the weld metal is favoured to a considerable degree by a large size of crystalline grains, ensuring a large length of the free path of dislocations in their slip planes, and allowing the dislocation source to emit more dislocations. The highly developed slip in a limited number of active systems persists in crystals to a certain critical value of deformation.

Upon exceeding this limit, the active slip systems and dislocation sources in them grow in number, and the velocity of these dislocations increases. This leads to increase in the number of collisions of the dislocations and decrease in a mean length of flat slips. As a result, there occurs transition to the next, compara-

tively uniform distribution of the dislocations, i.e. the third stage of strain hardening. At this stage, the strain hardening factor n varies in a non-monotonous manner with increase in the test temperature (Figure 4).

As shown by the test results, the molybdenum alloy considered contained interstitial elements and phases. This led to the effect of dynamic strain ageing showing up in it. Being situated on the crystalline lattice defects, the impurities block the dislocation sources, thus increasing their starting stress. During the deformation process, the impurities limit the ability of the dislocations to move, which leads to rise in the effective stress and, what is important, to increase in the dislocation density growth rate. These effects of the interstitial elements and phases are most pronounced at the initial stages of plastic deformation, where all the sources and dislocations are fixed, and the effect of the dynamic strain ageing, as well as the strain hardening coefficients corresponding to the above stages, grow with elevation of temperature due to increase in mobility of the impurities.

Study of the character of fracture of the molybdenum alloy specimens at room temperature after annealing at different temperatures shows (Figure 5) a mixed inter- and transcrystalline type of fracture at increase in the annealing temperature above the recrystallisation point. Increase in the annealing temperature to 1800 °C has almost no effect on the character of fracture. Pre-recrystallisation annealing at temperatures of 1100 and 1200 °C does not change structure of the initial material, and fracture of the specimens in this structural state occurs, like in a deformed alloy, along the boundaries of sub-structural elements (cells) and is of an exfoliation character.

Increase in the test temperature is accompanied by increase in ductility of the alloy, which correlates with formation of fragments of a pitting fracture of the specimens.

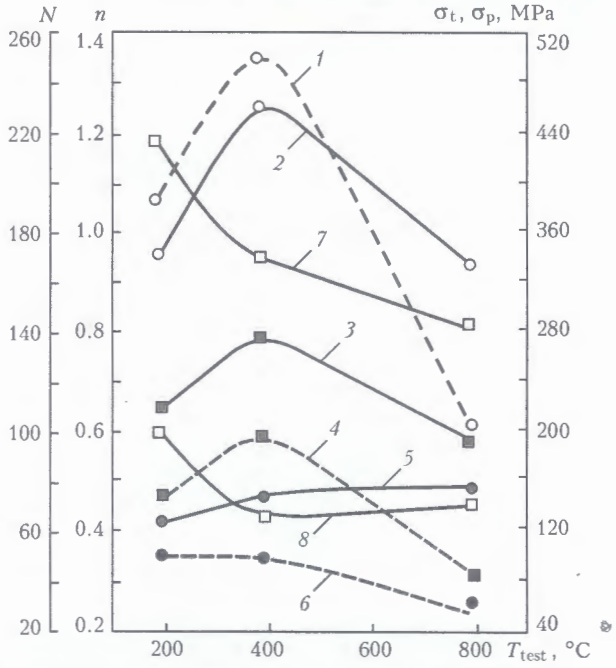

Figure 4. Dependence of strain hardening coefficients N (1 — N_1; 4 — N_2; 6 — N_3), strain hardening factors n (2 — n_1; 3 — n_2; 5 — n_3), proportionality limit σ_p (8) and tensile strength σ_t (7) upon the test temperature of the specimens cut along the rolling direction after annealing for 1 h at 1400 °C

Low-temperature ductility of welded joints in molybdenum alloys is the main factor that allows practical application of molybdenum alloy welded structures [8]. Therefore, in evaluation of performance of welded structures the main consideration should be given to low-temperature ductility and cold shortness temperature of welded joints. The level of low-temperature ductility of the weld metal depends to a certain degree upon the welding process parameters. Its dependence upon the preweld thermomechanical and heat treatment parameters, i.e. upon the initial structure, sub-structure and crystallographic and structural texture, is much stronger [4]. With the identical technology of welding one and the same

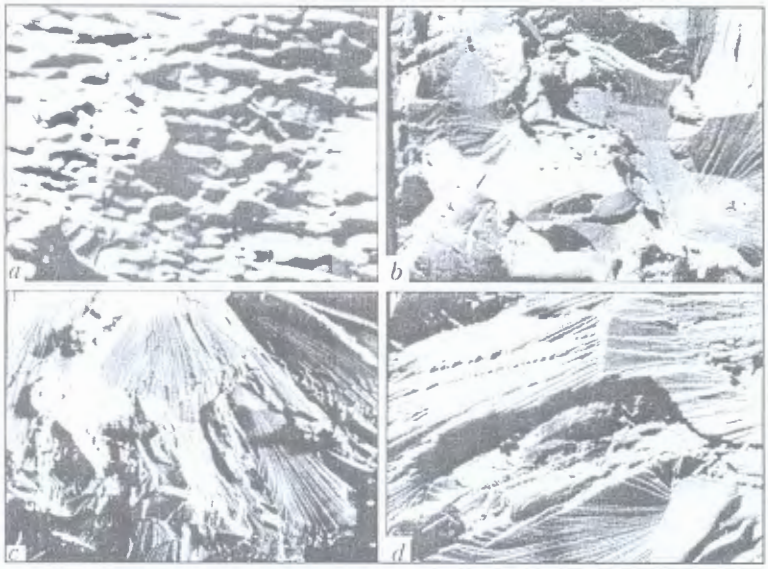

Figure 5. Fracture surface of the specimens cut at an angle of 45° to the rolling direction after annealing for 1 h at different temperatures: a — 1100; b — 1400; c — 1800; d — 2000 °C

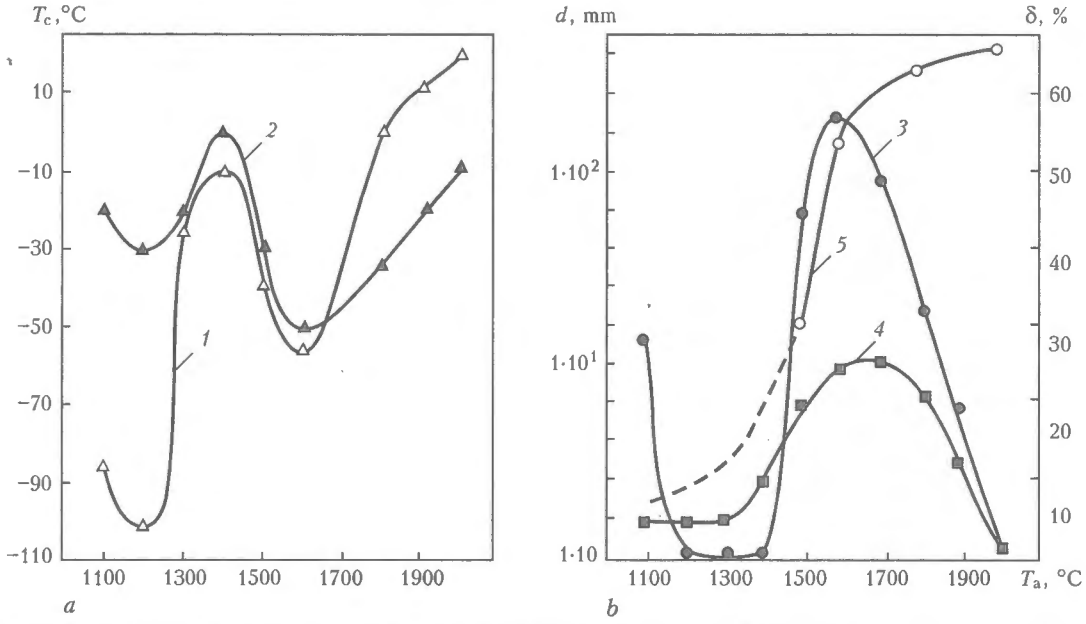

Figure 6. Dependence of cold shortness temperature T_c (*a*), grain size *d* and elongation δ (*b*) upon the annealing temperature: *1*, *2* — cold shortness temperature; *3*, *4* — elongation; *5* — grain size; *1*, *3*, *5* — base metal; *2*, *4* — welded joint

molybdenum alloy, the resulting welded joints may have the angle of bending to fracture ranging from 0 to 180°, depending upon the structural state of the base metal caused by preweld heat treatment.

Figure 6 shows variations in the cold shortness temperature and elongation of the base and weld metals depending upon the temperature of annealing of the initial molybdenum alloy sheet. As follows from the data presented, preliminary annealing of molybdenum alloy TsM12 deformed by rolling is accompanied by a non-monotonous variation in ductility of both base and weld metal.

It should be noted that the character of variations in the cold shortness temperature and elongation remains unchanged. This is another proof of the earlier conclusions [4] that the process of welding thin-sheet molybdenum alloys results in formation of such a structural state of the welded joints which is caused primarily by the structural state of the initial material. It should be emphasised that the cold shortness temperature of a welded joint, independently of the preweld heat treatment parameters, remains in a range of negative temperatures, whereas the cold shortness temperature of the base metal after annealing at temperatures above 1800 °C shifts to a range of positive temperatures. Most probably, this can be caused by a change in the character of fracture.

Specimens cut from the weld metal fracture by the mechanism of transcrystalline cleavage for all parameters of preweld annealing. Specimens of the base metal fracture by the mechanism of exfoliation, where the annealing temperature does not exceed the recrystallisation temperature (Figure 6, *a*). After annealing in a temperature range of 1400–1600 °C the character of fracture is transcrystalline cleavage (Figure 6, *b*). And, finally, after annealing at temperatures above 1800 °C a gradual change in the fracture character from transcrystalline to intercrystalline cleavage occurs.

CONCLUSIONS

1. Annealing of the deformed sheets of molybdenum alloy TsM12 is accompanied by a monotonous decrease in anisotropy of yield stress. After annealing at the recrystallisation temperatures the alloy becomes almost isotropic.

2. Elongation after annealing at temperatures of 1200–1400 °C falls to 0–2.5 %, and then, after annealing at a temperature of 1600 °C, it grows again to 45–65 %, depending upon the orientation of the longitudinal axis of a specimen relative to the rolling direction.

3. Optimal combination of strength and ductile characteristics of a welded joint can be achieved by welding the molybdenum alloy annealed at 1500–1700 °C. In this case, the strain deformation coefficients are equal for different zones of the welded joint, and plastic deformation occurs uniformly and simultaneously over the entire welded joint.

1. Trefilov, V.I., Milman, Yu.V., Firstov, S.A. (1975) *Physical principles of strength of refractory metals*. Kiev: Naukova Dumka.
2. Nerodenko, M.M., Polishchuk, E.P., Vojtkovich, V.G. et al. (1976) Influence of crystallographic and mechanical texture of base metal on properties of welded joints in molybdenum. *Avtomatich. Svarka*, **5**, 19–21, 29.
3. Nerodenko, M.M., Polishchuk, E.P., Milman, Yu.V. et al. (1978) Relationship between crystallographic textures of base metal and weld in low-alloy molybdenum alloys. *Ibid.*, **12**, 12–15.
4. Asnis, E.A., Goncharov, A.B., Nerodenko, M.M. et al. (1995) *Welding of refractory metals*. Ed. by B.E. Paton. Vol. 5. London.
5. Morgunova, N.N., Klypin, B.A., Boyarshinov, V.A. et al. (1975) *Molybdenum alloys*. Moscow: Metallurgiya.
6. Trefilov, V.I., Gornaya, I.D., Moiseev, V.F. et al. (1982) Linear stage in strain hardening of polycrystalline bcc metals. *Doklady AN USSR*. Series A, **11**, 81–85.
7. Gornaya, I.D. (1983) *Principles of strain hardening and fracture of molybdenum-, vanadium- and iron-base alloys*. Syn. of Thesis for Cand. of Phys.-Math. Sci. Degree. Kiev.
8. Trefilov, V.I., Milman, Yu.V., Ivashchenko, R.K. et al. (1983) *Structure, texture and mechanical properties of wrought molybdenum alloys*. Kiev: Naukova Dumka.

EFFECT OF POLARISATION OF RADIATION ON ABSORPTION OF LASER BEAM IN DEEP-PENETRATION WELDING

I.V. KRIVTSUN and **A.N. TALERKO**
E.O. Paton Electric Welding Institute, NASU, Kiev, Ukraine

Mathematical model has been developed to calculate the space distribution of power of laser radiation absorbed by the surface of a keyhole in deep-penetration laser welding. The model allows for the effect of focusing conditions of the initial beam, wavelength and polarisation of laser radiation on its absorption in the keyhole of an arbitrary shape, as well as multiple reflections of incident radiation from the keyhole surface. The model has shown that polarisation of laser radiation, shape and size of the keyhole have a substantial effect on the distributed and integrated characteristics of absorption of the laser beam by metal welded.

Keywords: *laser welding, keyhole, laser beam, radiation polarisation, absorption coefficient, metal, surface*

The impact on metals by such a highly concentrated heat source as the focused laser beam leads to intensive heating, melting and evaporation of metal, causing formation of a keyhole in the metal melt [1]. The coefficient of absorption of electromagnetic waves by a flat surface of the metal melt is very low, and, according to the data of [2], is 5–40 % in the case of a normally falling radiation with a wavelength range characteristic of the majority of technological lasers. Formation of the keyhole leads to a considerable increase in the efficiency of absorption of laser radiation due to its multiple reflections from the keyhole walls. As the laser beam is moved with respect to a sample (which, for example, is the case of welding), the initial beam falls on the front wall of the keyhole at a rather high angle of incidence. Therefore, its absorption may greatly depend upon the direction of a vector of polarisation of the incident radiation [3].

Different models are available for quantitative description of peculiarities of propagation and absorption of laser radiation in the keyhole. However, most of them are limited to a consideration of axisymmetric keyholes [1, 4]. At the same time, in high-speed laser welding, as well as in hybrid laser-arc processes, the keyhole may have an extremely asymmetric shape.

Therefore, this study has been aimed at development of a mathematical model to calculate the integrated and distributed characteristics of absorption of the laser beam by the surface of a keyhole having an arbitrary shape, allowing for multiple reflections of the beam from the keyhole walls (absorption of laser radiation in a vapour flow filling the keyhole being neglected).

Assume that a keyhole, the shape of a free surface of which is set by equation $z = z_s(x, y)$ (Figure 1), is formed in a metal sample under the effect of the focused laser beam. The coordinate system is selected so that axis Oz is directed downward and coincides with the beam axis, while plane $z = 0$ coincides with the upper (flat) surface of the sample. Assume also that the initial laser beam has the form of a quasi-plane electromagnetic wave propagating in a direction of axis Oz, and that it has the Gaussian distribution of the radiation intensity, which is assumed to be linearly polarised, so that vector of the electric field of the incident wave is at angle φ_0 ($0 \le \varphi_0 \le \pi/2$) to the positive direction of axis Ox. The space distribution of a complex amplitude of the electric field for such a beam can be written down as follows [5]:

$$\mathbf{E}_0(x, y, z) = \mathbf{E}_F \frac{w_F}{w_z} \exp\left[-\frac{x^2 + y^2}{w_z^2} + i\left(k\frac{x^2 + y^2}{2R_z} - \varphi_z\right)\right], \quad (1)$$

$$\mathbf{E}_F = E_F (\cos\varphi_0, \sin\varphi_0, 0).$$

Here

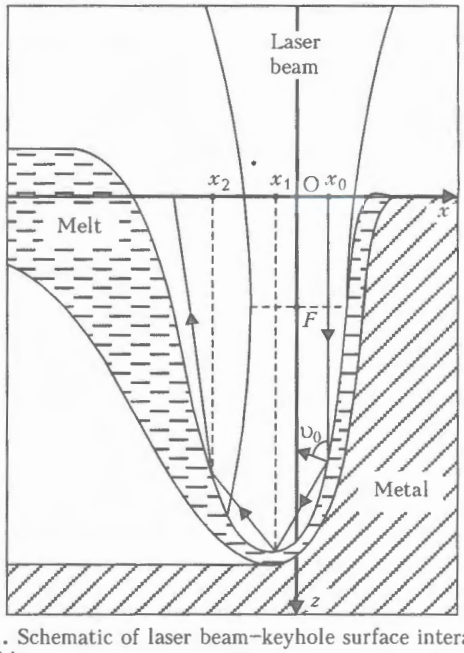

Figure 1. Schematic of laser beam–keyhole surface interaction in laser welding

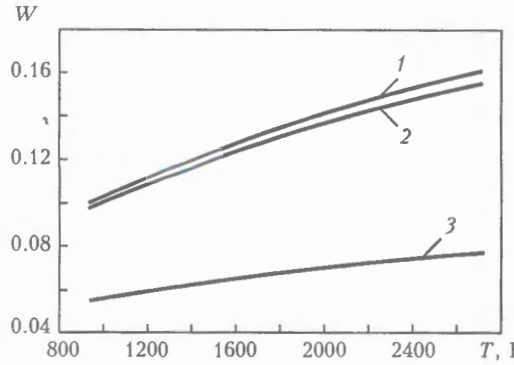

Figure 2. Dependence of the coefficient of absorption of laser radiation falling normal to a flat surface of molten aluminium upon the temperature of this surface (optical properties of molten aluminium were taken from [2]): *1* — diode laser, $\lambda = 0.808$ μm; *2* — YAG-laser, $\lambda = 1.06$ μm; *3* — CO_2-laser, $\lambda = 10.6$ μm

$$w_z^2(z) = w_F^2\left[1 + \frac{(z-F)^2}{z_F^2}\right];\quad R_z(z) = (z-F)\left[1 + \frac{z_F^2}{(z-F)^2}\right];$$

$$\varphi_z(z) = \operatorname{arctg}\left(\frac{z-F}{z_F}\right),\quad z_F = \frac{kw_F^2}{2}, \qquad (2)$$

where w_F is the minimal half-width of the laser beam; F is the distance from the beam focusing plane to the sample surface (see Figure 1); $k = 2\pi/\lambda$ is the wave vector; and λ is the laser radiation wavelength.

Distribution of the radiation intensity in the beam under consideration can be found using the following relationship [3]:

$$I_0(x, y, z) = \frac{c}{8\pi}|\mathbf{E}_0|^2, \qquad (3)$$

where c is the velocity of light.

The value of E_F from (1) is determined using the integral expression for a total power of the beam, Q_0, this yielding

$$E_F^2 = 16Q_0/(cw_F^2). \qquad (4)$$

Absorption of laser radiation by metals in a thin sub-surface layer depends upon the temperature of the metal surface and the radiation wavelength (Figure 2), and in the case of an inclined incidence it depends also upon the radiation polarisation (Figure 3). In a general case, coefficients of absorption of electromagnetic waves by an isotropic metal for two independent polarisations of an incident wave can be determined using the following relationship [6]:

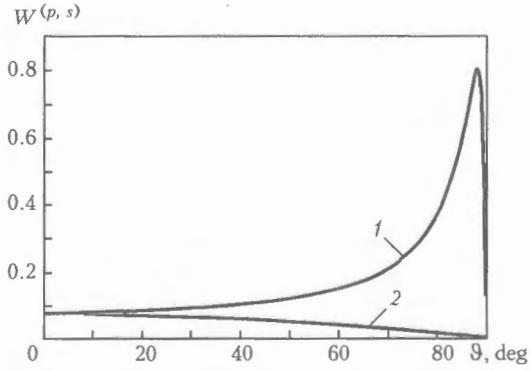

Figure 3. Dependence of the coefficient of absorption of a linearly polarised radiation of the CO_2-laser ($\lambda = 10.6$ μm) by the surface of molten aluminium at a boiling temperature of aluminium ($T = 2720$ K) upon the angle of incidence: *1* — *p*-polarisation; *2* — *s*-polarisation

$$W^{(p,s)} = -\frac{4\mathrm{Re}(Z_\omega^{(p,s)})}{|1 - Z_\omega^{(p,s)}|^2}. \qquad (5)$$

The space dispersion of dielectric permittivity of metal being ignored, the following expressions result for the values of $Z_\omega^{(p,s)}$ [6]:

$$Z_\omega^{(p)} = -\frac{\sqrt{\varepsilon_\omega - \sin^2\vartheta}}{\varepsilon_\omega\cos\vartheta};\quad Z_\omega^{(s)} = -\frac{\cos\vartheta}{\sqrt{\varepsilon_\omega - \sin^2\vartheta}}, \qquad (6)$$

where $\varepsilon_\omega(T)$ is the complex dielectric permittivity at a laser radiation frequency of $\omega = 2\pi c/\lambda$ for metal at temperature T; and ϑ is the incidence angle. Index p corresponds to a case of incidence of a wave, the vector of the electric field of which is parallel to the incidence plane (p-polarisation), and s corresponds to a case where the vector is normal to the incidence plane (s-polarisation).

Use approximation of the geometrical optics to calculate the distributed and integrated characteristics of absorption of the laser beam in a keyhole, allowing for multiple reflections of the radiation from its walls. Assume that the initial laser beam is a set of straight-line rays parallel to axis Oz, each of which is characterised by coordinates (x_0, y_0) of a point of the first incidence onto the metal surface, curvature of the wave front surface of the incident beam near the focusing plane (at $|z - F|^2 << z_F^2$) being ignored. In this case the course of the reflected rays inside the keyhole (see Figure 1) can be determined using the following equations:

$$\frac{x - x_m}{a_{m+1}} = \frac{y - y_m}{b_{m+1}} = \frac{z - z_m}{c_{m+1}},\quad m = 0, 1, 2, \ldots, \qquad (7)$$

where $\{x_m(x_0, y_0), y_m(x_0, y_0)$ and $z_m(x_0, y_0)\}$ are the space coordinates of a point of the $m + 1$ incidence of a corresponding ray onto the keyhole surface, $a_{m+1}(x_0, y_0)$, $b_{m+1}(x_0, y_0)$ and $c_{m+1}(x_0, y_0)$ are the direction cosines of a unit vector ($a_{m+1}^2 + b_{m+1}^2 + c_{m+1}^2 = 1$) in a direction of the reflected ray after the $m + 1$ reflection.

Coordinates of the reflection points are found from the conditions of intersection of the reflected rays with the keyhole surface (providing that a given ray after the preceding reflection does not propagate outside the keyhole):

$$\frac{x_{m+1} - x_m}{a_{m+1}} = \frac{y_{m+1} - y_m}{b_{m+1}} = \qquad (8)$$

$$= \frac{z_s(x_{m+1}, y_{m+1}) - z_m}{c_{m+1}},\quad m = 0, 1, 2, \ldots$$

The direction cosines are determined proceeding from the conditions that incidence angle $\vartheta_m(x_0, y_0)$ is equal to the reflection angle, and that the incident and reflected rays are in the same plane with the vector of normal to surface $z = z_s(x, y)$ at the point of incidence:

$$\begin{aligned} \cos\vartheta_m &= a_{m+1}\alpha_m + b_{m+1}\beta_m + c_{m+1}\gamma_m = \\ &= -(a_m\alpha_m + b_m\beta_m + c_m\gamma_m); \\ a_{m+1}(b_m\gamma_m - c_m\beta_m) &+ b_{m+1}(c_m\alpha_m - a_m\gamma_m) + \\ + c_{m+1}(a_m\beta_m - b_m\alpha_m) &= 0, \quad m = 0, 1, 2, \ldots , \end{aligned} \tag{9}$$

where $\alpha_m(x_0, y_0)$, $\beta_m(x_0, y_0)$ and $\gamma_m(x_0, y_0)$ are the direction cosines of a unit vector of the internal normal to the keyhole surface at a point of the $m + 1$ incidence of a corresponding ray:

$$\alpha_m = \frac{p_m}{\sqrt{1 + p_m^2 + q_m^2}}; \quad \beta_m = \frac{q_m}{\sqrt{1 + p_m^2 + q_m^2}}; \quad \gamma_m = -\frac{1}{\sqrt{1 + p_m^2 + q_m^2}}; \tag{10}$$

$$p_m = \frac{\partial z_s}{\partial x}\Big|_{\substack{x = x_m \\ y = y_m}}; \quad q_m = \frac{\partial z_s}{\partial y}\Big|_{\substack{x = x_m \\ y = y_m}}.$$

Direction cosines for rays of the initial laser beam are

$$a_0 = b_0 = 0, \; c_0 = 1. \tag{11}$$

Equation for the plane of incidence of a ray onto the keyhole surface can be written down as follows:

$$A_m x + B_m y + C_m z + D_m = 0, \quad m = 0, 1, 2, \ldots , \tag{12}$$

where $A_m(x_0, y_0)$, $B_m(x_0, y_0)$ and $C_m(x_0, y_0)$ are the direction cosines of a unit vector of normal to a plane of the $m + 1$ incidence of the initial ray with coordinates (x_0, y_0).

The corresponding direction cosines can be determined from the conditions that this plane passes through the point of incidence, and that the incident ray and vector of normal to the keyhole surface at this point are parallel to the plane of incidence:

$$\begin{aligned} A_m x_m + B_m y_m + C_m z_m + D_m &= 0; \\ A_m a_m + B_m b_m + C_m c_m &= 0; \\ A_m\alpha_m + B_m\beta_m + C_m\gamma_m &= 0, \quad m = 0, 1, 2, \ldots , \end{aligned} \tag{13}$$

as well as from the condition that $A_m^2 + B_m^2 + C_m^2 = 1$. For the planes of incidence of the initial laser beam rays

$$A_0 = \frac{\beta_0}{\sqrt{\alpha_0^2 + \beta_0^2}}; \quad B_0 = -\frac{\alpha_0}{\sqrt{\alpha_0^2 + \beta_0^2}}; \quad C_0 = 0. \tag{14}$$

At the first incidence of a ray of the initial beam onto the keyhole surface at point $\{x_0, y_0, z_s(x_0, y_0)\}$, power of the radiation falling on the elementary region of this surface $dS_0(x_0, y_0) = -dS_0^{(x, y)}/\gamma_0(x_0, y_0)$, has the following form:

$$dP_0 = I_0\,[x_0, y_0, z_s(x_0, y_0)]\; dS_0^{(x, y)}, \tag{15}$$

where $dS_0^{(x, y)} \equiv dx_0 dy_0$ is the projection of dS_0 on plane xOy.

Expressions (1) and (3) being taken into account, the corresponding portion of this power for each of the two independent polarisations of the radiation can be found as follows:

$$dP_0^{(p)} = dP_0 \cos^2\psi_0; \quad dP_0^{(s)} = dP_0 \sin^2\psi_0, \tag{16}$$

where $\psi_0(x_0, y_0)$ is the angle between the plane of the first incidence of a selected ray and direction of the vector of the electric field of the initial laser beam.

The total radiation power absorbed by region dS_0 can be written down as follows:

$$d\bar{P}_0 = dP_0(W_0^{(p)} \cos^2\psi_0 + W_0^{(s)} \sin^2\psi_0). \tag{17}$$

The heat flow introduced into metal by the initial laser beam at point $\{x_0, y_0, z_s(x_0, y_0)\}$ can be calculated as follows:

$$q_0 = dP_0(W_0^{(p)} \cos^2\psi_0 + W_0^{(s)} \sin^2\psi_0)/(dS_0), \tag{18}$$

where $W_0^{(p, s)}[\vartheta_0(x_0, y_0), T(x_0, y_0)]$ are the values of the absorption coefficients for p- and s-polarisation, respectively, at the said point of the surface.

Power of the radiation falling then on region dS_1, reflected from the elementary region dS_0, is

$$\begin{aligned} dP_1 \equiv d\bar{P}_0 = \\ = dP_0[(1 - W_0^{(p)}) \cos^2\psi_0 + (1 - W_0^{(s)}) \sin^2\psi_0)]. \end{aligned} \tag{19}$$

By repeating the above considerations for subsequent reflections, we can derive the recurrent formula to find $dP_{m+1}[x_{m+1}(x_0, y_0)$ and $y_{m+1}(x_0, y_0)]$:

$$\begin{aligned} dP_{m+1} = dP_m[(1 - W_m^{(p)}) \cos^2\psi_m + \\ + (1 - W_m^{(s)}) \sin^2\psi_m], \quad m = 0, 1, 2, \ldots , \end{aligned} \tag{20}$$

where $W_m^{(p, s)}[\vartheta_m(x_0, y_0), T(x_m, y_m)]$ and $\psi_m(x_0, y_0)$ are the values of the absorption coefficients and angle between the plane of the $m + 1$ incidence of a ray onto the keyhole surface and direction of the vector of the incident radiation electric field.

The value of $dP_0(x_0, y_0)$ is found from formula (15), and the angle can be calculated from the following relationship:

$$\begin{aligned} \sin^2\psi_m = \\ = \frac{[A_m(E_m^{(p)} + E_m^{(s)})_x + B_m(E_m^{(p)} + E_m^{(s)})_y + C_m(E_m^{(p)} + E_m^{(s)})_z]^2}{(E_m^{(p)} + E_m^{(s)})_x^2 + (E_m^{(p)} + E_m^{(s)})_y^2 + (E_m^{(p)} + E_m^{(s)})_z^2}, \\ m = 0, 1, 2, \ldots , \end{aligned} \tag{21}$$

where electric field components $\mathbf{E}_m = \mathbf{E}_m^{(p)} + \mathbf{E}_m^{(s)}$ at the $m + 1$ incidence of a ray onto the keyhole surface are determined from the conditions that the vector of $\mathbf{E}_m^{(p)}$ lies in the plane of incidence and is normal to the incident ray, and that $\mathbf{E}_m^{(s)}$ is normal to this plane:

$$(E_m^{(p)})_x a_m + (E_m^{(p)})_y b_m + (E_m^{(p)})_z c_m = 0;$$
$$(E_m^{(p)})_x A_m + (E_m^{(p)})_y B_m + (E_m^{(p)})_z C_m = 0;$$
$$\frac{A_m}{(E_m^{(s)})_x} = \frac{B_m}{(E_m^{(s)})_y} = \frac{C_m}{(E_m^{(s)})_z}, \quad m = 0, 1, 2, \ldots, \tag{22}$$

and from the conditions that relate the electric field components for the incident and reflected radiation at a corresponding incidence:

$$(E_{m+1}^{(p)})^2 = (1 - W_m^{(p)})(E_m^{(p)})^2;$$
$$(E_{m+1}^{(s)})^2 = (1 - W_m^{(s)})(E_m^{(s)})^2, \quad m = 0, 1, 2, \ldots \tag{23}$$

In particular, for the first incidence using (1) and (2) we find that

$$\sin^2 \psi_0 = (A_0 \cos \varphi_0 + B_0 \sin \varphi_0)^2. \tag{24}$$

By analogy with (18), heat flow $q_m[x_m(x_0, y_0), y_m(x_0, y_0), z_m(x_0, y_0)]$ introduced into metal at the $m + 1$ incidence of the ray (x_0, y_0) of the initial beam onto the keyhole surface can be written down as follows:

$$q_m = dP_m(W_m^{(p)} \cos^2 \psi_m + W_m^{(s)} \sin^2 \psi_m)/(dS_m), \quad m = 0, 1, 2, \ldots \tag{25}$$

Here $dS_m(x_0, y_0) = -dS_m^{(x, y)}/\gamma_m(x_0, y_0)$, where $dS_m^{(x, y)}$ is the surface area of a quadrangle in plane xOy, the corners of which are determined by coordinates (x_m, y_m) of the points of intersection of the initial beam rays (x_0, y_0), $(x_0 + dx_0, y_0)$, $(x_0, y_0 + dy_0)$ and $(x_0 + dx_0, y_0 + dy_0)$ with surface $z = z_s(x, y)$ at the $m + 1$ reflection.

The resultant space distribution of the heat flow introduced into metal by the laser beam, allowing for multiple reflections of radiation from the keyhole walls, can be written down in the following form:

$$q[x, y, z_s(x, y)] = \sum_{m=0}^{\infty} \int \delta[x - x_m(x_0, y_0)]\delta[y - y_m(x_0, y_0)] q_m dx_0 dy_0. \tag{26}$$

Integration is done over a range of variations in the coordinates of the initial laser beam rays falling on the keyhole surface. Then, by integrating over the entire surface of $z = z_s(x, y)$ from expression (26), we can calculate total power $\overline{Q}$ absorbed by metal, as well as the integral absorption coefficient determined as

$$\overline{W} = \overline{Q}/Q_0. \tag{27}$$

The algorithm was developed for numerical realisation of the suggested model. This algorithm is based on the principle of discretisation of the calculation domain by plotting a 2D grid in plane xOy and a corresponding array containing values of the z-coordinates of the keyhole surface points. The total value (for all possible reflections) of the absorbed radiation power was determined for each cell of this grid. A limiting condition for the quantity of the reflections considered was that allowance for the next reflection should not lead to a change of more than 1 % in the absorbed power. Then the value of the heat flow corresponding to a given cell was calculated.

The software was developed to enable computer modelling of the distributed and integrated characteristics of absorption of the laser beam in deep-penetration welding. The input parameters for the computation software included physical and geometric characteristics of the initial laser beam (power, wavelength and direction of the vector of polarisation of the radiation, beam diameter in the focusing plane and position of this plane with respect to the sample surface), as well as optical properties of metal, shape and geometric sizes of the keyhole.

It should be noted that this software can be utilised to compute characteristics of absorption of the laser beam with an arbitrary (non-Gaussian) distribution of the radiation intensity. The software was used to conduct numerical analysis of peculiarities of absorption of the Gaussian beam of the CO_2-laser radiation (λ = 10.6 μm) in keyholes of different shapes, as applied to laser welding of aluminium. Depth H of the keyhole was varied from 2 to 10 mm, and temperature of its surface was assumed to be uniform and equal to the boiling temperature of aluminium. Parameters of the initial laser beam were selected as follows: power — Q_0 = 10 kW, sample surface to focusing plane distance — F = 5 mm, range of variation of the beam diameter in this plane, d_F, determined as the diameter of a circle within which 99 % of the laser radiation power ($2w_F = 0.66d_F$) is concentrated — 0.2–0.5 mm, and angle between the radiation polarisation vector and welding direction — $\varphi_0 = 0$–$\pi/2$. The used values of the absorption coefficients for p- and s-polarised radiation were selected in accordance with the data shown in Figure 3.

Figures 4–7 show the results of calculation of the distributed and integrated characteristics of absorption of the laser beam in the keyhole, the shape of which in the selected coordinate system is set by the following equations:

$$1 - \frac{z}{H} = \begin{cases} \dfrac{(x + \Delta x)^2}{(R_x^+)^2} + \dfrac{y^2}{R_y^2}, & x + \Delta x > 0; \\ \dfrac{(x + \Delta x)^2}{(R_x^-)^2} + \dfrac{y^2}{R_y^2}, & x + \Delta x < 0, \end{cases} \tag{28}$$

at $R_x^+ = 0.5$ mm, $R_x^- = 1.5$ mm, $R_y = 1.0$ mm and Δx = = 0.25 mm.

The effect of polarisation of laser radiation on the space distribution of the heat flow introduced into metal through the surface of such a keyhole is illustrated in Figures 4 and 5. An intensive absorption of the initial laser beam falling on the front wall of the keyhole at high values of angle ϑ_0 (for an axial beam, e.g., $\vartheta_0 \approx 87°$) is seen at $\varphi_0 = 0$, whereas the radiation polarised so that $\varphi_0 = \pi/2$ is absorbed very insignificantly at the first incidence onto the keyhole surface

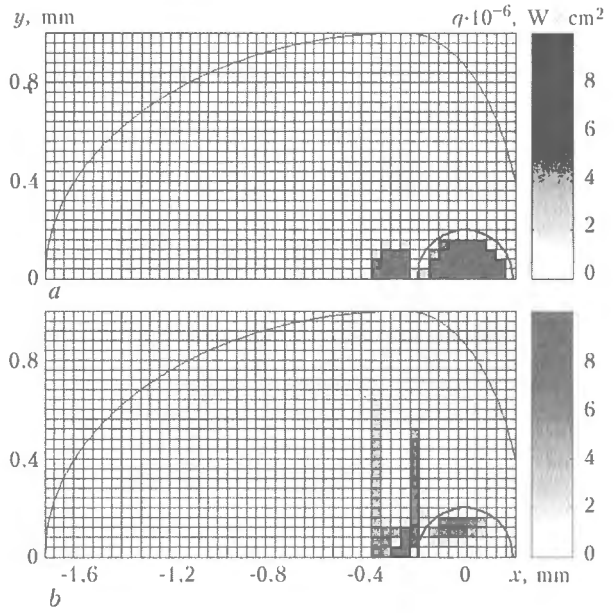

Figure 4. Space distribution of the heat flow introduced into metal through the keyhole surface (H = 10 mm) by the laser beam with d_F = 0.4 mm, linear polarisation of the radiation and different welding directions: *a* — $\varphi_0 = 0$; *b* — $\varphi_0 = \pi/2$

(Figure 5). This is associated with a substantial difference in the absorption coefficients for *p*- and *s*-polarised waves at high values of the angle of incidence (see Figure 3). The laser radiation reflected after the first incidence onto the metal surface falls on the rear wall of the keyhole. In this case several additional absorption maxima (solid curve in Figure 5) rapidly decreasing in amplitude, which correspond to subsequent reflections and are concentrated near plane *xOz* (see Figure 4, *a*), are formed at $\varphi_0 = 0$, whereas at $\varphi_0 = \pi/2$ only one additional absorption maximum corresponding to the second incidence (dashed curve in Figure 5) is formed near the said plane. It should be noted that in the last case a considerable portion of the absorbed energy (both at the first reflection and at the reflections that follow) falls on the side walls of the keyhole (see Figure 4, *b*), where the radiation component with a vector of the electric field lying in the incidence plane contributes much to the total absorption.

The data shown in Figure 6 are indicative of a substantial increase in the radiation power absorbed

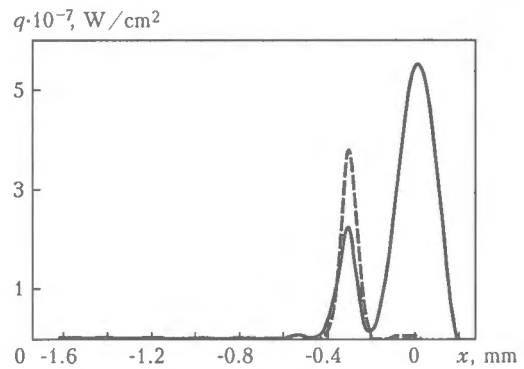

Figure 5. Distribution of the heat flow in the keyhole symmetry plane (y = 0) at $\varphi_0 = 0$ (*solid curve*) and $\varphi_0 = \pi/2$ (*dashed curve*); the rest of the parameters are the same as in Figure 4

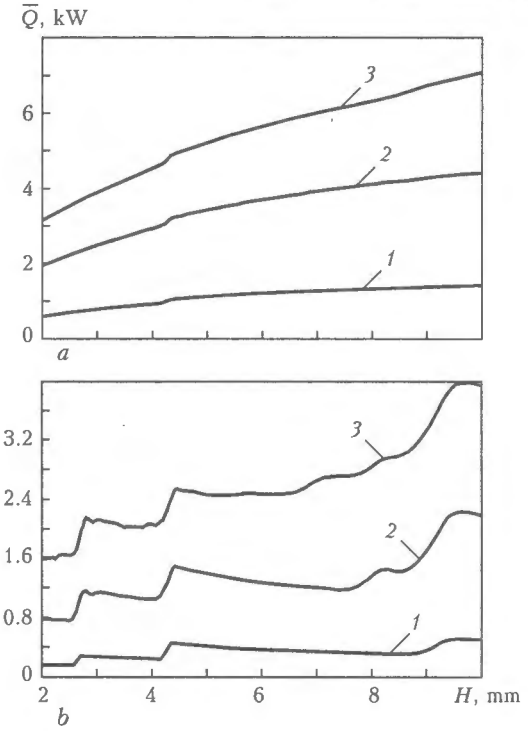

Figure 6. Dependence of the radiation power absorbed by metal upon the depth of the keyhole for the laser beam with $\varphi_0 = 0$ (*a*) and $\varphi_0 = \pi/2$ (*b*) at different values of the beam diameter in the focusing plane: *1* — d_F = 0.2; *2* — d_F = 0.3; *3* — d_F = 0.5 mm

by the surface of the keyhole of a shape considered with increase in diameter d_F of the initial laser beam. In addition, a stepwise increase in the radiation power absorbed in the keyhole takes place with increase in its depth, which can be related to the corresponding increase in the quantity of possible reflections of the initial beam rays (before they leave the keyhole). This effect is especially pronounced in the case of a laser radiation polarised normal to the welding direction (see Figures 6, *b* and 7), since, as shown above, the radiation beam with $\varphi_0 = \pi/2$ is very slightly absorbed at the first incidence onto the keyhole surface. As far as the absolute values of $\overline{Q}$ are concerned, at $\varphi_0 = 0$ the radiation power absorbed by metal is almost twice as high as that observed at $\varphi_0 = \pi/2$ (see Figure 6, *a* and *b*), the major change taking place in a range of $\pi/6 \le \varphi_0 = \pi/2$ (see Figure 7).

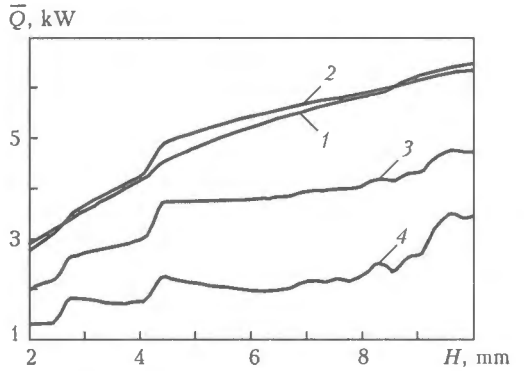

Figure 7. Dependence of the absorbed power upon the depth of the keyhole at d_F = 0.4 mm and different directions of the radiation polarisation vector in the initial beam: *1* — $\varphi_0 = 0$; *2* — $\varphi_0 = \pi/6$; *3* — $\varphi_0 = \pi/3$; *4* — $\varphi_0 = \pi/2$

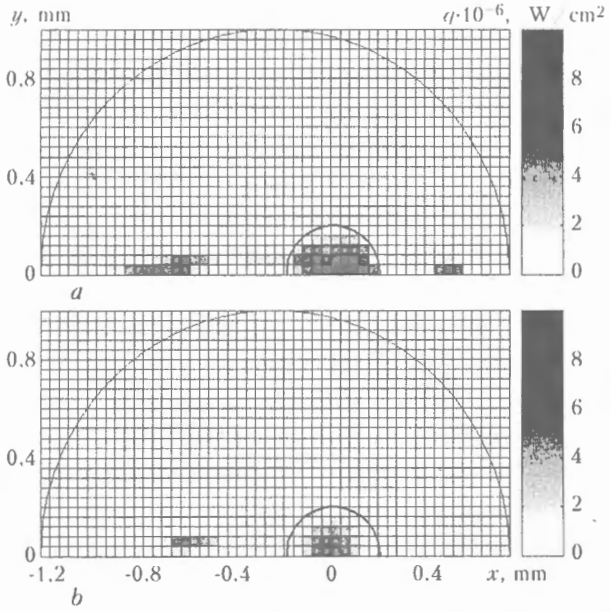

Figure 8. Space distribution of the heat flow introduced into metal by the laser beam with $d_F = 0.4$ mm and linear radiation polarisation: *a*, *b* — same as in Figure 4

Figures 8 and 9 show the calculation data on distribution of the heat flow for the case of absorption of the laser beam in the keyhole of a different shape:

$$1 - \frac{z}{H} = \left[\frac{(x + \Delta x)^2 + y^2}{R^2}\right]^2, \qquad (29)$$

where $H = 10$ mm, $R = 1$ mm and $\Delta_x = 0.25$ mm.

In this case the initial beam rays also undergo multiple reflections in the keyhole. However, unlike the earlier considered shape of the keyhole, here the reflected rays can contribute much to that portion of the radiation power that is absorbed by its front wall (compare Figures 5 and 9). The distribution of $q[x, 0, z_s(x, 0)]$ in a case of using laser radiation polarised in the welding direction is similar to that for the radiation polarised in a normal direction, the difference being that the heat flow and total absorbed power are much higher in the first case.

It can be noted in conclusion that the direction of the radiation polarisation vector in the laser beam exerts a substantial effect on its absorption by metal during deep-penetration laser welding. In particular, the laser radiation polarised along the weld is absorbed almost twice as efficient as that polarised in the normal direction. Therefore, to increase the efficiency of laser welding, it is expedient to use laser beams with a linear polarisation of radiation along the welding direction.

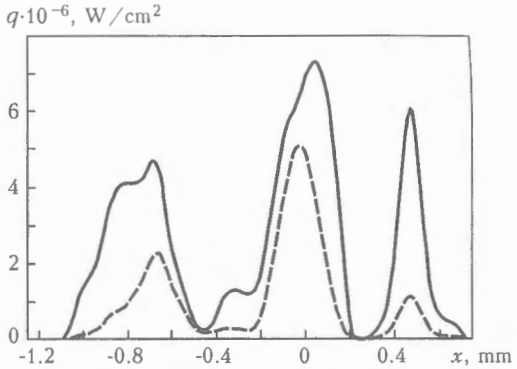

Figure 9. Distribution of the heat flow in plane $y = 0$ at $\varphi_0 = 0$ (*solid curve*) and $\varphi_0 = \pi/2$ (*dashed curve*); $d_F = 0.4$ mm

The space distribution of the heat flow introduced by the laser beam through the keyhole surface greatly depends upon the radiation polarisation, and can be substantially different from the distribution of the radiation intensity in the initial beam. This should be taken into account in analysis of the processes occurring on the surface and in the bulk of the weld pool, as well as in calculation of the space-time distributions of metal temperature in the HAZ during deep-penetration laser welding.

As the shape and geometric size of the keyhole have a strong effect on the distributed and integrated characteristics of absorption of the laser beam, to adequately describe the deep-penetration laser welding process it is necessary to develop a mathematical model, which would allow the shape and size of the keyhole to be determined in a self-consistent way, depending upon the welding process parameters, including the laser radiation polarisation.

1. Arutyunyan, R.V., Baranov, V.Yu., Bolshov, L.A. et al. (1989) *Effect of laser radiation on materials*. Moscow: Nauka.
2. Miller, J.C. (1969) Optical properties of liquid metals at high temperatures. *Phil. Mag.*, **20**, 1115–1132.
3. Landau, L.D., Lifshits, E.M. (1982) Electrodynamics of continuous media. Moscow: Nauka.
4. Lopota, L.D., Sukhov, Yu.T., Turichin, G.A. (1997) Model of laser welding with deep penetration for technology application. *Izvestiya RAN. Physics Series*, 61(8), 1613–1618.
5. Yariv, A. (1980) *Quantum electronics*. Moscow: Sov. Radio.
6. Gvozdetsky, V.S., Zagorodny, A.G., Krivtsun, I.V. et al. (1987) Effect of layered dielectric coatings on absorption properties of constricted plasma-like media. *Radiotekhnika i Elektronika*, 32(11), 2372–2381.

DETERMINATION OF DESIGN S–N CURVES OF WELDED JOINTS OF METAL STRUCTURES CURRENTLY IN SERVICE

P.P. MIKHEEV, V.V. KNYSH, O.V. VOJTENKO and **V.A. BRODOVOJ**
E.O. Paton Electric Welding Institute, NASU, Kiev, Ukraine

A procedure was developed of plotting design S–N curves for the main types of welded joints for in-service structures, using a specially developed software for PC. Obtained design S–N curves of welded joints were compared with the results of fatigue testing of large-scale specimens.

Keywords: *welded joint, bounded fatigue limit, stress concentration factor, S–N curve, software, residual life*

In order to determine the residual life of welded structures, the design life of which is over, it is necessary to have the characteristics of fatigue strength of welded joints (design S–N curves), corresponding to the fatigue strength of the actual (examined) joints of structures in operation. Such curves cannot be generated experimentally, as preparing the respective specimens will require violating the integrity of the load-carrying elements of the structure.

It is suggested taking the basic diagrams of limit stresses of welded joints in steel of various strength grades with low (close to zero) residual stresses as the initial data for establishing the design S–N curves of welded joints. Basic diagrams of welded joints are specified by RD 50-694–90 «Procedural guidelines. Probabilistic method of fatigue analysis of welded structures» [1]. As in RD document stress concentration factors α_σ are not specified for the established groups of welded joints, it is proposed to take their average values, earlier determined for the respective types of welded joints, as the standard α_σ values [2, 3]. Average values of the stress concentration factors for element groups 2–7, according to the classification in RD 50-694–90, are given below:

Element group	2	3	4	5	6	7
Stress concentration factor α_σ	1.1	1.3	1.4	1.6	1.7	2.3

Two values of endurance limit σ_{R_σ} (for instance, at $N = 5 \cdot 10^4$ and $N = 2 \cdot 10^6$ cycles) at a specified cycle asymmetry R_σ, required for plotting the basic S–N curve, can be determined directly from the diagrams of limit cycle stresses of the respective groups of welded joints in steels of three strength grades.

For subsequent automation of the procedures of plotting the basic S–N curves, it is recommended to determine the required values of endurance limit σ_{R_σ} from the following relationship:

$$\sigma_{R_\sigma} = \frac{2\sigma_{-1}}{2 - D(1 + R_\sigma)}, \qquad (1)$$

where $D = \sigma_0 - \sigma_{-1}/\sigma_m$; σ_{-1} is the endurance limit of the joint at a symmetrical loading cycle determined from the diagrams of limit cycle stresses for a specified number of cycles; σ_m is the average limit cycle stress determined from the diagrams of limit cycle stresses for a specified number of cycles at $R_\sigma = 0$; R_σ is the coefficient of cycle asymmetry; σ_0 is the endurance limit of the joint at zero-to-compression stress cycle determined from the diagram of limit cycle stresses for a specified cycle number.

It is proposed to plot the basic S–N curves for this group of welded joints in $(N - \sigma)$ co-ordinate plane in the form of a straight line ($\sigma = a \lg N + b$), passing through points with co-ordinates ($5 \cdot 10^4$, $\sigma_{R_\sigma}^{2 \cdot 10^4}$) and ($2 \cdot 10^6$, $\sigma_{R_\sigma}^{2 \cdot 10^6}$). In this case the equation of the basic S–N curve becomes

$$\sigma = 0.625\sigma_{R_\sigma}^{5 \cdot 10^4}\left(\frac{\sigma_{R_\sigma}^{2 \cdot 10^6}}{\sigma_{R_\sigma}^{5 \cdot 10^4}} - 1\right)\lg N + 3.94\sigma_{R_\sigma}^{5 \cdot 10^4}\left(1 - 0.75\,\frac{\sigma_{R_\sigma}^{2 \cdot 10^6}}{\sigma_{R_\sigma}^{5 \cdot 10^4}}\right). \qquad (2)$$

For presentation of this procedure the type of joints with fillet welds, corresponding to class 4b of the code [1] (Figure 1) and made of low-carbon steel (σ_y = 240 MPa, σ_t = 480 MPa), for a symmetrical loading cycle ($R_\sigma = -1.0$) was selected from seven groups of welded joints of metal structures.

The corresponding basic S–N curve, plotted from relationship (2), is given in Figure 2.

Plotting of design S–N curves of welded joints in load-carrying elements of metal structures in operation, required to determine their residual life, is performed on the basis of a procedure developed at PWI. This is a procedure of design determination of a bounded endurance limit, corresponding to $2 \cdot 10^6$ cycles, allowing for the actual values determined in the structure in service for the stress concentration factors, asymmetry of the loading cycle, steady-state level of residual stresses and mechanical properties of the metal [3, 4].

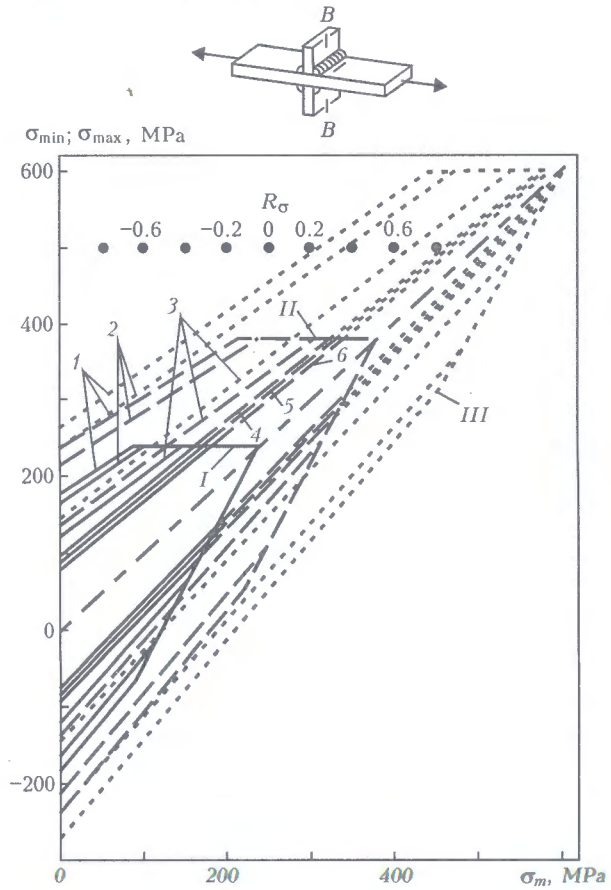

Figure 1. Diagrams of limit stresses of the cycle for group 4b elements: *I* — low-carbon; *II* — low-alloyed; *III* — high-strength steels; *1* — $N = 5 \cdot 10^4$; *2* — $1 \cdot 10^5$; *3* — $5 \cdot 10^5$; *4* — $2 \cdot 10^6$; *5* — $5 \cdot 10^6$; *6* — $N \rightarrow \infty$ cycles

A basic S–N curve is selected, which is determined by the above method, and which pertains to the type of welded joint with a low level of residual welding stresses, for which the averaged stress concentration factor α_σ is the closest to the experimentally established stress concentration factor α_σ^k of a welded joint of the metal structure element in service. To provide a conservative estimate of the residual life of a welded structure, the basic S–N curve should correspond to the averaged stress concentration factor α_σ, greater than or equal to the experimentally established α_σ^k. In this case the basic S–N curve is determined for the value of the coefficient of asymmetry of an alternating

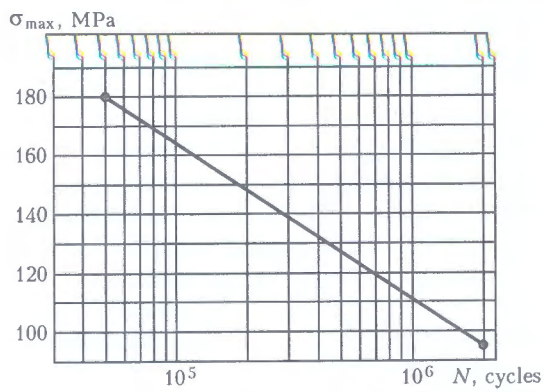

Figure 2. Basic S–N curve of a welded joint of class 4b on low-carbon steel; $R_\sigma = -1.0$

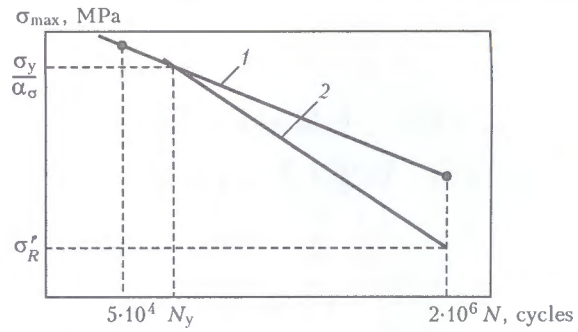

Figure 3. Schematic of plotting a design S–N curve of a welded joint on an element of a metal structure in service: *1* — basic S–N curve ($\sigma_{res} = 0$); *2* — design curve

loading cycle, corresponding to its value in service for the studied element of a welded structure. The established position of the basic S–N curve is used to determine the cyclic fatigue life N_y, corresponding to the region of cyclic loading, in which in the zones of a stress raiser with concentration factor α_σ the stresses reach the values of base metal yield point.

In other words, the known equation of basic S–N curve (2) is used to determine the number of cycles of stress alternation N_y, corresponding to the value of maximum cycle stress σ_{max}, equal to σ_y/α_σ value. The thus obtained point with co-ordinates (N_y, σ_y/α_σ) in co-ordinate plane ($N - \sigma$) is taken to be the upper point of the design S–N curve of welded joints in load-carrying elements of metal structures in service with their inherent combinations of factors, which determine their fatigue resistance (Figure 3).

Such factors are known to be mechanical properties of base metal, stress concentration factor α_σ^k, coefficient of cycle asymmetry R_σ, and maximum stresses σ_{max} of the cycle of external alternating loading σ^{st} and steady-state level of residual welding stresses σ_{res}^{st}. Influence of all the above factors on fatigue strength of welded structures in service, except for the residual welding stresses, is expressed by basic S–N curves, found from relationship (2).

In this connection, it is proposed to establish the design S–N curve by correction of the appropriate basic S–N curve. The above correction consists in lowering of the endurance limit, based on 2 mln cycles, down to a value equal to endurance limit σ_R^r, allowing for the influence of a steady-state level of residual welding stresses. In this case, the condition is satisfied of coincidence of the design and basic S–N curves at cyclic stresses, corresponding to reaching stress levels equal to material yield point in the zones of a concentrator with factor α_σ, as in this case the residual welding stresses relax completely. Known experimental studies [5] show a coincidence of bounded endurance limits of welded joints without residual stresses and those with residual stresses of different level, if a cycle of alternating stresses of the same range with maximum stresses equal to material yield point is implemented in the stress concentrator zones.

The value of endurance limit $\sigma_{R_\sigma}^r$ is given by the following relationships [4]:

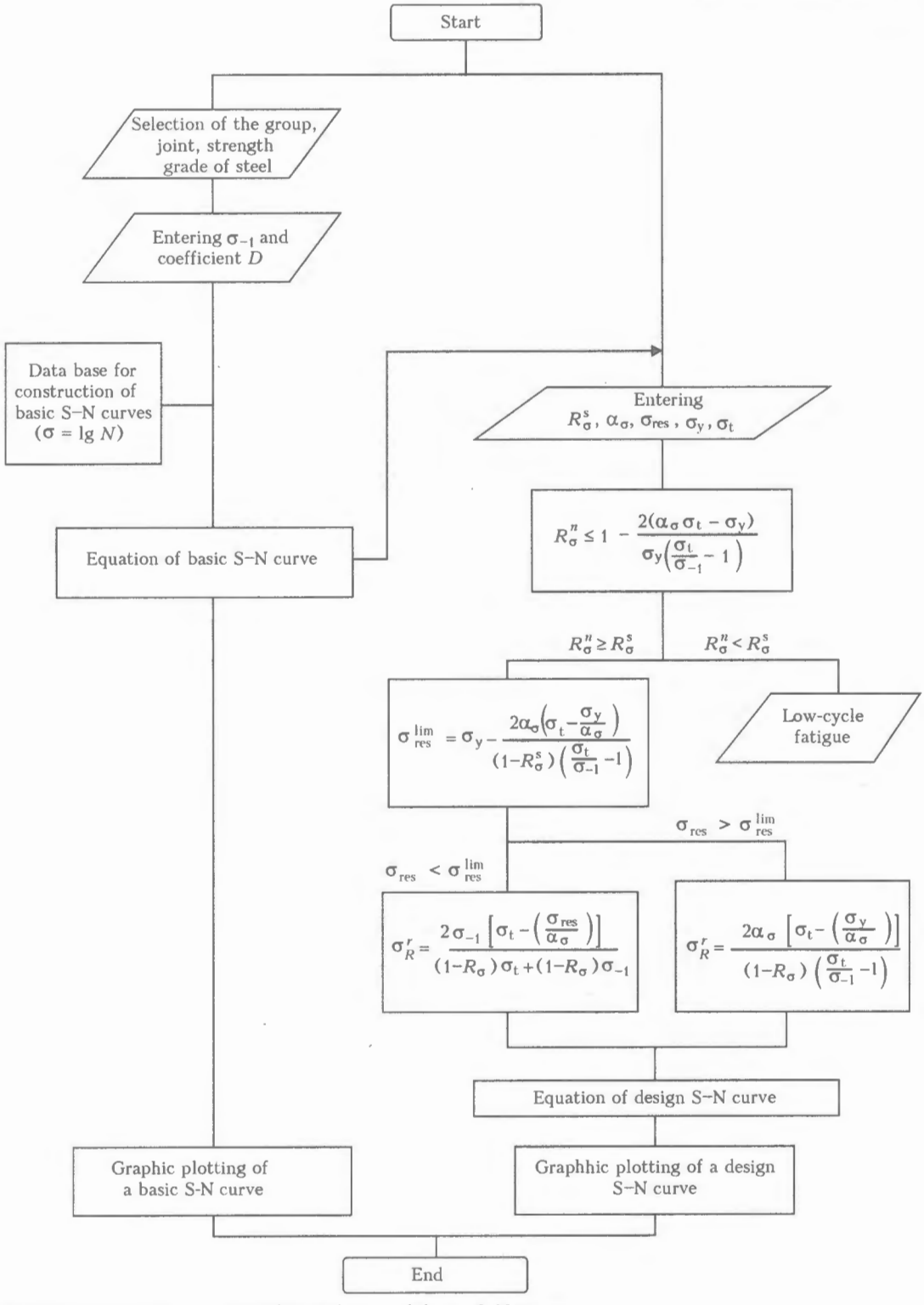

Figure 4. Block-diagram of a program for plotting basic and design S–N curves

$$\begin{cases} \sigma^r_{R_\sigma} = \dfrac{2\sigma_{-1}[\sigma_t - (\frac{\sigma_{res}}{\alpha_\sigma})]}{(1 - R^s_\sigma)\sigma_t + (1 + R^s_\sigma)\sigma_{-1}}, & \text{if } \sigma^{st}_{res} < \sigma^{lim}_{res} \\ \sigma^r_{R_\sigma} = \dfrac{2[\sigma_t - (\frac{\sigma_y}{\alpha_\sigma})]}{(1 - R^s_\sigma)(\frac{\sigma_t}{\sigma_{-1}} - 1)}, & \text{if } \sigma^{st}_{res} \ge \sigma^{lim}_{res} \end{cases}, \quad (3)$$

where R^e_σ is the service coefficient of cycle asymmetry; σ^{lim}_{res} are the limit values of residual stresses

$$\sigma^{lim}_{res} = \sigma_y - \frac{2\alpha_\sigma(\sigma_t - \frac{\sigma_y}{\alpha_\sigma})}{(1 - R^s_\sigma)(\frac{\sigma_t}{\sigma_{-1}} - 1)}.$$

These relationships allow for the influence of the level of steady-state residual welding stresses σ^{st}_{res} acting in a welded joint of a structural element in operation.

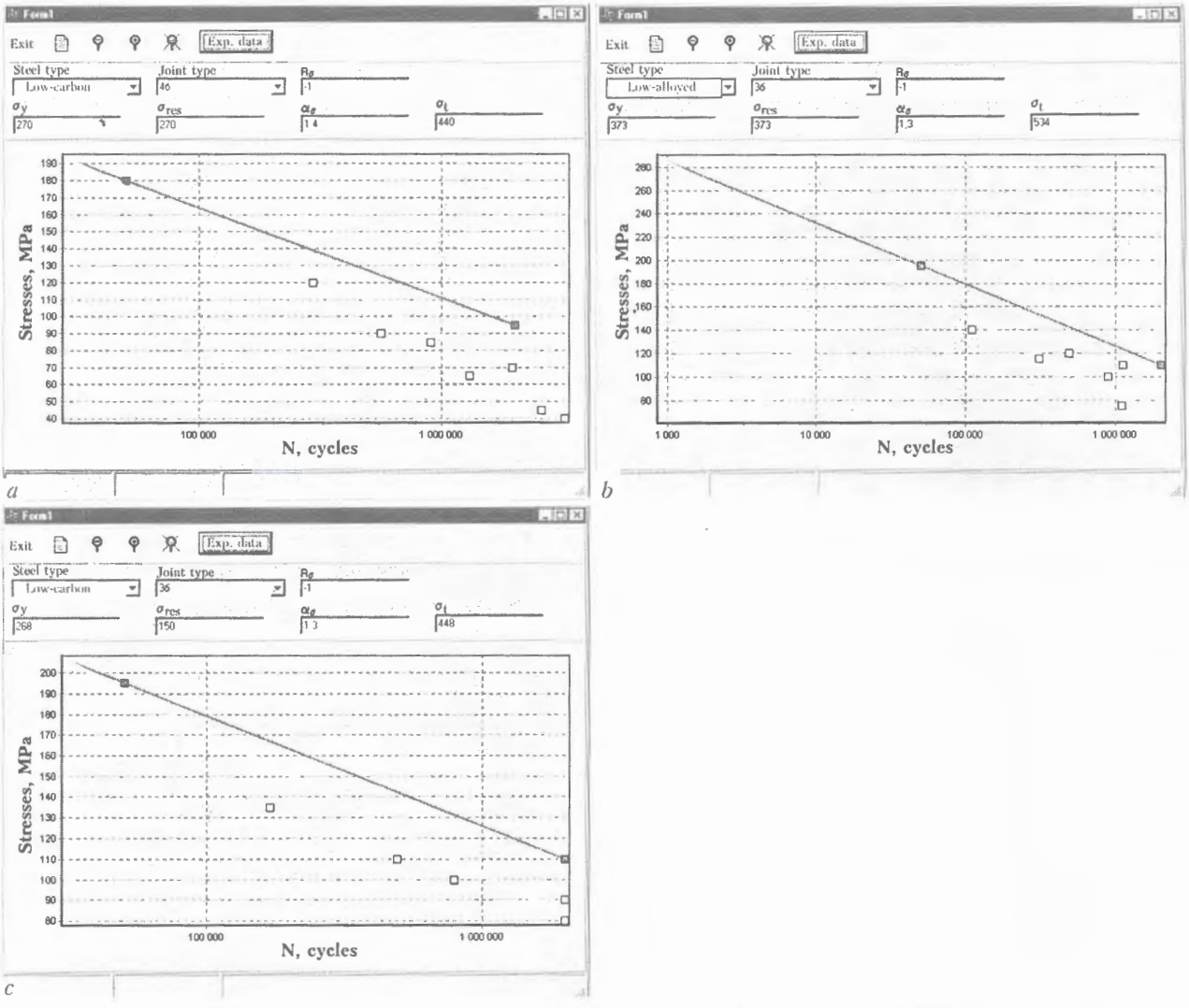

Figure 5. Comparison of a design S–N curve with the results of fatigue testing of the respective welded joints: *a* — element group 4, $\sigma_{res} \approx 0.6\sigma_y$; *b* — element group 3, $\sigma_{res} \approx \sigma_y$; *c* — element group 3, $\sigma_{res} \approx 0.6\sigma_y$; *dark curve* is basic S–N curve; *light curve* is design curve; *dots* are the results of fatigue testing of the corresponding welded joints

The above correction of the basic S–N curve actually consists in its rotation around a point with co-ordinates $(N_y, \sigma_y/\alpha_\sigma)$ in the co-ordinate plane $(N - \sigma)$ so that the corrected S–N curve (which is exactly the design curve), would run through a point with co-ordinates $(2 \cdot 10^6, \sigma_R^r)$. Then the design S–N curve of the main types of welded joints of load-carrying elements in metal structures currently in service with certain combinations of factors that determine their fatigue strength can be written as

$$\sigma = \frac{\sigma_R^r - \frac{\sigma_y}{\alpha_\sigma}}{6 + \lg 2 - \lg N_y} \lg N + \frac{(6 + \lg 2)\frac{\sigma_y}{\sigma_\alpha} - \sigma_R^r \lg N_y}{6 + \lg 2 - \lg N_y}. \quad (4)$$

Software for a personal computer was written for automation of the design procedures, when plotting the basic and design S–N curves. Program algorithm was written in C^{++} programming language, and is supported by Windows NT operating system. Block-diagram of the program is given in Figure 4. Data required for plotting the basic and design S–N curves are stored in Paradox data base.

When working with the program in the user format, it is necessary to select the strength grade of the steel and introduce σ_y and σ_t values corresponding to it, the group of element joint, corresponding value of the stress concentration factor α_σ, asymmetry of acting stress cycle R_σ, and value of the level of steady-state residual welding stresses σ_{res}^{st}. After that the program checks the entered data and performs the necessary calculations. Calculation results are presented in the graphic form as S–N curves in a semi-logarithmic scale $(\sigma - \lg N)$. If required, the program allows comparing the design S–N curve with the data obtained at experimental studies of fatigue strength of the respective joint. The developed program allows exporting the data and calculation results into such programs as Microcal Origin, MS Word, MS Exel.

Figure 5 gives a comparison of the design S–N curve derived by the proposed procedure with the experimental data. In the first case (Figure 5, *a*), fatigue testing at a symmetrical loading cycle (can-

tilever bending) was conducted using large-scale specimens of 200 × 30 mm section with transverse stiffeners, joined by fillet welds. Specimens were made of low-carbon steel M16S (σ_y = 270 MPa, σ_t = 440 MPa). Residual tensile welding stresses in the specimens reached values close to the yield point of steel.

In the second case (Figure 5, *b*) fatigue testing under the same loading conditions was conducted on specimens of 200 × 26 mm cross-section with a butt joint (low-alloyed 10G2S1 steel: σ_y = 373 MPa, σ_t = = 534 MPa). Similar to the first case, residual tensile welding stresses in the specimens reach values close to the steel yield point.

In the third case (Figure 5, *c*) the same loading conditions were used to test specimens of 200 × 30 mm section with a butt joint crossed by longitudinal deposits (low-carbon M16S steel: σ_y = 268 MPa, σ_t = = 448 MPa). Unlike the previous specimens, in this case the residual tensile welding stresses in specimens did not exceed ≈ 150 MPa. A lower level of residual stresses in the specimens is due to their relaxation under the impact of static overloading, applied before fatigue testing of the specimens.

Data given in Figures 5–7 is indicative of a satisfactory agreement of the design S–N curves of welded joints, obtained by the proposed procedure, and results of fatigue testing of similar type of joints, both with the limit tensile residual stresses, and with much lower residual stresses.

CONCLUSIONS

1. A procedure has been developed of computerized plotting of basic S–N curves for various types of welded joints, according to the classification of RD 50-694–90, based on the use of the respective diagrams of limit stresses, given in RD.

2. A procedure has been developed for plotting the design S–N curves of welded joints of metal structures in service, based on the change of the position of the respective basic S–N curves, depending on the experimentally established for a given metal structure characteristics of alternating loading cycle, value of the joint stress concentration factor, steady-state level of residual welding stresses and mechanical properties of the metal.

3. PC software has been created, which implements the proposed sequence of determination of design S–N curves for welded joints of metal structures in service for subsequent design evaluation of their residual life.

4. Performed comparison of design S–N curves of welded joints, derived by the suggested procedure, with the results of fatigue testing of large-scale specimens of low-carbon M16S steel and low-alloyed 10G2S1 steel is indicative of their satisfactory agreement.

1. *RD 50-694–90*. Reliability in engineering. Probabilistic method of fatigue analysis of welded structures. Moscow: Standart.
2. Trufyakov, V.I. (1973) *Fatigue of welded joints*. Kiev: Naukova Dumka.
3. (1990) *Strength of welded joints under alternating loads*. Ed. by V.I. Trufyakov. Kiev: Naukova Dumka.
4. Trufyakov, V.I., Mikheev, P.P., Kudryavtsev, Y.F. (1995) *Fatigue strength of welded structures. Residual stresses and improvement treatments*. Harwood A.P.
5. Gurney, T.R., Maddox, S.I. (1972) Determination of fatigue design stresses for welded structures from an analysis of data. *Metal Construction and British Welding J.*, 4(11), 418–422.

RESTORATION OF A CRUSHER MOVABLE JAW

V.D. POZNYAKOV, V.M. KIRIAKOV, Yu.V. DEMCHENKO and A.V. KLAPATYUK
E.O. Paton Electric Welding Institute, NASU, Kiev, Ukraine

The main approaches are considered which were implemented during restoration of intricate cast metal structures of 35L type steel, in which macro- and microdamages were developed during long-term service. Description of the sequence of process operations during repair of a movable jaw is given.

Keywords: *repair welding, medium-carbon steel, solidification cracks, cold cracks, residual welding stresses, welding heat input, weld metal, chemical inhomogeneity*

At Shargorodsk crushed rock factory for the primary crushing of marble of density exceeding 3000 kg/m^3, a jaw crusher with a simple swinging of a movable jaw is used since 1991. It was manufactured in Bulgaria in 1990 and is a unique metal structure designed for a primary crushing of sand rock of density up to 2400 kg/m^3. It consists of the following elements: a framework, movable and stationary jaws, connecting rod, distance plate with closing springs, positive stop and others (Figure 1). In accordance with technical characteristics the crusher is designed for 20 years of a failure-free operation. In a manufacturing cycle of crushed rock it is the most important element and its failure leads inevitably to the factory stoppage.

In 2003 (after 12 years of the operation commencement), one of distance plates and a crusher movable jaw failed. The earlier period of exhaustion of the crusher service life than that envisaged by the standardized documentation was, probably, caused by the specifics of its service. As the density of the marble is higher greatly than the density of materials, for which this crushing equipment is designed, then the loads were increased on its main load-carrying elements (distance plate and movable jaw).

A distance plate is a changeable plate of a rectangular section. Its replacement does not encounter any difficulties. A movable jaw is a cast honey-comb intricate structure of more than 7 t mass. The manufacture of the new jaw requires significant expenses and stoppage of manufacturing for indefinite time.

In this connection, the need was arisen in the development of alternative methods for recovery of the crusher working capacity, being inexpensive and low-time consuming. It was decided to restore by welding the integrity of the movable jaw at the site of the

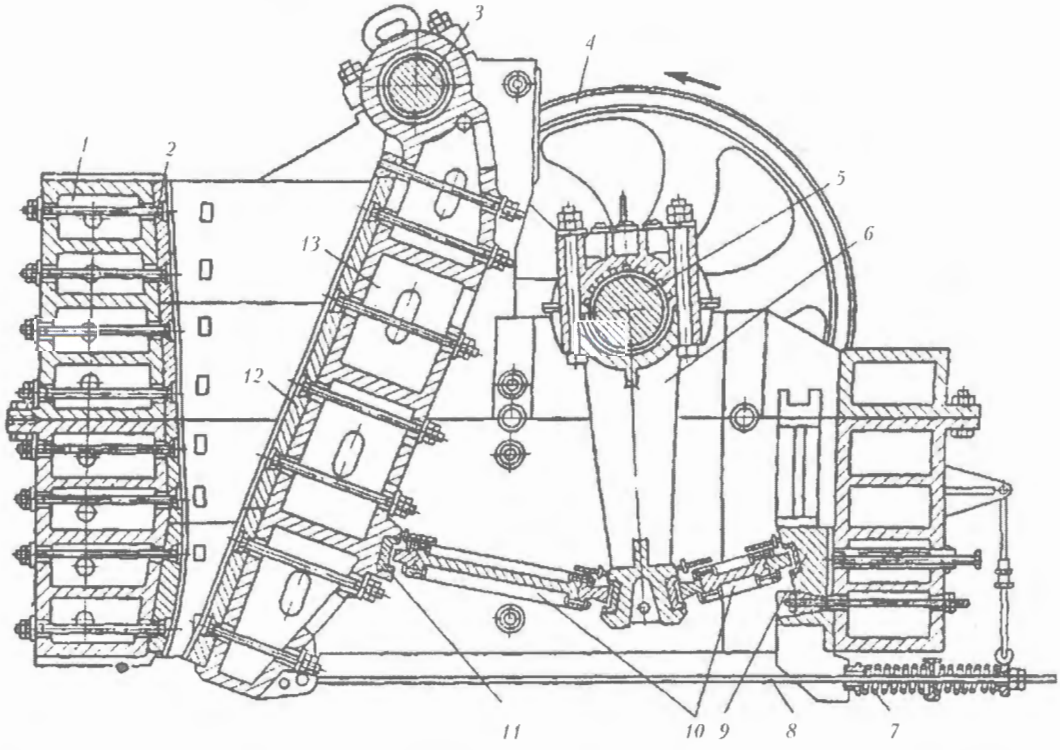

Figure 1. Scheme of crusher jaw: *1* — framework; *2* — armored plate on stationary jaw; *3* — axle; *4* — flywheel; *5* — eccentric shaft; *6* — connecting rod; *7* — spring; *8* — thrust; *9* — adjusting device; *10* — distance plates; *11* — insert; *12* — armored plates; *13* — movable jaw

structure operation in a short time and at a relatively small material expenses.

To develop the operating technology of repair, the specialists of the STC «The E.O. Paton Electric Welding Institute» inspected the fractured elements of the movable jaw, determined the chemical composition and made the metallographic examination of the cast metal.

The visual inspection of the movable jaw showed that the fracture occurred at the area, adjacent to the distance protective plate (Figure 2). Firstly, a fatigue crack was formed in the upper girth of jaw of 50 mm thickness under the action of impact loads. Later on, it was increased and damaged the upper girth over the entire its length. Then, the fatigue fracture initiated also a brittle avalanche fracture of vertical stiffeners of the jaw lower girth (Figure 3).

The condition of cast metal after long-time service was evaluated from the results of investigation of metal samples which were taken from damaged areas of the movable jaw. One part of samples was used for determination of chemical composition, and another part was used for preparation of sections and metallographic examinations.

Chemical composition of metal was determined in unit «Spectrovac-1000». It was found that metal, from which a crusher movable jaw was manufactured, corresponds to the domestic steel 35L and contains 0.36–0.41 % C; 0.36–0.40 % Si; 0.50–0.58 % Mn; 0.024 % S; 0.034 % P.

Structure and non-metallic inclusions were examined in microscope «Neophot-32», and microhardness of metal was determined in hardness tester of LECO company at 50 g load. Interface was examined in scanning microscope JSM-840, furnished with a microanalyzer «Link».

Analysis of polished sections revealed the non-metallic inclusions of manganese sulphides, double iron-manganese sulphides, sulphoglasses of complex composition, silicon dioxides and iron oxides. Contamination of metal with sulphides is estimated by 2–4 numbers, while that with oxides is estimated by 3–4 numbers by GOST 1778. Defects in the form of numerous voids in the region of location of fine-dispersed sulphides and oxides were also revealed in the metal.

The further examination of microstructure of cast metal was made after chemical etching of microsections in 4 % alcohol solution of nitric acid. The investigations showed that microstructure of metal is not homogeneous and consists of ferrite and pearlite of microhardness $HB_{0.05}$ 1105–1320 and 1810–1980 MPa, respectively. Size of grains corresponds to 1–2 numbers by GOST 5639.

Analysis of metal surface confirmed that fracture was occurred by two mechanisms. Firstly, a fatigue crack was initiated and propagated in the movable crack, that is proved by the presence of a clearly expressed stream pattern in this region. Then, the crack began to propagate by a mechanism of a brittle fracture with its typical direct fracture (normal to surface) at a relatively low level of plastic deformation and low absorbing energy. In this case the crack is propagated, as a rule, at a high rate.

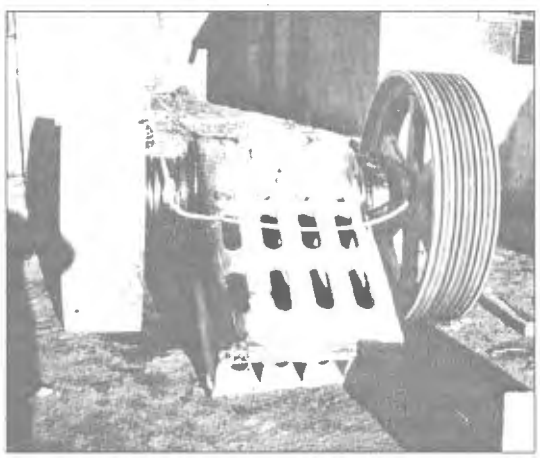

Figure 2. General view of damaged component of crusher jaw

Thus, the investigations revealed a number of the following peculiar features which can be taken into account when developing the technological processes of repair welding of the crusher movable jaw:

- increased carbon content in metal;
- chemical and structural inhomogeneity of cast metal;
- presence of regions with defects of casting;
- presence of areas with micro- and microcracks in site of stiffeners adjacent to upper and lower girths;
- difficult access to inner stiffeners of the jaw.

The increased carbon content in steel predetermines already itself the difficulties in welding, such as low resistance of weld metal against crystalline cracking, feasibility of formation of quenched structures in HAZ metal and, as a consequence, the cold cracking. In this case the welding of medium-carbon steels should be performed with preheating up to 200–350 °C [1]. However, due to large thickness of metal and total mass of structures, and also conditions of fulfillment of works at the factory, it was impossible to realize this.

Investigations showed that it is also possible to prevent the formation of crystalline and cold cracks in repaired welded joints at the lower temperatures of preheating. For this, the carbon content in weld

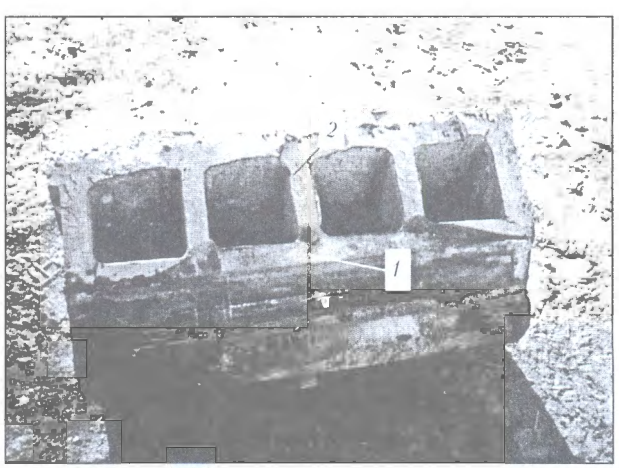

Figure 3. Appearance of interface (fracture) of crusher movable jaw: *1* — area with a fatigue fracture; *2* — area with a brittle fracture

metal should be limited and the level of residual tensile stresses in welded joints should be reduced.

By analyzing the possible ways of saturation of weld metal with carbon, it was decided to use the specialized electrodes for cutting to prevent cracks and edge preparation, and to use electrodes, as welding consumables, which will provide the deposited metal with ductility $\delta_5 \geq 30$ % and carbon content of not more than 0.07 %. In addition, the welding conditions should provide the minimum penetration of the parent metal and maximum value of the weld shape factor.

As the analysis of domestic and foreign publications, devoted to the problems of repair-restoration of different-purpose metal structures, shows [2–5], the high level of residual stresses in welded joints is one of main causes of their premature fracture which can occur both at the stage of repair works and also at the process of their subsequent service. To remove the welding stresses, the high-temperature tempering of products is, as a rule, used. However, taking into account the specifics of the product being repaired and technical capabilities of the enterprise, at which the repair works were made, it was necessary to find the way of reducing residual stresses, alternative to heat treatment. This required special investigations based on modeling the processes of repair welding of thick-plate structures.

The typical feature of the repair welds is their high rigidity. Therefore, the proceeding of thermodeformational processes in restrained joints depending on welding conditions was investigated and the effect of different kinds of postweld treatment on the feasibility of control of stressed state in welded joints was studied. This made it possible to establish the following.

In traditional welding with a rigid fixture of joints, the longitudinal and transverse stresses are formed whose level reaches $(0.8–0.9)\sigma_y$ of the parent metal. It is possible to reduce stresses by 30–40 % using weld metal peening with a specialized tool.

The control of welding stresses by the selection of definite sequence of layout of welds in groove filling, that also contributes to the reduction of stressed state of the joint, occurred to be rather effective. Combination of these two approaches gives an opportunity to reduce the residual tensile stresses in elements being restored to the level which does not exceed $(0.3–0.4)\sigma_y$.

Restoration of integrity of internal technological stiffeners in hard-to-reach places required special technical solutions. In this case the welding was performed by specialized high-efficient electrodes with highly-basic coating which provide good values of welding-technological characteristics and a necessary complex of properties of the deposited metal.

Welding was performed using a bath method. Weld of a required configuration was formed by using a special jig, developed for the bath welding and also electrodes providing high slag fluidity.

From the results of investigations the general technical solutions for the restoration of a crusher jaw and also general approaches to the technology of repair welding were worked out. Here, a complex nature of fracture, increased content of carbon in metal welded, and also the chemical and structural inhomogeneity of casting, the presence of areas with micro- and macrocracks, forming unfavorable fields of stresses caused by welding and the conditions of loading of the element were taken into account.

Technological process of repair included the following operations:

- determination of length of cracks by the NDT methods in sites of vertical stiffeners mating with lower and upper girths of a movable jaw;
- removal of cracks formed in sites of vertical stiffeners mating with lower and upper girths of movable jaw, edge preparation and filling the formed groove;
- edge preparation at abutted parts of the movable jaw;
- assembly of damaged elements of a movable jaw;
- welding in accordance with recommendations, developed at the E.O. Paton Electric Welding Institute, where 230 kg of electrodes were used;
- works on reduction of level of residual stresses in welded joints;
- removal of weld reinforcement flush with the parent metal;
- NDT of welded joint;
- restoration by surfacing of rests for armored plate and surface of movable jaw mating with an armored plate;
- cleaning of deposited surface of movable jaw to provide a sound contact between the movable jaw and armored plate.

Restoration works carried out in April, 2003 at Shargorodsk crushed rock factory took six days at three-shift work. Highly-skilled welders were involved in this work.

The restored movable jaw is operating at present under the condition of loads which exceed the design loads.

The experience gained in repair of the crusher movable jaw showed that the integrated approach to the solution of technical problem including the evaluation of condition of metal structure, modeling of technological processes, author's supervision of works, the inviting of specialized organizations for the accomplishment of these works makes it possible to provide the restoration and extension of service life of unique structures in a short time and at a high quality.

1. (1975) *Handbook of welder*. Ed. by V.V. Stepanov. Moscow: Mashinostroenie.
2. Irving, R.R. (1980) Can industry afford the high cost of weld repair. *Iron Age*, **3**, 49–55.
3. Larionov, V.P. (1986) *Electric arc welding of structures in northern realisation*. Novosibirsk: Nauka.
4. Dixter, R.J., Kelly, B.A. (1997) Research on repair and improvement methods. In: *Proc. of IIW 50th Annual Assembly Conf. on Performance of Dynamically Loaded Welded Structures*, San Francisco, July 14–15, 1997.
5. Dokunin, A.V., Semencha, P.V., Goldbukht, E.E. et al. (1982) *Improvement of strength and life of mining machines*. Moscow: Mashinostroenie.

HYDRATION OF FLUXES WITH A LOCALLY-CHANGED CHEMICAL COMPOSITION OF GRAINS

V.G. KUZMENKO[1] and V.I. GUZEJ[2]
[1]E.O. Paton Electric Welding Institute, NASU, Kiev, Ukraine
[2]Kiev City Administration, Ukraine

Investigation results on peculiarities of hydration of some grades of welding fluxes, e.g. fused ones and those subjected to preliminary thermal fluorination treatment in a gaseous environment containing HF, are presented. Formation of a low-hydrated layer on the surface of flux grains leads to a dramatic decrease in their susceptibility to moisture absorption. This treatment is especially efficient for fluxes of the basic type and those that have a pumiceous grain structure.

Keywords: *electric arc welding, fluxes, hydration, fluorination treatment*

The presence of excessive moisture in fluxes in welding promotes the saturation of weld pool and weld metal with hydrogen, that leads to the porosity and significant reduction in the level of its mechanical properties. Therefore, the limitation in susceptibility to hydration is one of main problems which should be solved in the development and use of welding fluxes [1].

There are several ways for the solution of this problem. The first way consists in adding of low-hydrated components into the composition of fluxes. Their list includes oxides of silicon, aluminium, titanium, zirconium, and fluorides used widely in making the composition of fluxes. They are little prone to hydration. However, some components intensify the moisture absorption by fluxes, for example, oxides of alkali and alkali-earth metals, and, calcium oxide in particular, existing most often in fused fluxes. The way, in which the degree of hydration of fluxes owing to the selection of appropriate components, is sufficiently effective and used widely in the development of fluxes of acid and neutral types. However, difficulties are encountered often in the development of highly-operational welding fluxes of basic type, where the presence of acid oxides is limited, but the oxides of basic type are rather completely presented.

The second way is the deposition of a layer of elements, possessing sealing and hydrophobizing properties, on the surface of flux grains [2]. This treatment decreases also significantly the moisture absorption. For this purpose, the conductance of a special additional treatment of flux is required, but, here, such undesirable impurities can be introduced into it as nitrogen, carbon and others. In addition, these coatings are not heat-resistant sufficiently, that limits the heat treatment of fluxes.

One more way for the solution of this problem is possible. It envisages the redistribution of components within the volume of flux grain, as a result of which the components, less susceptible to hydration, are arranged at the surface of grains. In this case a barrier layer is formed protecting the inner volume of flux grains from the interaction with air. Probably, it is impossible to provide such redistribution of components in the volume of grain of fluxes in use of the existing technology. Therefore, we have studied the feasibility of realization of this aim by using a special treatment providing the replacement of oxygen in surface layer of flux grains by fluorine.

It is known that fluorine and hydrogen fluoride (HF) are interacted intensively with oxides, forming appropriate fluorides [3]. Reaction of the hydrogen fluoride with oxides can be presented in the form

$$Me_2O + 2nHF = 2MeF_2 + nH_2O.$$

In making compositions of fluxes it is preferable to use such oxides as SiO_2, MnO, CaO, Al_2O_3, MgO, TiO_2, ZrO_2, FeO, K_2O, Na_2O. The following fluorides correspond to them: SiF_4, MnF_2, MnF_3, CaF_2, AlF, AlF_3, MgF_2, TiF_2, TiF_3, ZrF, ZrF_2, ZrF_3, FeF_2 [3]. Almost all the mentioned fluorides are in a solid state at sufficiently high temperature, except silicon tetrafluoride SiF_4, which forms gas at room temperature [3, 4]. Nevertheless, the silicon tetrafluoride can also form a sufficiently stable compound of $MeSiF_6$ type [3]. All the above-mentioned fluorides are formed in a surface layer of flux grains, and their solid state predetermines the sufficiently high degree of heat resistance and strength of bond with a material of the flux grain. This flux can be produced both as a result of interaction with water F-containing solutions and also in treatment with appropriate gaseous reagents. Probably, the latter variant is more preferable owing to the more effective contact of gas with a surface treated, reduction in level of diffusion limitations of chemical reaction and feasibility of combination of flux treatment by F-containing gases with its calcination. In this case the saturation of fluxes with fluorine will be determined by the diffusion of F-containing gas into the flux grain and will depend on the rate of its chemical reaction with oxides. Distribution of fluorine content in flux grain can be presented by the expression [5]

$$C_F = C_{F_1} \exp\left[-\sqrt{K/D}\,x\right],$$

where C_{F_1} is the fluorine concentration at the surface of flux grain; K is the constant of rate of chemical reaction of a gaseous reagent with a flux material; D is the coefficient of gas diffusion into the volume of flux grain; x is the distance from grain surface to the point considered.

In accordance with the above-given formula a formation of layer as a result of fluorination treatment of flux can be expected, in which the fluorine content will be maximum at the surface and decreasing monotonically with the movement inside the grain [5]. Here, the effect of fluorination treatment is intensified in basic fluxes, especially in those having the developed surface (pumiceous structure of grains).

Gaseous fluorine and hydrogen fluoride are used as fluorination reagents in chemical industry. However, to use them for treatment of fluxes is rather difficult and requires keeping definite safety measures. Probably, the solid salts at room temperature and easily-decomposing salts in heating of hydrofluoric acids such as KHF_2, $NaHF_2$, NH_3nHF, $(NH_3)_2SiF_6$, $MgSiF_6$ are more preferable for these purposes:

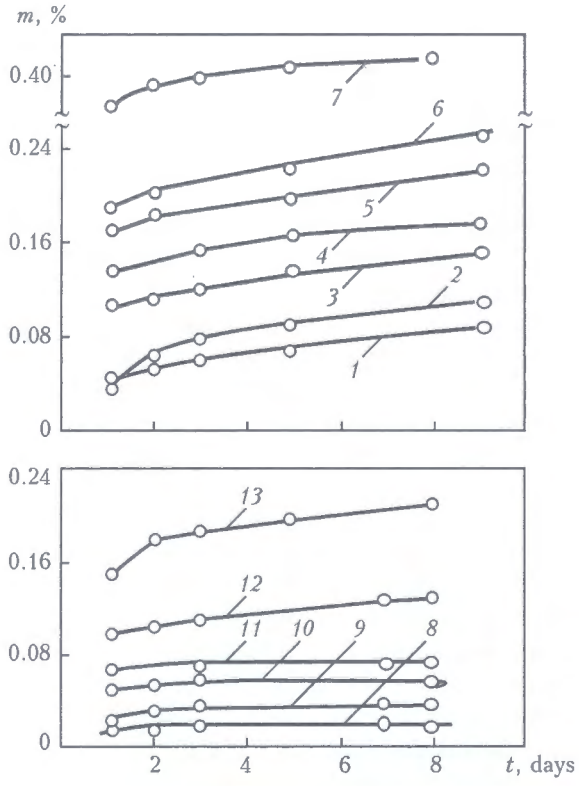

Figure 1. Kinetics of hydration of standard fluxes of different grades: AN-20S (*1*), AN-348-A (*2*), AN-18 (*3*), AN-20P (*4*), AN-60 (*5*), AN-26P (*6*), 48-OF-10 (*7*), AN-22 (*8*), AN-47 (*9*), AN-26S (*10*), OSTs-45 (*11*), AN-65 (*12*), AN-15 (*13*); m — increase in flux mass; t — time of holding

$$KHF_2 = KF + HF\uparrow;$$
$$NaHF_2 = NaF + HF\uparrow;$$
$$NH_3nHF = NH_3\uparrow + nHF\uparrow;$$
$$(NH_3)_2SiF_6 = 2NH_3\uparrow + 2HF\uparrow + SiF_4\uparrow;$$
$$MgSiF_6 = MgF_2 + SiF4\uparrow.$$

Ammonium salts are most suitable as a source of F-containing gases as they have a low (somewhat higher than 100 °C) temperature of decomposition and form here only the gaseous products [3].

We have conducted investigations on susceptibility of standard fluxes of 13 grades to hydration (AN-348-A, AN-20S, AN-18, AN-20P, AN-60, AN-26P, 48-OF-10, AN-22, AN-47, AN-26S, OSTs-45M, AN-65, AN-15) in initial state and some of them after the fluorination treatment.

Initial fluxes were calcinated at temperature 500 °C, and then placed into an exsiccator filled with water, where the humidity close to 100 % and temperature approximately 20 °C were provided. The duration of fluxes holding in the exsiccator was 9 days. Each day the samples were weighed at the same time (at accuracy $1 \cdot 10^{-5}$ g), whose results are presented in Figure 1.

The fluxes of AN-20P, AN-348-A, AN-60, 48-OF-10, AN-26P, AN-22, AN-65 and AN-15 were hold simultaneously in the same exsiccator and were subjected to a periodic control of change in mass. All they were subjected preliminary to the fluorination treatment, which consisted in calcination of flux mixture of each separate grade with 5 % NH_4F in a closed container at 500 °C temperature for 1 h.

Kinetics of change in mass of samples of fluorinated fluxes in the process of moistening is presented in Figure 1, curves *8–13*. As the relatively low increment in mass of fluxes was observed during 10 days, the holding of fluorinated fluxes in exsiccator was increased up to 18 days. As is seen in Figure 1, the process of moisture absorbing of standard fluxes was proceeding in two stages. Maximum increment in mass of fluxes was observed in the first days. Here, the highest susceptibility to hydration was displayed by basic-type fluxes (AN-15), in particular with a pumecious structure of the grain (48-OF-10). The very factor of presence of this structure of grains is determinant for intensification of moisture absorbing even in clearly expressed acid fluxes (AN-60). The further holding of standard fluxes in the exsiccator shows the negligible their increase in moisture absorbing, has a monotonous mode and, here, the tendency to their saturation with moisture is manifested.

The mode of change in moisture absorbing of fluxes subjected to fluorination treatment is differed radically from that in standard fluxes (Figure 2). In the latter the level of saturation with moisture in the first days of holding is 4–10 times lower than that in fluxes of basic type (AN-15), and also in basic (48-OF-10) and acid fluxes (AN-60) with a pumecious structure of grains. For fluxes of acid and neutral types with a glassy structure of grains this characteristic is in-

creased (3–4 times). Nature of behaviour of fluorinated fluxes at a further holding has also great differences. On the 8–10th days some increase in mass of samples is observed. This is, probably, associated with a partial penetration of humid air through a protective barrier formed by highly-fluoride layer at the surface of flux grains. Then, the rate of moistening of samples is somewhat increased. Nevertheless, even after holding during 18 days the increment in moisture in samples of fluorinated fluxes is 1.5–2 times lower than that in untreated fluxes after holding during 8 days.

By generalizing the obtained results of comparative investigations of mode of hydration of some standard welding fluxes and those subjected to fluorination treatment it can be concluded that this treatment is an effective means for limitation of their saturation with moisture. Fluxes, subjected to treatment, can be used without calcination at least during two-three weeks from the moment of their manufacture.

CONCLUSIONS

1. Fluorination heat treatment of a number of standard welding fluxes in the medium, containing gaseous hydrogen fluorides (HF), leads to the formation of grains with a locally-changed chemical composition that occurs due to replacement of oxygen by fluorine in their surface layer.

2. Due to the formation of a low-hydrating protective layer from fluorides at the surface of fluxes grains, their susceptibility to hydration during holding in humid atmosphere is 2–4 times reduced.

3. The fluorination treatment is especially effective as regards to fluxes of basic type, also to fluxes having a pumiceous structure of grains for which the problem of hydration is especially actual.

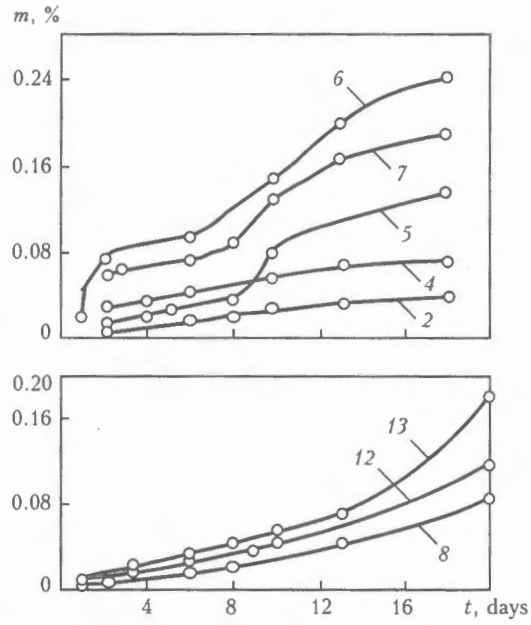

Figure 2. Kinetics of hydration of standard fluxes of different grades passed fluorination treatment at 500 °C temperature in mixture with 5 % NH_4F (see designations in Figure 1)

1. Podgaetsky, V.V., Lyuborets, I.I. (1984) *Welding fluxes*. Kiev: Tekhnika.
2. Bender, V.S., Makeev, S.D., Galinich, V.I. et al. *Method of granulation of flux*. USSR author's cert. 492368. Int. Cl. B 23 K 35/36. Publ. 25.11.75.
3. Ryss, I.G. (1956) *Chemistry of fluorine and its inorganic compounds*. Moscow: Goskhimizdat.
4. Wicks, K.E., Blok, F.E. (1965) *Thermodynamic properties of 65 elements, their oxides, halogenides, carbides and nitrides*. Moscow: Metallurgiya.
5. Zhukhovitsky, A.A., Shvartsman, L.A. (1973) *Physical-chemical principles of metallurgical processes*. Moscow: Metallurgiya.

OPTICAL GENERATORS OF LIGHT PLANE FOR TECHNICAL VISION DEVICES OF SYSTEMS OF ARC WELDING AUTOMATION

F.N. KISILEVSKY and **E.V. SHAPOVALOV**
E.O. Paton Electric Welding Institute, NASU, Kiev, Ukraine

Possible methods of designing light plane optical generators, which may be used in triangulation systems of technical vision of arc welding automation systems are considered, and some comparative characteristics of different kinds of optical generators of the light plane and recommendations on their application with different types of the groove are given.

Keywords: *arc welding, process automation, technical vision system, light plane, gap measurement, joint line, grooved butt*

Various sensors are used as feedback elements in systems of automation of arc welding processes. By the principle of their operation they are divided into arc, eddy current, tactile, optical, etc. The main advantages of optical sensors include contactlessness, information content, and accuracy. These features make optical sensors indispensable when solving diverse problems of automation of welding production, nondestructive testing, assembly production, etc.

Over the last years intensive development of computing systems and electronics enabled application of optical sensors to control the arc welding process in ship-building, pipe manufacturing, aircraft and aerospace industry, etc.

The majority of optical sensors are based on the method of triangulation (Figure 1). The principle of operation of such sensors is described in greater detail in [1–5]. One of the main elements of an optical sensor based on the triangulation method is light plane optical generator (LPOG). Light band *4* forms, when light plane *6* crosses surfaces being welded *5*.

The purpose of this study is consideration of the possible methods of LPOG construction, as well as comparison of some technical characteristics of various LPOGs.

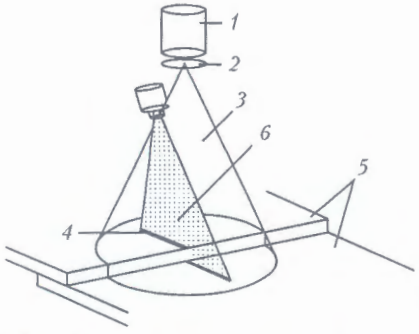

Figure 1. Schematics of a sensor operating by the light section method: *1* — videocamera; *2* — interference filter; *3* — LPOG; *4* — light band; *5* — surfaces being welded; *6* — light plane

Known are several methods of LPOG construction, namely:

- mechanical scanning of the laser beam;
- multiple refraction of the laser beam in a prism system;
- use of taper-prismatic concentrator;
- use of a specialized line generator lens (LGL);
- use of cylindrical optics.

When building LPOG with a mechanical scanning of the beam, the laser diode (laser module) is usually rigidly fastened, and the mirror makes reciprocal motion.

LPOGs with mechanical scanning have several serious drawbacks, which limits their application:

- presence of mobile parts and additional electronic block, controlling the scanning of the laser beam;
- non-uniform brightness of the light band, caused by that the velocity of the light beam is different at the edges and in the center of the band;
- large overall dimensions and considerable weight.

Mirror vibration frequency should be higher than the vertical sweep frequency of the videocamera, and it is usually equal to 300–400 Hz. LPOGs with mechanical scanning have a low reliability, and they are practically not used because of their drawbacks.

A rather interesting method to obtain the light plane is multiple refraction of the laser beam in a system of prisms (Figure 2). The figure shows the beam path in the optical system, consisting of ten prisms (material is fused quartz).

To reduce the losses, the beam is applied to the prism at Brewster angle:

$$\operatorname{tg} \theta_{Br} = \frac{n_2}{n_1},$$

where θ_{Br} is the Brewster angle; n_2 and n_1 are the refraction indices.

Lower losses are due to that for a wave, the electric vector of which is in the incidence plane, the reflected wave at angle of incidence θ_{Br} is completely absent. An advantage of such LPOG is the fact that the outgoing beams are parallel to each other. Their totality

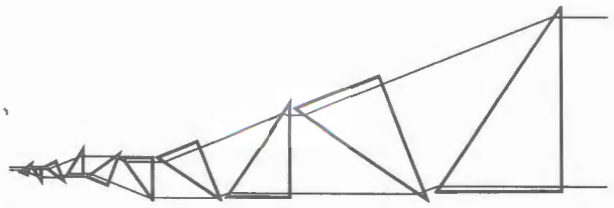

Figure 2. Beam path in the prism system

forms a light plane, where all the beams have the same intensity.

The disadvantages include the following:

- large overall dimensions of the illuminator. At incoming beam diameter of 1.5 mm and width of outgoing beam of 60 mm, the minimum overall dimensions of the illuminator are 100 × 70 × 20 mm;
- considerable losses of laser radiation power, when going through a system of prisms, which may be up to 35–40 % of power. These may be reduced, using antireflective prisms.

There also exist sources of rather powerful radiation, namely superluminescent light-emitting diodes (LED), which are an alternative to semi-conductor lasers. A matrix providing a light flow of a quite high power can be formed from individual LED. Its has the disadvantage of the radiation of a LED group being insufficiently monochromatic. The width of radiation line on the level of 0.5 of maximum intensity is 25–30 nm, which is by an order of magnitude wider than in semi-conductor lasers.

The E.O. Paton Electric Welding Institute developed a radiation module [1], based on LED-matrix (Figure 3). A matrix of 50 mm diameter included 37 LED of HLMP-ED16TW000 type of Hewlett-Packard company. The estimated total radiating power of such a matrix was 100–150 mW ($\lambda_0 \approx 620$–640 nm).

A glass taper-prismatic concentrator with an entrance aperture of 42 mm diameter and exit aperture in the form of a 15 × 0.4 mm rectangle (38:1 side ratio) was selected and implemented as an optical-physical and design solution for an optimal optic element, providing higher uniformity of radiation across the section of the light flow of the primary radiator (LED-matrix) and conversion of the light flow into a plane. The disadvantages of this LPOG are large dimensions and considerable weight.

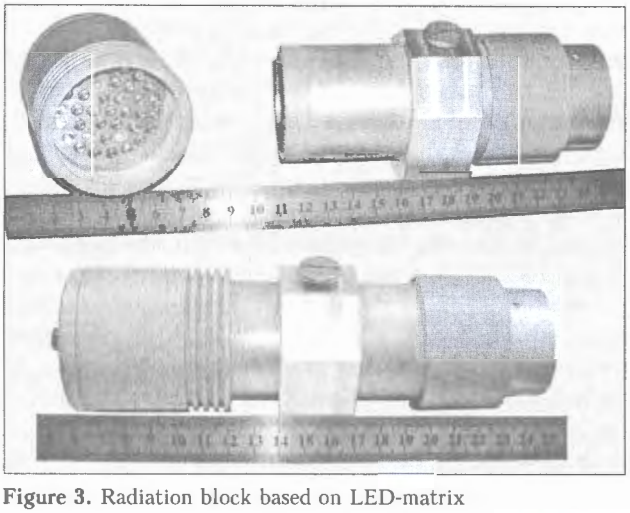

Figure 3. Radiation block based on LED-matrix

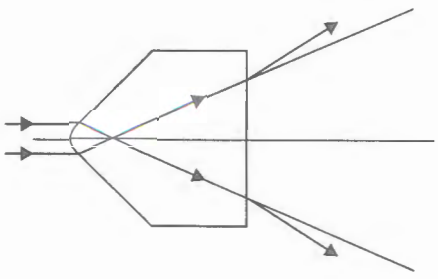

Figure 4. Beam path in a specialized lens

PWI tried out LPOG based on a specialized LGL (Figure 4) [5]. A laser diode of about 30 mW power, $\lambda_0 \approx 670$ nm is used as the radiation source. The semiconductor laser crystal generates a beam with the divergence of 30–35° in one plane and 9–10° in another plane. The section of this beam is an ellipse with Gaussian distribution of intensive radiation. To generate a uniform light flow of 1.0–1.5 mm diameter LPOG uses a collimator, consisting of three microlenses.

Collimated laser radiation is evolved into a line using a specialized lens. This device evolves the radiation into a line by one co-ordinate, angle of divergence of the light beam being 50° at a focal distance of approximately 7 mm. Figure 4 shows the beam path of such a lens.

One of the most recent developments of PWI in the field of small-sized light plane generators is LPOG based on a cylindrical microlens (Figure 5). A laser module was selected as the radiation source. The device uses a cylindrical microlens with a short focal distance. LPOG optical circuit is shown in Figure 6. The main advantages of LPOG, based on a cylindrical microlens, are minimum overall dimensions and weight. The length of the entire LPOG is 36 mm, its diameter is 15 mm, and weight is 30 g.

For the conditions of arc welding the most acceptable LPOGs, taking into account their characteristics (overall dimensions, weight, cost, optical circuit efficiency) are those based on a cylindrical optics and a specialized LGL. The above characteristics have the same parameters for LPOGs of both types. The difference consists in that LPOG based on cylindrical optics has a normal distribution of radiation intensity. As dispersion is reduced with increase of the angles

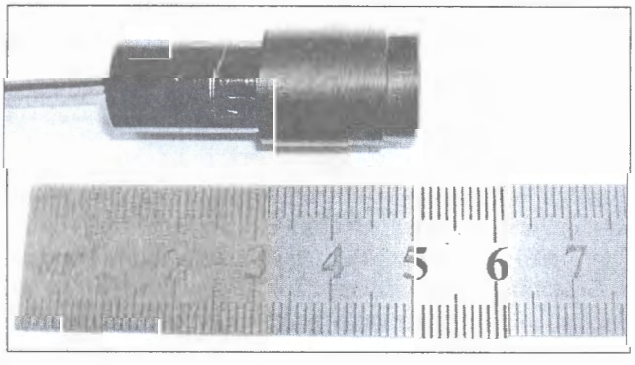

Figure 5. LPOG based on a cylindrical microlens

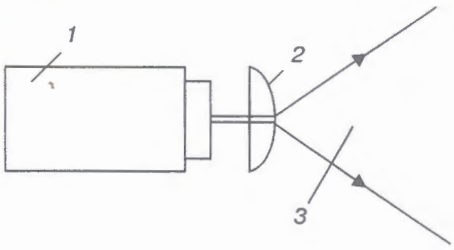

Figure 6. Schematic of LPOG based on a cylindrical microlens: *1* — laser module; *2* — cylindrical lens; *3* — light plane

of incidence of the light beams, in order to provide a uniform brightness distribution along the light band, it is rational to apply LPOG based on a cylindrical lens when welding surfaces with a deep groove.

Narrow-band interference light filters with the pass band $\lambda_{0.5}$ = 5–7 nm are used to protect the videocamera from intensive radiation of the welding arc. Transmission factor of the interference light filter decreases with greater angle of incidence (application) of the beams on this light filter. Therefore, it is rational to apply the LPOG using a specialized LGL, when a light plane with a large aperture angle is required. This is related to the fact that the light line formed by the light section has greater intensity on the edges, and not in the center, as in LPOG based on cylindrical optics. In an image obtained with a videocamera, such a light band will have a practically uniform brightness along the entire length.

LPOGs based on a taper-prismatic concentrator and mechanical scanning of the laser beam, are rarely used, because of the above drawbacks.

LPOGs based on cylindrical optics or specialized LGL, have a drawback, affecting the measurement accuracy because of non-parallelism of the light beams. If high requirements are made of the technical vision means in terms of the accuracy of measurement of the butt gap, in our opinion use of LPOG based on prisms is the most rational.

1. Kisilevsky, F.N., Butakov, G.A., Dolinenko, V.V. et al. (2001) Improvement of seam tracking quality on the base of technical vision. In: *Proc. of Int. Sci.-Techn. Conf. and Exhibition on Problems of Quality Assurance in Welding Production*, Kiev, April 3–6, 2001.
2. Ustinov, N.G., Karpilenko, A.V. (1992) Optical sensor for automatic welding. *Avtomatich. Svarka*, **7/8**, 37–40.
3. Boillot, J.-P., Noruk, J. (2002) The benefits of laser vision in robotic arc welding. *Welding J.*, **8**, 32–34.
4. Kisilevsky, F.N., Pritula, S.I., Dolinenko, V.V. (2003) System of guiding the welding torch along the butt using a TV sensor. *The Paton Welding J.*, **1**, 49–50.
5. Shapovalov, E.V., Klochko, A.I., Suzdalev, I.V. et al. (2003) System of technical vision of automatic control systems for arc welding technological process in shipbuilding. In: *Proc. of Conf. on Lasers. Measurements. Information*, St.-Petersburg, June 25–26, 2003.

PROCEDURE OF SELECTION OF PARAMETERS FOR PULSED FEED OF ELECTRODE WIRE

V.A. LEBEDEV
E.O. Paton Electric Welding Institute, NASU, Kiev, Ukraine

Some known methods for selection of the main parameters of the mechanism for pulsed feed of electrode wire are analyzed. Procedure for calculation of parameters of pulsed control of electrode metal transfer, based on energy characteristics of mechanized arc and electrode wire feed processes, is considered. It is proved that at selection of the parameters of pulsed motion of electrode wire it is necessary to take into account the limitations determining the stability of the arc process with a pulsed feed.

Keywords: *arc welding, consumable electrode, mechanized equipment, electrode metal transfer, control, spatter, losses, feed mechanism, optimization, pulses*

Scientific results have been accumulated [1] and new design developments have been made [2] recently to implement one of the promising methods to control electrode metal transfer in mechanized processes of arc welding with a pulsed electrode feed. The most recent engineering solutions in this field allow implementing a reliable pulsed feed of electrode wires of all the known types, namely solid, flux-cored (for the first time), steel and aluminium alloy wires. Designs of the modern mechanism of pulsed feed are such that they enable regulation of practically all the parameters of the generated pulses, namely frequency, pitch and shape. Proceeding from the above it can be stated that the pulsed method of electrode wire feed to control the electrode metal transfer is at such an engineering level, which can be considered as ready for application in mechanized arc welding equipment [1].

The purpose of this work is evaluation of the known procedures to select the main parameters of pulsed feed of electrode wire, as well as development of new procedures, allowing for the features of welding with the above-mentioned motion of electrode wire.

It is known [3] that forced transfer of liquid metal drops formed at the electrode wire tip at its pulsed feeding proceeds due to inertia forces acting on this drop. In this case the inertial force F_d required for

the drop detachment is given by the following relationship:

$$F_d > F_s + F_r - F_e(\pm F_m), \quad (1)$$

where F_s is the surface tension force; F_r is the force of reactive pressure of liquid metal vapours; F_e is the electromagnetic force; F_m is the force determined by the drop mass.

After the start of electrode wire melting, a drop forms at its tip, and magnitudes of forces F_s, F_r, F_e and F_m change as the drop grows. Each of these values depends both on the time of the drop existence and on a number of other physical and thermophysical parameters, i.e. for each of them the following relationship is valid in some form:

$$F_s = \pi r^2 \frac{2\sigma}{R}; \quad F_r = m_{ev} v; \quad F_e = AI^2; \quad F_m = m_{d.d} g, \quad (2)$$

where $\sigma = f(t^0, \gamma)$ is the surface tension factor of the drop; t^0 is the current temperature; γ is the specific weight of electrode metal; r is the electrode wire radius; R is the radius of the drop surface curvature; m_{ev} is the mass of metal evaporating from the surface per a unit of time; v is the initial velocity of the vapour jet; A is the proportionality factor; I is the arc process current; $m_{d.d}$ is the mass of the drops detached in the arc process without pulsed feed (traditional process of gas-shielded consumable electrode arc welding); g is the acceleration in the terrestrial gravity field.

In addition, some force characteristics, determining the behaviour of the electrode metal drop, are strongly affected by the composition of the shielding medium and welding mode, and the magnitude of F_m further depends on the welding position.

In the mechanized arc welding process with a controlled electrode metal transfer the goal is to provide a forced transfer of the drop into the metal pool. It is obvious that to obtain weld metal of a certain quality, as well as lower electrode metal spatter, its drops should have a certain size. This size is assigned or selected proceeding from the conditions of the possible minimum soaking of the molten metal in the arcing zone (to avoid burning-out of the alloying elements), and minimum inertia impact of the energy, also determined by the drop weight. The latter limitation arises from that the existing designs of feed mechanisms have limited capabilities of the required acceleration of the pulsed motion of electrode wire.

Determination of force characteristics, included into (1), is a complex problem, as the conditions of (2) must be taken into account.

There exist several procedures for selection of the parameters of mechanical pulses required to provide a forced detachment of the drop from the metal wire tip.

The procedure, proposed in [4], is based on that the following relationship can be the condition of the drop detachment in welding with a pulsed feed of electrode wire:

$$m_{d.sp} g' = m_{d.d} g,$$

where $m_{d.sp}$ is the mass of the drops specified for detachment in an arc welding process with pulsed feed of electrode wire; g' is the drop acceleration at the moment of its detachment with pulsed wire feed.

The above procedure does not envisage calculation of the values of characteristics included into (1), which significantly simplifies the procedure of finding the required acceleration of the wire at its pulsed feed as one of the main values that determine the requirements to the mechanisms of pulsed feed. The disadvantage of this procedure is that it requires having the data on time $t_{d.d}$ of detachment of electrode metal drop with the traditional arc welding process. In connection with the fact that $t_{d.d}$ also depends on a large number of parameters and conditions (current, voltage, composition of electrode wire and shielding gas, wire extension and diameter, etc.), it is proposed to determine these values experimentally. In view of a considerable scope of the required experimental studies of different arc welding processes and application of different materials, the above procedure becomes labour-consuming and is rarely used in practical work for selection of the pulsed feed parameters or development of mechanized arc welding equipment.

A procedure suggested in [5] is more advanced. It enables analytical study of the condition of forced detachment of an electrode metal drop. This procedure is used to determine the condition of equilibrium of an electrode metal drop, allowing for practically all the known forces acting on it. The condition of equilibrium of forces acting on the elementary area of the drop at pulsed motion of electrode wire was used to derive a certain generalized criterion Π, which is the ratio of Laplace pressure in a drop to the total force, also including the inertial force:

$$\Pi = 2\sigma_l / R_0 (g + g') h_{ax} r_l + F_e + F_r,$$

where σ_l is the surface tension force of liquid metal of the drop; R_0 is the curvature radius in the frontal point of the drop; h_{ax} is the axial size of the drop, which determines the volume of molten metal, to which the inertial force is applied at pulsed feed of electrode wire; ρ_l is the density of liquid metal of the drop.

It is established that at $\Pi < 8$ a guaranteed forced detachment of electrode metal is provided with each feed pulse. In our opinion, such an approach can provide a more accurate result, but requires conducting a large scope of calculations, and it further requires the data on variation of a number of physical characteristics of the metal at different temperatures and specific processes occurring in the arc. With a large number of them, when knowledge of the pulsed feed parameters is required, such a procedure is highly labour-consuming, and, as shown by experience, it is not used in practice.

When studying the process of electrode metal transfer by forced techniques, it should be taken into

account that it has the following forms: forced transfer with short-circuiting of the arc gap or without short-circuiting, similar to the long-arc process.

In the first variant the process of forced transfer is much simplified due to the presence of the surface tension forces, which at the final stage of the drop transfer promote its transition into the weld pool. It is obvious that in this case no significant acceleration of the pulsed motion of electrode wire is required for the action of inertial forces, which are sufficient for the drop detachment. It is only necessary to provide a shorter time of the drop existence at the electrode tip. In the case of forced transfer of electrode metal without short-circuiting of the arc gap, the action of inertial forces in the electrode wire–drop system should exceed the total action of those forces, which retain the above system in an undetached condition up to a certain time.

Earlier considered methods to determine the inertial forces as a result of action of a pulsed feed of electrode wire belong to the last case to a greater extent. It is obvious that such an approach to determination of mechanical control action should be regarded as correct. However, the complexity of using the proposed design procedures and the need to take into account the difficult-to-determine parameters make it necessary to look for a simpler method to evaluate the pulsed feed parameters, which could be readily used in practical design and in determination of the technological conditions of the welding process with a mechanical impact.

We propose a somewhat different new approach to solving the above problem.

This approach is based on comparison of the energy consumption required for detachment of an electrode metal drop at a stationary feed of electrode wire and forced detachment and transfer of the drop under the impact of mechanical pulses. To simplify determination of forces, acting on the electrode metal drop at the moment of its formation at stationary feed of electrode wire, let us represent the forces trying to separate the electrode metal drop and those retaining it, as a resulting value F_{res}, and let us designate as F_c the forces counteracting the drop motion into the metal pool. Proceeding from electrodynamic nature of detachment and transfer of the drops from the electrode wire tip [6], it can be noted that the forces of detachment of the above drop are ponderomotive forces (pinch-effect) and forces of gas-dynamic head. The force, retaining the drop at the electrode wire tip, is that of surface tension, and the force, preventing the drop motion into the metal pool, is the force of resistance to the medium, which in the arc gap is the plasma flow, having a certain viscosity and density. It is obvious that a combined action of the above forces at a certain stage of the drop growth ensures its detachment and transportation into the metal pool in the plasma flow. The resulting action imparts to the electrode metal drop kinetic energy W_e, which can be defined as

$$W_e = m_{d.e} v_{d.e}^2/2, \quad (3)$$

where $m_{d.e}$ is the mass of electrode metal drop under natural conditions of its detachment and transfer; $v_{d.e}^2$ is the velocity of electrode metal drop motion in a plasma flow under the natural conditions of its detachment and transfer.

It should be noted that the mass and velocity of motion of an electrode metal drop in a traditional arc welding process depend on a number of electrode material characteristics, shielding medium (shielding gas), as well as arc welding process parameters. Studies [7, 8] give analytical expressions for establishing the velocities of electrode drop motion after the drop detachment from the wire tip. In our study we will use a quite simple method of $v_{d.e}$ determination, suggested in [9]:

$$v_{d.e} = \frac{1}{d_{d.e}} \frac{ka}{1 + \sqrt{cd_{d.e}a}}, \quad (4)$$

where $d_{d.e}$ is the diameter of electrode metal drop, transferred naturally at a steady motion of the electrode; k, a, c are the coefficients, calculated by procedures taken from [9, 10].

In order to determine the mass of electrode metal, transferred naturally, it is possible to use the data from a number of studies devoted to problems of gas-shielded welding. In our investigations we used the data of [10, 11] etc., which are given in the form of tables or graphically and which determine the sought mass of the drop by one or several parameters:

$$m_{d.e} = f/(d_e, I_a, U_a, l_e, \text{electrode wire material, shielding gas type}),$$

where d_e and l_e are the electrode wire diameter and extension, respectively; I_a and U_a are the current and voltage of the arc process.

To simplify subsequent conclusions, let us make assumptions, which are required, when studying the processes of electrode metal transfer in welding, and part of which is given in [5, 10], namely:

- an electrode metal drop, which is transferred naturally or at control of mechanical pulses, has a constant shape, close to that of a sphere;
- electrode material, gas medium, plasma flow are the parameters unchanged in a transfer cycle and repeated for a number of cycles;
- metal drop density is the same at natural or forced transfer.

At mechanical control of the transfer, the magnitude of kinetic energy imparted to the drop, should be at least not less than that which provides a natural transfer of this drop. Proceeding from this consideration and allowing for (3), we can write the following relationship:

$$\frac{m_{d.con} v_{d.con}^2}{2} > \frac{m_{d.e} v_{d.e}^2}{2}, \quad (5)$$

where $m_{d.con}$ is the mass of electrode metal drop at a controlled transfer; $v_{d.con}$ is the velocity of electrode wire tip, at which a forced detachment of the drop proceeds at controlled transfer.

Study [12] gives the characteristics of controlled transfer of electrode metal, providing its low losses and acceptable shapes of the welded joint, where the criterion of the amount of the drop metal was taken to be drop diameter $d_{d.con}$, at which it is correlated with electrode diameter d_e:

$$d_{d.con}/d_e = \varepsilon, \quad (6)$$

where ε is the optimum number.

Let us express the drop diameter as its mass and substitute it into expression (5), which we will solve for sought value $v_{d.con}$. Allowing for (4), we have

$$v_{d.con} > \sqrt{\frac{d_{d.e}}{d^3_{d.con}} \frac{ka}{1 + \sqrt{cd_{d.e}a}}}. \quad (7)$$

Allowing for expression (6), inequality (7) can be written as

$$v_{d.con} > \sqrt{\frac{d_{d.e}}{\varepsilon d^3_{d.con}} \frac{ka}{1 + \sqrt{cd_{d.e}a}}}. \quad (8)$$

It should be noted that (7) and (8) make sense only at $d_{d.con} > d_{d.e}$. Otherwise the ability to control the transfer is lost.

When studying the pulsed feed of electrode wire, electrode wire acceleration required for a controlled transfer, providing $v_{d.con}$ for three types of welding processes, was calculated, namely:

1. Welding with aluminium electrode wire of Sv-AMg type in argon;
2. Welding with steel electrode wire of Sv-08G2S type also in argon;
3. Welding with steel electrode wire of Sv-08G2S type in CO_2.

Here the following condition was made: ε = 1.0–1.2. Calculations were conducted for the most characteristic welding modes, using the above wires of 1.2 and 1.6 mm diameters.

Calculations showed that for case 1 the motion acceleration should be equal to 25–35; for 2 — 40–60, and for 3 — 80 m/s^2 and more. These data do not contradict the conclusions of [5], and it is confirmed by the results of our experimental studies [1], which is indicative of the possibility of using the proposed procedure of selection of the parameters of pulsed electrode motion to implement a controlled transfer of electrode metal.

The above calculations have been verified during performance of welding on a vertical surface (vertical and horizontal welds). In all these cases a positive result was obtained at controlled transfer of electrode metal drops. This is, obviously, attributable to the fact that in the case of a pulsed electrode feed in positions other than the downhand position, an effect is achieved, which is found in downhand welding with a stationary feed of electrode wire. Pulsed feed of electrode wire provides a level of energy of detachment and motion of the drop, which is sufficient for overcoming the last force of gravity.

To achieve a controlled transfer of electrode metal with forced short-circuits, it is enough to accelerate the motion of a drop of electrode metal before it contacts the pool, and to ensure its transition into this pool due to surface tension and impact of increased electrodynamic forces. By our estimates based on experimental investigations, the acceleration imparted to the drop in this case can be 1.5 to 2 times smaller than in the absence of the short-circuits.

We have performed calculations of the required acceleration of flux-cored electrode wire tip to provide drop transfer controlled by mechanical pulses.

In view of the fact that the publications devoted to investigation of mechanized processes of arc welding and surfacing do not have a sufficient scope of information on its direct application, the proposed calculation procedure uses some indirect data [13], and also makes several assumptions, in particular, on the volumes of the melting electrode metal (given volumes of flux-cored wire sheath and volumes of solid wires were compared).

Results of these calculations made, for instance, for surfacing flux-cored wire of type PP-Np-80Kh20R3T (GSP-AN170) of 3.2 mm diameter, showed that the amplitude of acceleration of its pulsed feed should be not less than 35–45 m/s^2. However, experimental work conducted with application of pulsed feed of the above wire indicates that the acceleration providing a forced detachment and transfer of electrode metal drops into the pool is practically 2 times less than the calculated value. In our opinion, such a discrepancy between the calculated and experimental values is related to an inaccuracy of the data used in calculations, as well as to the fact that the possible change of the nature of electrode metal transfer in flux-cored wire arc welding was not taken into account.

Such a change in the nature of electrode metal transfer, in particular, formation and fragmentation of the drop, is indicated by the data given in [14], as well as data on components of the plasma flow, formed under the conditions of melting of a charge of a special composition. It is quite obvious that further research of the nature of melting and transfer of electrode metal in the welding and surfacing flux-cored wires is required. However, despite the significant discrepancies in the design and experimental results, the data obtained by the suggested procedure, can be used for defining the initial conditions of selection of the mechanism of pulsed feed of flux-cored electrode wire.

We earlier suggested a method to determine the rate and pitch of pulsed feed of electrode wire to achieve a stable arc welding process [15]. This procedure is based on determination of feed rate v_{st} in the above process, when the arc current does not go through zero value (which is a feature of welding process stability):

$$v_{st} = \frac{[(I_{max} - I_1)e^{-t/T_{cir}} - \frac{U_{o.-c} - U_{c-a} - k_a l_a}{k_{d.r} - 1/k_{f.s}}](k_{d.r} - 1/k_{f.s})}{k_a(1 - k_{sh})l_a(1 - \cos \omega t)[1 - T_{cir}(1 - e^{-t/T_{cir}})]}, \quad (9)$$

where k_a is the gradient of potential in the arc column; l_a is the length of the arc gap; $k_{f.s}$ is the coefficient of feed system that is determined by the slope of the external volt-ampere characteristic; $k_{d.r}$ is the coefficient of dynamic resistance of the arc; $U_{o.-c}$ is the open-circuit voltage; U_{c-a} is the voltage drop in the cathode-anode region; T_{cir} is the equivalent time constant of welding circuit; I_{max} is the maximum value of current; I_1 is the initial value of current; k_{sh} is the coefficient of the drop shape; ω is the frequency of displacement of electrode wire tip with a harmonic nature of motion.

Expression (9) leads to the conclusion that at $t = t_{cycle}$ (t_{cycle} is cycle time) rate v_{st} takes such a value, at which the arc current does not go through zero value, i.e. condition of a stable occurrence of the process is satisfied.

Such a technique, taking into account the equality of the cycles of forced transfer of electrode metal in welding with a pulsed feed of electrode wire, allows ignoring the drop shape and its dimensions.

Proceeding from the above, when substituting value $t < t_{cycle}$ into (9) we may obtain $v_{st} = v_{st.cr}$, where $v_{st.cr}$ is the critical rate of pulsed feed of the wire, and when it is exceeded the process looses its stability. The critical pitch of the electrode wire feed pulse, admissible proceeding from the condition of process stability, has the following form:

$$S_{cr} = v_{st.cr}/2f_p \text{ or } S_{cr} = k_{cr}d_e, \quad (10)$$

where f_p is the frequency of the pulses of electrode wire feed; k_{cr} is the coefficient of interrelation of the critical pitch of electrode wire feed and diameter.

Finally, allowing for (8) and (9) the complete condition of selection of the electrode wire feed rate $v_{d.con}$ becomes

$$\frac{[(I_{max} - I_1)e^{-t/T_{cir}} - \frac{U_{o.-c} - U_{c-a} - k_a l_a}{k_{d.r} - 1/k_{f.s}}](k_{d.r} - 1/k_{f.s})}{k_a(1 - k_{sh})l_a(1 - \cos \omega t)[1 - T_{cir}(1 - e^{-t/T_{cir}})]} > \quad (11)$$

$$> v_{d.e} > \sqrt{\frac{d_{d.e}}{\varepsilon d_e^3} \frac{ka}{1 + \sqrt{c d_{d.e} a}}}.$$

Inequality (11) is the basic one for selection of the main parameters of pulsed feed of the wire. Electrode wire feed pitch is calculated by it, using (10).

CONCLUSIONS

1. Mechanical method to control the transfer of electrode metal in consumable electrode arc welding in connection with introduction of new developments of pulsed feed mechanisms, requires simple and practicable procedures, which may be used to select the parameters of pulsed motion of electrode metal.

2. The proposed and verified by practice procedure of determination of the main parameters of pulsed motion of the electrode, which is based on energy relationships, can be used to obtain the initial evaluations of the rate and acceleration of pulsed feed that are effective in solving the problems of a controllable transfer of electrode metal.

3. When selecting the pulsed feed characteristics, it is necessary to introduce limitations, determining the stability of arc processes with a controlled transfer of electrode metal.

1. Paton, B.E., Lebedev, V.A., Pichak, V.G. et al. (2002) Analysis of technical and technological features of pulsed feed of electrode wire in arc welding and surfacing processes. *Svarochn. Proizvodstvo*, **2**, 24–31.
2. Lebedev, V.A., Moshkin, V.F., Pichak, V.G. (1996) New mechanisms of electrode wire feed. *Avtomatich. Svarka*, **5**, 39–44.
3. Dmitrienko, V.P., Potapievsky, A.G. (1982) Requirements to devices for pulsed wire feed with mechanical control of electrode metal transfer. *Sudostroenie*, **10**, 42–43.
4. Dmitrienko, V.P. (1979) Calculation of the speed of electrode tip displacement in welding with mechanical control of transfer. *Avtomatich. Svarka*, **2**, 7–9.
5. Voropaj, V.P. (1996) Parameters and technological features of arc welding with a pulsed feed of electrode and filler wire. *Ibid.*, **10**, 3–9.
6. Dyatlov, V.I. (1964) Elements of the theory of electrode metal transfer in electric arc welding. In: *New problems of welding technique*. Kiev: Tekhnika.
7. Petrov, A.V. (1957) Metal transfer in the arc and penetration of parent metal in gas-shielded welding. *Avtomatich. Svarka*, **4**, 7–10.
8. Needham, J.C., Cooksey, S.J., Milner, P.R., (1960) Metal transfer in inert gas-shielded arc welding. *British Welding J.*, **7(2)**, 101–104.
9. Kovalyov, I.M., Akulov, A.I. (1969) Relative motion of electrode metal drops in plasma flow during gas-shielded welding. *Avtomatich. Svarka*, **12**, 27–30.
10. Kovalyov, I.M., Akulov, A.I. (1969) Sizes and frequency of electrode metal drop transfer in argon metal-arc welding. *Ibid.*, **8**, 12–17.
11. Potapievsky, A.G. (1974) *Shielded metal-arc welding*. Moscow: Mashinostroenie.
12. Voropaj, N.M., Lavrishchev, V.Ya. (1976) Conditions of electrode metal transfer in CO_2 welding. *Avtomatich. Svarka*, **5**, 8–11.
13. Pokhodnya, I.K., Suptel, A.M., Shlepakov, V.N. (1972) *Flux-cored wire welding*. Kiev: Naukova Dumka.
14. Husman, M.D. (1996) Flux-cored wires as an alternative of stick electrodes and solid wire. *Svarochn. Proizvodstvo*, **1**, 34–38.
15. Dudko, D.A., Lebedev, V.A., Moshkin, V.F. et al. (2000) Stability of processes of arc welding and surfacing with pulsed feed of electrode wire. *Ibid.*, **1**, 12–15.

EVALUATION OF STEEPNESS OF THE ARC STATIC CHARACTERISTIC BY THE RESULTS OF INDIRECT MEASUREMENTS

G.A. TSYBULKIN
E.O. Paton Electric Welding Institute, NASU, Kiev, Ukraine

A method is suggested for assessment of steepness of the static characteristic of an electric arc in consumable electrode welding, which is based on using the results of indirect measurements of some parameters in the welding circuit.

Keywords: *arc welding, consumable electrode, static characteristic of the arc, stability*

It is known that in gas-shielded consumable-electrode robotic arc welding it is desirable to use the welding current sources with more flat external characteristics, compared to the manual welding sources. However, this raises some concerns, related to the possible deterioration of the stability of the welding process proper, as the condition of stability

$$S_a - S_s > -R \qquad (1)$$

can be violated at certain values of S_s [1].

In inequality (1) S_a is the steepness of the static characteristic of the arc; S_s is the steepness of the external characteristic of the current source; R is the impedance of the welding circuit, including the resistance of the current-carrying wires, sliding contact in the torch nozzle and electrode extension.

The arisen concerns could be alleviated by checking by formula (1), if we knew the values of steepness S_a for the used welding modes. Unfortunately, S_a values are usually not known, and their measurement involves great difficulties, as it requires maintaining a constant arc length, which is practically impossible to implement with the consumable electrode. We can try to obtain S_a estimate indirectly. With this purpose let us consider the relationship for time constant T_s of the welding process [2]:

$$T_s = \frac{R_*}{EM}, \qquad (2)$$

where E is the electric intensity in the arc column; M is the steepness of the electrode melting characteristic; R_* is a generalized resistance calculated from the following formula:

$$R_* = R + S_a - S_s. \qquad (3)$$

Proceeding from (2) and (3) we can write

$$S_a = T_s EM + S_s - R. \qquad (4)$$

From expression (4) it can be seen that, if we were able to determine by some means the numeric values of parameters T_s, E, M and R at a specified S_s, then the sought value of S_a could be calculated from (4). Let us consider such a possibility.

Time constant T_s can be rather accurately determined by an experimental method, suggested by Prof. B. Paton in [3], the essence of which is as follows. Electrode wire feed rate v_e is varied relative to its specified value v_{e0} by a harmonic law $v_e = v_{e0} + \Delta v_e \sin \Delta\Omega t$ (here t is the current time) with a small amplitude Δv_e and frequency Ω. Measured parameters are voltage u or current i of arc welding, which vary by the same law, but with a phase shift φ. In particular, according to [4], $i = i_0 \sin(\Omega t - \varphi)$, where Δi and i_0 are the oscillation amplitude and constant component of the welding current, respectively; $\varphi = \text{arctg}\, \Omega T_s$. Hence,

$$T_s = \frac{1}{\Omega} \text{tg}\, \varphi.$$

Value of parameter M with a sufficient accuracy is found from the following formula:

$$M = \frac{\Delta v_e}{\Delta i};$$

resistance R can be measured directly, and value of electric intensity E for each specific condition of conducting the measurements can be taken from a Table given, for instance, in [5].

Thus, we have determined that the numerical values of all the parameters included into (4) can be obtained in a rather simple manner, which means that there exists a fundamental possibility of indirect

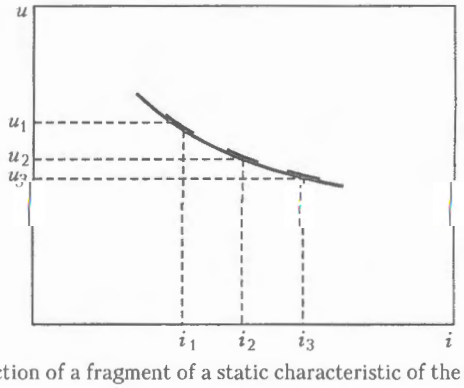

Construction of a fragment of a static characteristic of the arc from indirect measurements

evaluation of the steepness of welding arc static characteristic S_a.

Having thus obtained an evaluation of S_a, we can use the condition of stability (1) and select the admissible slope of the external characteristic of welding current source for robotic arc welding from the following formula:

$$S_s < S_a + R.$$

It should be noted that all the measurements for S_a determination from (4) should be taken at the same parameters of the welding mode. If it is necessary to get an idea about the actual shape of the static characteristic of the arc in the narrow ranges of the used arc welding modes, several such measurement should be taken and an appropriate curve should be plotted. The curve is plotted as follows.

In each fixed point (i_k, u_k), where $k = 1, \ldots, n$, and n is the number of points (Figure), a short segment is drawn at angle $\alpha = \text{arctg}\, S_a(k)$ to axis i (as in the known isocline method [6]), and then the segments are joined by a smooth line. This line will exactly be almost equidistant from the actual static characteristic of the arc in a measured range of welding currents.

1. Tsybulkin, G.A. (2002) To the question of GMAW stability. *The Paton Welding J.*, **5**, 14–16.
2. Tsybulkin, G.A. (1998) On compensation of the influence of welding parameter instability on evaluation of electrode deviation from the joint line of welded parts. *Avtomatich. Svarka*, **4**, 50–52.
3. Paton, B.E. (1952) Self-regulation of the arc in consumable electrode welding. *Ibid.*, **1**, 38–45.
4. Tsybulkin, G.A. (2003) On the influence of the speed of variation of electrode extension and arc length on arc sensor signal. *The Paton Welding J.*, **6**, 21–24.
5. Lenivkin, V.A., Dyurgerov, N.G., Sagirov, Kh.N. (1989) *Technological properties of the welding arc in shielding gases*. Moscow: Mashinostroenie.
6. Kanningham, V. (1962) *Introduction into the theory of non-linear systems*. Moscow-Leningrad: Gosenergoizdat.

EFFECT OF DETONATION COATINGS ON MECHANICAL PROPERTIES OF PRODUCTS

E.A. ASTAKHOV
E.O. Paton Electric Welding Institute, NASU, Kiev, Ukraine

Effect of coating from VK15 and Al_2O_3 on fatigue and short-time strength, ductility, impact strength of steel 45, stainless steel 10Kh18N10T and titanium alloy 3V and 3M was established.

Keywords: *carbon steel, stainless steel, titanium alloys, detonation coating, adhesion strength, mechanical properties*

The feasibility of application of detonation coating in ship-building depends on antifriction properties [1], high characteristics of adhesion strength of coatings with a base, low level of porosity [2], presence of industrial automated detonation complexes «Prometej», «Perun-S» and others [3, 4].

Nevertheless, the application of any types of coatings in ship-building, including detonation coatings, is impossible without study of their effect on design strength of the parent metal.

For this purpose, the investigation of effect of coatings from VK15 and Al_2O_3 on short-term strength, ductility, impact strength and fatigue strength of steel 45, stainless steel and titanium alloys 3V and 3M was carried out. Thickness of coating was 0.2–0.3 mm. Specimens for mechanical tests and determination of impact strength were not subjected to polishing due to the absence of a special shaped diamond tool. A special disc of a shape of a fillet on the specimen was manufactured to polish the specimens for determination of the fatigue strength.

Mechanical properties of parent metal were determined on specimens HO-8 with 15 mm diameter test part, manufactured from all the tested materials; the effect of a scale factor was evaluated on specimens HO-13 with 5 mm diameter test part, manufactured only from alloy 3M. 10 specimens of each type were tested. Test data are given in Table 1.

Table 1. Results of short-time testing of specimens with and without coating

Specimen tested	σ_t, *MPa*	$\sigma_{0.2}$, *MPa*	δ, %	ψ, %	$a_n \cdot 10^{-3}$, *J/m²*
Alloy 3M	664–700 / 679	607–635 / 626	13.3–15.7 / 14.7	35.6–37.7 / 38.9	10.9–11.4 / 11.1
Alloy 3M + coating Al_2O_3	656–679 / 671	612–636 / 624	13.3–16.5 / 14.7	38.1–41.1 / 39.0	10.1–10.7 / 10.5
Alloy 3V	753–762 / 757	649–747 / 701	19.2–21.6 / 20.5	48.9–64.7 / 51.7	11.7–18.1 / 12.2
Alloy 3V + coating VK15	540–695 / 618	497–681 / 594	12.8–14.8 / 14.0	54.7–64.1 / 58.2	11.7–14.0 / 12.9
Steel 10Kh18N10T	628–718 / 669	300–552 / 420	34.5–51.5 / 44.0	65.4–70.7 / 68.8	19.0–21.22 / 20.0
Steel 10Kh18N10T + coating Al_2O_3	624–666 / 642	581–613 / 595	35.9–49.9 / 45.8	65.9–69.7 / 67.3	20.3–21.9 / 21.2
Steel 10Kh18N10T + coating VK15	484–627 / 567	276–344 / 300	40.0–68.4 / 55.1	70.9–76.3 / 73.5	N/D
Steel 45	650–670 / 664	361–372 / 368	21.2–22.7 / 22.1	42.3–44.7 / 43.9	2.5–3.5 / 3.0
Steel 45 + coating Al_2O_3	647–670 / 657	362–390 / 369	18.8–21.6 / 20.9	43.7–45.2 / 44.5	2.7–3.4 / 3.1
Alloy 3M (HO-13)	681–701 / 690	641–670 / 648	17.2–19.6 / 18.6	36.8–46.2 / 41.0	N/D
Alloy 3M (HO-13) + coating Al_2O_3	624–666 / 642	581–613 / 595		N/D	

Note. Numerator gives the range of values, while denominator gives the mean value.

Table 2. Fatigue strength of a base with detonation coating

Material of specimen base	σ_v, *MPa*	*Medium*	*Condition of specimen*	*Fatigue limit, MPa*
Alloy 3V	757	Air	Initial	325
			Coating VK15	205
		Sea water	Initial	325
			Coating VK15	205
Alloy 3M	679	Air	Initial	361
			Coating Al_2O_3	230
10Kh18N10T	669	Same	Initial	300
			Coating VK15	185
			Coating Al_2O_3	160
Steel 45	664	»	Initial	170
			Coating Al_2O_3	160

As is seen from data obtained, the reduction in the level of strength characteristics and elongation in specimens from alloy 3V and stainless steel with coating from VK15, and also negligible increase in impact strength of alloy 3V were revealed.

On steel 45 the coating from Al_2O_3 did not almost influence the strength and ductile properties of the parent metal. Negligible increase in ultimate and yield strengths was noted on specimens from steel 10Kh18N10T. The specific ductility of steel 45, alloy 3M and stainless steel 10Kh18N10T under the effect of coating Al_2O_3 is changed very little (less than by 7 %).

Under the service conditions many components of ship structures are subjected to alternating loads, therefore, the stress concentration may lead to the fatigue fracture [5]. The change in fatigue strength of the base material was investigated after deposition of the detonation coating on it (Table 2). The fatigue strength was determined on smooth specimens with 6 mm diameter test part under the conditions of a console bending at the rotation rate of 3000 rpm. The test base was $1 \cdot 10^7$ cycles, thickness of coating layer after polishing was 0.15–0.20 mm.

The results obtained prove that the decrease in fatigue strength of titanium alloys is 36–37 % and does not depend on the coating material, unlike steel 10Kh18N10T. Thus, when the coating from VK15 is deposited it is decreased by 38 % and by 47 % at Al_2O_3 coating.

The effect of sea water on the fatigue strength of alloy 3V with detonation coating from VK15 was not observed. The deterioration of fatigue strength has the same nature as that after oxidizing used at present.

Coating from Al_2O_3 does not show any significant effect on the strength of steel 45 in air.

CONCLUSIONS

1. It was established that the detonation coating from Al_2O_3 does not almost change the short-time strength, ductility and impact strength of alloy 3M, steel 45 and stainless steel 10Kh18N10T, while the coating from VK15 reduces these characteristics for alloy 3V and stainless steel by 15–20 % on average. Exception is the impact strength of alloy 3V, as it is constant.

2. It was found that the fatigue strength of steel 45 in air is not changed under the influence of the deposited coating from Al_2O_3, while for alloy 3M and stainless steel 10Kh18N10T it is decreased, respectively, by 36 and 47 % in deposition of coating from Al_2O_3 and by 37–38 % in deposition of coating from VK15.

3. The results obtained can be used in detonation coating of friction surfaces of main shafts to avoid the bronze lining.

Author expresses the acknowledgement to Dr. V.N. Goldfajn, staff scientist of TsNII «Prometej» (Russia), for assistance in organizing the present work fulfillment.

1. Goldfajn, V.I., Astakhov, E.A., Zverev, A.I. et al. (1979) Study of antifriction properties of VK15 coatings deposited by detonation method on VT5 alloy. *Poroshk. Metallurgiya*, 1, 81–84.
2. Zverev, A.I., Sharivker, S.Yu., Astakhov, E.A. (1979) *Detonation spraying of coatings*. Leningrad: Sudostroenie.
3. Astakhov, E.A., Filippov, D.T. (1988) *Detonation spraying for repair and hardening of parts of ship mechinery*. Kiev: Znanie.
4. Yushchenko, K.A., Astakhov, E.A., Klimenko, V.S. et al. (1990) Detonation spraying of strengthening coatings and ways of its development. In: *Transact. on New Processes and Equipment for Thermal Sprayed and Vacuum Coatings*. Kiev: PWI.
5. Vinogradov, S.S. (1967) *Fast repair of catcher boats*. Leningrad: Sudostroenie.